BRNO UNIVERSITY OF TECHNOLOGY

VYSOKÉ UČENÍ TECHNICKÉ V BRNĚ

FACULTY OF ELECTRICAL ENGINEERING AND COMMUNICATION

FAKULTA ELEKTROTECHNIKY A KOMUNIKAČNÍCH TECHNOLOGIÍ

DEPARTMENT OF BIOMEDICAL ENGINEERING

ÚSTAV BIOMEDICÍNSKÉHO INŽENÝRSTVÍ

SIMULTANNEOUS EEG-FMRI DATA FUSION WITH GENERALIZED SPECTRAL PATTERNS

FÚZE SIMULTÁNNÍCH EEG-FMRI DAT ZA POMOCI ZOBECNĚNÝCH SPEKTRÁLNÍCH VZORCŮ

DOCTORAL THESIS

DIZERTAČNÍ PRÁCE

AUTHOR AUTOR PRÁCE	Ing. René Labounek
ACADEMIC ADVISOR ŠKOLITEL	prof. Ing. Jiří Jan, CSc.
EXPERT ADVISOR ŠKOLITEL – SPECIALISTA	Ing. Michal Mikl, Ph.D.
EXPERT ADVISOR ŠKOLITEL – SPECIALISTA	David A. Bridwell, Ph.D.

BRNO 2018

ABSTRACT

Lots of different data fusion strategies have been developed during last 15 years of simultaneous EEG-fMRI research. The current doctoral thesis summarizes the actual state of the art in EEG-fMRI data fusion research and puts a goal to improve task-related network visualizations blindly directly from the acquired data. Two different models which should improve it have been proposed within the thesis (i.e. generalized spectral heuristic model and generalized spatiospectral heuristic model). Generalized spectral heuristic model utilizes relative EEG power fluctuations in distinct frequency bands averaged over electrodes of interest and compares the fluctuations with delayed BOLD signal fluctuations via general liner model. The obtained results shows that the model visualizes several different frequency dependent task-related EEG-fMRI networks. The model overcomes the absolute power fluctuation approach and classic heuristic approach too. The absolute power visualized a task-not-related broadband EEG-fMRI component and classic heuristic model was insensitive to visualize the task-related visual network which was observed for the relative α-band pattern for visual oddball task data. For the semantic decision task EEG-fMRI data, the frequency dependence was not so evident in final results. Since all the bands visualized only visual network and any areas of speech network, the results were possibly corrupted by not-suppressed eye-blinking artifact in EEG data. Mutual information coefficients between different EEG-fMRI statistical parametric maps showed that the similarities over different frequency bands are similar over different tasks (i.e. visual oddball and semantic decision). More, the coefficients proved that averaging over different electrodes of interest does not bring any new information into the joint analysis, i.e. the signal on one single lead is very smoothed signal from the whole scalp. For that reasons, better incorporation of the channel information into the EEG-fMRI analysis started to be necessary and we have proposed more general spatiospectral heuristic model and designed how to estimate the model with spatiospectral Group Independent Component Analysis of EEG spectra relative power. The obtained results show that spatiospectral heuristic model visualizes the statistically most significant task-related networks (compared to absolute power spatiospectral pattern results and generalized spectral heuristic model results). The spatiospectral heuristic model was the only one, which observed task-related activations in a speech areas for semantic decision data. Beyond the fusion of EEG spatiospectral patterns with fMRI data, we have tested the stability of the spatiospectral pattern estimates over different paradigms (i.e. visual oddball, semantic decision and resting-state) with k-means clustering algorithm. We have got 14 stable patterns for the absolute EEG power and 12 stable patterns for the relative EEG power. Although ten of the patterns appear similar over the power types, the relative power spatiospectral patterns (i.e. spatiospectral heuristic model patterns) have higher evidence to tasks.

KEYWORDS

simultaneous EEG-fMRI, heuristic approach, spatiospectral group-ICA, independent component analysis, general linear model, GLM, visual oddball, semantic decision, resting-state, k-means clustering, ICASSO, GIFT, SPM12, EEG Regressor Builder

ABSTRAKT

Mnoho rozdílných strategií fúze bylo vyvinuto během posledních 15 let výzkumu simultánního EEG-fMRI. Aktuální dizertační práce shrnuje aktuální současný stav v oblasti výzkumu fúze simultánních EEG-fMRI dat a pokládá si za cíl vylepšit vizualizaci úkolem evokovaných mozkových sítí slepou analýzou přímo z nasnímaných dat. Dva rozdílné modely, které by to měly vylepšit, byly navrhnuty v předložené práci (tj. zobecněný spektrální heuristický model a zobecněný prostorovo-frekvenční heuristický model). Zobecněný frekvenční heuristický model využívá fluktuace relativního EEG výkonu v určitých frekvenčních pásmech zprůměrovaných přes elektrody zájmu a srovnává je se zpožděnými fluktuacemi BOLD signálů pomocí obecného lineárního modelu. Získané výsledky ukazují, že model zobrazuje několik na frekvenci závislých rozdílných úkolem evokovaných EEG-fMRI sítí. Model překonává přístup fluktuací absolutního EEG výkonu i klasický (povodní) heuristický přístup. Absolutní výkon vizualizoval s úkolem nesouvisející širokospektrální EEG-fMRI komponentu a klasický heuristický přístup nebyl senzitivní k vizualizaci s úkolem spřažené vizuální sítě, která byla pozorována pro relativní α pásmo pro data vizuálního oddball experimentu. Pro EEG-fMRI data s úkolem sémantického rozhodování, frekvenční závislost nebyla ve finálních výsledcích tak evidentní, neboť všechna pásma zobrazily vizuální síť a nezobrazily aktivace v řečových centrech. Tyto výsledky byly pravděpodobně poškozeny artefaktem mrkání v EEG datech. Koeficienty vzájemné informace mezi rozdílnými EEG-fMRI statistickými parametrickými mapami ukázaly, že podobnosti napříč různými frekvenčními pásmy jsou obdobné napříč různými úkoly (tj. vizuální oddball a sémantické rozhodování). Navíc, koeficienty prokázaly, že průměrování napříč různými elektrodami zájmu nepřináší žádnou novou informaci do společné analýzy, tj. signál na jednom svodu je velmi rozmazaný signál z celého skalpu. Z těchto důvodů začalo být třeba lépe zakomponovat informace ze svodů do EEG-fMRI analýzy, a proto jsme navrhli více obecný prostorovo-frekvenční heuristický model a také jak ho odhadnout za pomoci prostorovo-frekvenční skupinové analýzy nezávislých komponent relativního výkonu EEG spektra. Získané výsledky ukazují, že prostorovo-frekvenční heuristický model vizualizuje statisticky nejvíce signifikantní s úkolem spřažené mozkové sítě (srovnáno s výsledky prostorovo-frekvenčních vzorů absolutního výkonu a s výsledky zobecněného frekvenčního heuristického modelu). Prostorovo-frekvenční heuristický model byl jediný, který zaznamenal s úkolem spřažené aktivace v řečových centrech na datech sémantického rozhodování. Mimo fúzi prostorovo-frekvenčních vzorů s fMRI daty, jsme testovali stabilitu odhadů prostorovo-frekvenčních vzorů napříč různými paradigmaty (tj. vizuální oddball, semantické rozhodování a resting-state) za pomoci k-means shlukovacího algoritmu. Dostali jsme 14 stabilních vzorů pro absolutní EEG výkon a 12 stabilních vzorů pro relativní EEG výkon. Ačkoliv 10 z těchto vzorů vypadají podobně napříč výkonovými typy, prostorovo-frekvenční vzory relativního výkonu (tj. vzory prostorovo-frekvenčního heuristického modelu) mají vyšší evidenci k úkolům.

KLÍČOVÁ SLOVA

simultánní EEG-fMRI, heuristický přístup, prostorovofrekvenční skupinová-ICA, analýza nezávislých komponent, obecný lineární model, GLM, vizuální oddball, semantické rozhodování, resting-state, k-means shlukování, ICASSO, GIFT, SPM12, EEG Regressor Builder

LABOUNEK, René *Simultanneous EEG-fMRI data fusion with generalized spectral patterns*: doctoral thesis. Brno: Brno University of Technology, Faculty of Electrical Engineering and Communication, Department of Biomedical Engineering, 2018. 142 p. Supervised by prof. Ing. Jiří Jan, CSc., Ing. Michal Mikl, Ph.D. and David A. Bridwell, Ph.D.

DECLARATION

I declare that I have written my doctoral thesis on the theme of "Simultanneous EEG-fMRI data fusion with generalized spectral patterns" independently, under the guidance of the doctoral thesis supervisor and using the technical literature and other sources of information which are all quoted in the thesis and detailed in the list of literature at the end of the thesis.

As the author of the doctoral thesis I furthermore declare that, as regards the creation of this doctoral thesis, I have not infringed any copyright. In particular, I have not unlawfully encroached on anyone's personal and/or ownership rights and I am fully aware of the consequences in the case of breaking Regulation § 11 and the following of the Copyright Act No 121/2000 Sb., and of the rights related to intellectual property right and changes in some Acts (Intellectual Property Act) and formulated in later regulations, inclusive of the possible consequences resulting from the provisions of Criminal Act No 40/2009 Sb., Section 2, Head VI, Part 4.

Brno ....

author's signature

ACKNOWLEDGEMENT

I would like to thank to the doctoral thesis academic advisor prof. Ing. Jiří Jan, CSc. and specialist advisors Ing. Michal Mikl, Ph.D. and David A Bridwell, Ph.D. for professional guidance, consultations, patience and contributing ideas to the thesis. More, I would like to thank to them and to other colleagues Ing. Radek Mareček, Ph.D., Ing. Martin Lamoš, Ing. Tomáš Slavíček, MUDr. Petr Bednařík, Ph.D., doc. Ing. Jaromír Baštinec, CSc., prof. MUDr. Milan Brázdil, Ph.D. and prof. MUDr. Ing. Petr Hluštík, Ph.D. for their expertise, advices, comments, help and support during manuscript's writings, submissions and other things.

I would like to thank to assistant prof. Christophe Lenglet, Ph.D. for letting me come to Center for Magnetic Resonance Research, University of Minnesota, USA at Research Scholar Fellowship and other local workers who welcomed me warmly and were gentle mentors. It was very valuable experience for me, I was trying to work hard there, and I believe I will be able to work together with them again. Special and heartfelt thanks belong to MUDr. Petr Bednařík, Ph.D. and MUDr. Alena Svátková, Ph.D. who let me stay in their place and made me *"a little home"* in USA.

I would like to thank to my students Ing. David Janeček, Ing. Dominika Sanetrníková, Ing. Radek Valla, Ing. Zuzana Piskořová and Ing. Jakub Zimolka who were working hard on their bachelor and master theses which helped to answer and solve some questions.

I would like to thank to my parents René Labounek and MUDr. Marcela Labounková for their help, support and patience during my *"longstanding"* studies. Last but not least, I would like to thank to my wife Ing. Ivana Labounková for her love, kindness and support.

It would not be possible to write my doctoral thesis without all of you.

This research was supported by grant n. P304/11/1318 of Grant Agency of Czech Republic, grant n. FEKT-S-14-2210 of Brno University of Technology, by grant n. CZ.1.05/1.1.00/02.0068 of Central European Institute of Technology and by grant n. AZV 16-30210A of Palacky University. The foundation *"Nadání Josefa, Marie a Zdeňky Hlávkových"* funded my travel costs for international conference presentation of my work. All funding sources are highly acknowledged.

All EEG-fMRI measurements were performed at the 1^{st} Department of Neurology, St. Anne's University Hospital Brno, Czech Republic.

Computational resources were provided by the CESNET LM2015042 and the CERIT Scientific Cloud LM2015085, provided under the programme "Projects of Large Research, Development, and Innovations Infrastructures".

Brno ....

author's signature

LIST OF PUBLICATIONS

IF journal publications

- **LABOUNEK, R.**; LAMOŠ, M.; MAREČEK, R.; BRÁZDIL, M.; JAN, J. *Exploring task-related variability in fMRI data using fluctuations in power spectrum of simultaneously acquired EEG.* ***Journal of Neuroscience Methods***, 2015, vol. 245, no. 1, p. 125-136. ISSN: 0165-0270. [**IF: 2.053, WOS cit.: 5; Scopus cit.: 4; Google Scholar cit.: 7**]
- MAREČEK, R.; LAMOŠ, M.; **LABOUNEK, R.**; BARTOŇ, M.; SLAVÍČEK, T.; MIKL, M.; REKTOR, I.; BRÁZDIL, M. *Multiway array decomposition of EEG spectrum: Implications of its stability for the exploration of large-scale brain networks.* ***Neural Computation***, 2017, vol. 29, no. 4, p. 968-989. ISSN: 0899-7667. [**IF: 1.626; Scopus cit.: 1, Google Scholar cit.: 2**]
- **LABOUNEK, R.**; BRIDWELL, D.; MAREČEK, R.; LAMOŠ, M.; MIKL, M.; SLAVÍČEK, T.; BEDNAŘÍK, P.; BAŠTINEC, J.; HLUŠTÍK, P.; BRÁZDIL, M.; JAN, J. *Stable Scalp EEG Spatiospectral Patterns Across Paradigms Estimated by Group ICA.* ***Brain Topography***, 2018, vol. 31, no. 1, p. 76-89 ISSN: 0896-0267. [**IF: 3.394**]

Conference proceedings indexed at WOS or Scopus

- **LABOUNEK, R.**; LAMOŠ, M.; MAREČEK, R.; JAN, J. *Analysis of connections between simultaneous EEG and fMRI data.* In ***Proceedings of 19th International Conference on Systems, Signals and Image Processing (IEEE - IWSSIP)***. Vienna, Austria: 2012. p. 594-597. ISBN: 978-3-200-02588- 2. [**Google Scholar cit.: 5**]
- **LABOUNEK, R.**; JANEČEK D.; MAREČEK, R.; LAMOŠ, M.; SLAVÍČEK T.; MIKL M.; BAŠTINEC J.; BRIDWELL D.; BRÁZDIL, M.; JAN, J. *Generalized EEG-fMRI Spectral and Spatiospectral Heuristic Models.* In ***Proceedings of International Symposium on Biomedical Imaging (IEEE - ISBI)***. Prague, Czech Republic: 2016. p. 767-770. ISBN: 978-1-4799-2350- 2. ISSN: 1945-7928. [**WOS cit.: 1; Scopus cit.: 1, Google Scholar cit.: 4**]

International conference abstracts

- **LABOUNEK, R.**; GAJDOŠ, M.; FOUSEK, J.; MIKL, M.; HAVLÍČEK, M.; BRÁZDIL, M.; JAN, J. *Sigmoid function parameter stability in anatomically informed priors for dynamic causal models.* In ***Proceedinds of 20th Annual Meet-***

ing of the Organization for Human Brain Mapping. Hamburg, Germany: OHBM, 2014.

- **LABOUNEK, R.**; MIKL, M.; JAKUBÍČEK, R.; CHMELÍK, J.; JAN, J. *Could it be possible to distinguish bending and crossing fibers in diffusion MRI data?*. ***Clinical Neurophysiology***. Netherlands: Elsevier B.V., 2015. p. e46 ISSN: 1388-2457. [**IF: 3.426**]
- **LABOUNEK, R.**; MIKL, M.; JAN, J.; VALLA, R.; BAŠTINEC, J.; LENGLET, C. *Effects of axonal spatial distribution and diameter on diffusion MR simulations*. In ***Proceedings of 22nd Annual Meeting of the Organization for Human Brain Mapping***. Geneva, Switzerland: (OHBM), 2017.

National conference abstracts

- **LABOUNEK, R.**; JAN, J.; LAMOŠ, M.; MAREČEK, R. *EEG Regressor Builder - nástroj pro EEG/fMRI analýzu*. ***Česká a slovenská neurologie a neurochirurgie***. Media Hall, Bidláky 20, 639 00 Brno: Ambit Media, a.s., 2012. p. 28-29. ISSN: 1210-7859.
- **LABOUNEK, R.**; LAMOŠ, M.; MAREČEK, R.; JAN, J. *Korelace simultánních výkonových spekter EEG signálu s BOLD signálem během vizuálního oddball experimentu*. In ***9. mezinárodní workshop funkční magnetické rezonance***. Olomouc, 2013. p. 34-34. [**Google Scholar cit.: 2**]
- **LABOUNEK, R.**; FOUSEK, J.; GAJDOŠ, M.; MIKL, M.; JAN, J. *Gamma rozložení pravděpodobnosti anatomické konektivity mezi aktivními motorickými koretexy a cerebellem*. In ***10. Mezinárodní Workshop Funkční magnetické rezonance***. Olomouc, 2014. p. 10-11.

Software

- **LABOUNEK, R.**; JANEČEK, D.; SANETRNÍKOVÁ, D.; LAMOŠ, M.; JAN, J.; MAREČEK, R.: *EEG Regressor Builder ver. 2*. Brno University of Technology, Czech Republic. Available from: `http://www.ubmi.feec.vutbr.cz/sites/default/files/products/26150.zip`

CONTENTS

LIST OF FIGURES

LIST OF TABLES

INTRODUCTION

Since Isidor Rabi (1937) declared and measured atom's nuclear magnetic resonance at molecular beams [170], Felix Bloch and Edward Purcell (1946) expanded it at liquid and solid measurements [17, 169] and Paul Lauterbur (1973) introduced basal principles of magnetic resonance imaging (MRI) [129], many different MRI sequences able to visualize different chemico-physical phenomena were invented. In biomedical imaging applications, different chemico-physical image contrasts can provide different qualitative and quantitative information about in-vivo displayed tissue. The qualitative information presents the property of measured variable (e.g. high resolution anatomy [58, 174, 205], blood oxygenation [161, 162, 163], concentration [53, 133], diffusion constant [8, 154, 155],...). And the quantitative information presents rate of qualitative information distribution over space, or over time, or over both, etc. Simply, MRI became to be an indispensable diagnostic method which is still under development.

After 1990, Ogawa's et al. MRI sequences sensitive to blood oxygenation [161, 162, 163] gave raise to the field called functional magnetic resonance imaging (fMRI) because repetitive time of one 3D image scanning fulfills the Nyquist theorem [98] for capturing of dynamic cardio-vascular changes evoked by induced neuronal activity [86]. That kind of imaging started to be widely used in basic and clinical research of brain's [7, 54, 112, 203] and spinal cord's [115, 195, 196, 197] gray matter activity visualizations.

Practically immediately after BOLD signal discovery (blood oxygen level dependence) [161, 162, 163], other scientists started to think about simultaneous recording of scalp electrophysiological and functional MRI data. They solved it between 1993-1995 and scientific field called simultaneous EEG-fMRI[1] was born [85, 96]. The 1^{st} initial trouble which had to be solved was gradient artefact suppression from simultaneously EEG signal. There were two main problems. The amplitude of the MR pulse gradients is much higher than EEG signal amplitude, and frequency characteristics of both signals overlap themselves. Fortunately because of quite stable temporal characteristic of the pulse gradient, Allen et al. and Goldman et al. solved it with cumulative signal filtering techniques at the end of the millennium [3, 4, 72]. And, the fusion of simultaneous EEG-fMRI data has become to be possible since that times [72, 73, 127].

Submitted doctoral thesis deals with current improvements in simultaneous EEG-fMRI data fusion via generalized spectral patterns. The whole work is organized

[1]The measurement when the brain neuronal activity is captured simultaneously with two different physical techniques - electroencephalography (EEG) [157] and functional magnetic resonance imaging (fMRI) [86].

into 5 separate chapters. The *chapter 1. "Simultaneous EEG-fMRI data analysis: a brief state of the art"* introduces briefly used statistical models and the current state of art in simultaneous EEG-fMRI data fusion research, highlights current shortcomings and explains why we have decided to improve selected deficiencies (i.e. incorporation of relative EEG power and spatiospectral EEG decomposition of it at independent components used as input into the joint EEG-fMRI analysis). The *chapter 2. "Ph.D. thesis objectives"* defines main objectives of the doctoral thesis which should be achieved for a successful improvements of the current EEG-fMRI methods. The *chapter 3. "Generalized EEG-fMRI spectral heuristic model"* is devoted to the relative EEG power incorporation into the EEG-fMRI analysis and contains the whole problem formulation since the description of methods, through results and discussion, upto the conclusions and evaluations of the benefits of the derived generalized spectral heuristic model. The *chapter 4. "EEG spatiospectral patterns for EEG-fMRI fusion"* is organized in the same order as the *chapter 3. "Generalized EEG-fMRI spectral heuristic model"* for spatiospectral group Independent Component Analysis (group-ICA) of EEG signal, tests the stability of derived spatiospectral patterns over different paradigms and subjects, assesses its benefits and limits for the EEG-fMRI data fusion and evaluates benefits of declared generalized EEG-fMRI spatiospectral heuristic model. The final *chapter 5. "Ph.D. thesis outcomes and conclusions"* repeats the thesis objectives and describes whether and how each sub-objective was or was not fulfilled.

1 SIMULTANEOUS EEG-FMRI DATA ANALYSIS: A BRIEF STATE OF THE ART

Ives et al. (1993) captured the first EEG signal record during echo-planar MRI [96]. Huang-Hellinger et al. (1995) performed the first initial simultaneous EEG-fMRI measurements [85] about two years after Ogawa's et al. (1990-1993) discovering of blood oxygen level dependence effect at MR signal (also called BOLD signal) [161, 162, 163]. Initial joint EEG-fMRI data analyses [72, 73, 127] became possible after next five years (approx. since 2000), when already initial algorithms for the proper suppression of gradient MR artifacts from acquired EEG appeared available [3, 4, 72]. It means that the brain neuronal activity has been capturing simultaneously with two physically different measuring modalities since that times, where each recorded signal dispose with different properties and characters, although they both contains the same underlying activity.

The EEG signal summarizes all chemico-electrical brain events measured with unpolarized electrodes on the scalp or from intra-cranial space [157], and has the character of stationary and ergodic stochastic signal [98] for its short sections with practically any delay after neuronal activations. Only scalp EEG records were used in the current thesis. The EEG records dispose with much better temporal resolution (sampling frequency 100-5000Hz) than fMRI records (sampling approx. 0.3-1.5Hz) but also with much lower spatial resolution (EEG: 20-256 electrodes over the scalp; fMRI: 3D sampling from units up to tens of mm^3 per voxel).

In fMRI, the local BOLD signal changes are proportional to local delayed hemodynamic changes in brain's cardiovascular system evoked after local neuronal activity increase. The dependence between the neuronal activity and the BOLD signal was described with the four state variable hemodynamic model [25, 59, 64]. It is schematically shown in Fig. 1.1a, where the induced neuronal activity $\boldsymbol{u}(t)$ evokes changes in vasodilative signal dynamics $\boldsymbol{s}(t)$ containing a subsume of neurogenic and diffusive signal subcomponents. After that, the blood flow is increasing $\boldsymbol{f}(t)$ followed by the changes in blood volume $\boldsymbol{v}(t)$ and in paramagnetic deoxy-hemoglobin (dHb) concentration $\boldsymbol{q}(t)$. The BOLD signal $\boldsymbol{y}(t)$ is given by the the non-linear response at those changes [59, 64, 78].

Although the single-input single-output hemodynamic model (1.1a) is modulated with an non-linear function [64], the whole model can be considered as a linear system whose impulse response function (IRF) is called the *hemodynamic response function* (HRF) [86] shown in Fig. 1.1b for canonical HRF. Because superposition principle applies to linear systems, theoretical BOLD signal response can be mod-

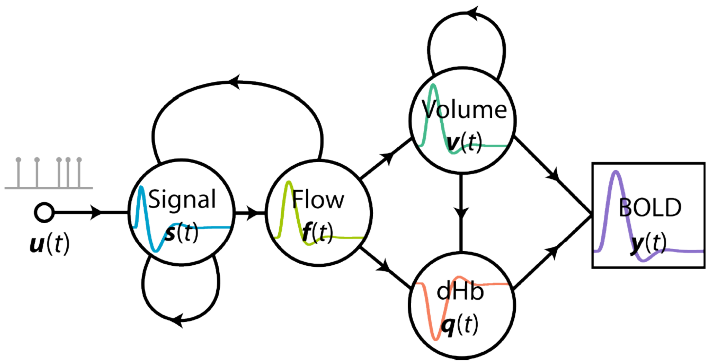

(a) Hemodynamic model diagram [78]

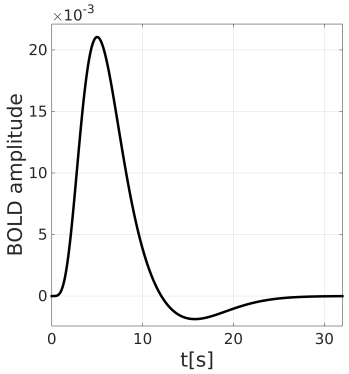

(b) canonical HRF

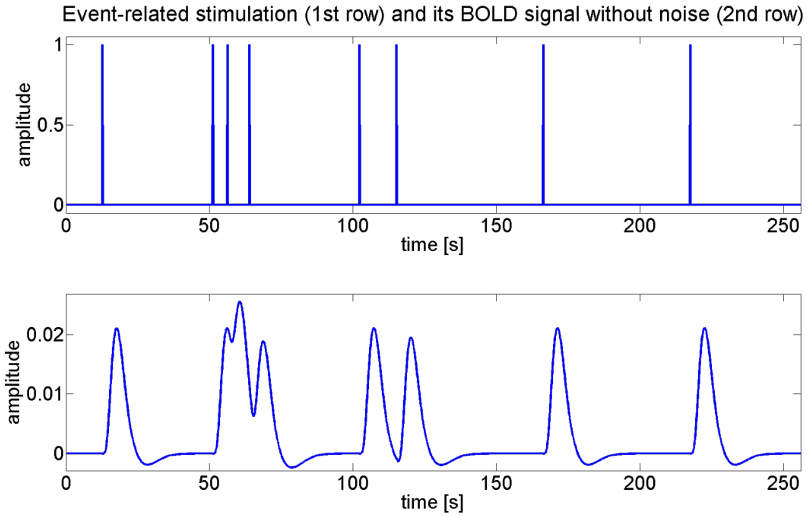

(c) Event-related design

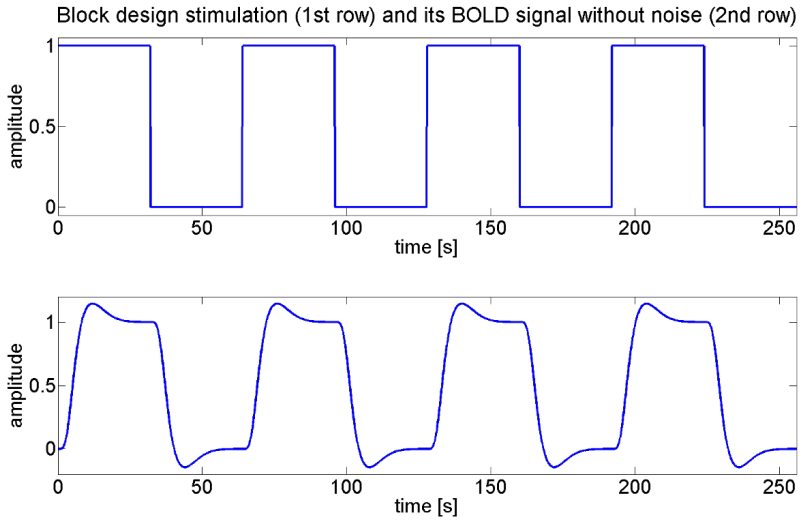

(d) Block design

Fig. 1.1: The basics of functional magnetic resonance imaging

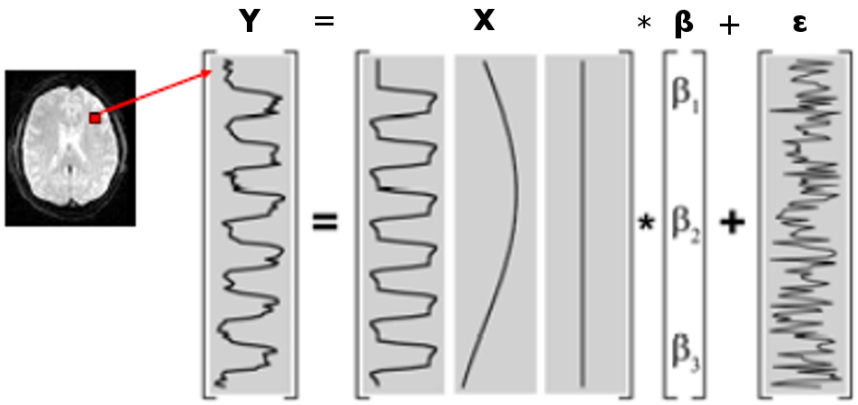

Fig. 1.2: General linear model in single-voxel: designed by Michal Mikl.

elled [86] as e.g. for the stimulus function of some event-related[1] (Fig. 1.1c) or block[2] (Fig. 1.1d) experimental design.

Since it is possible to model and predict the BOLD signal's shape and timings, several different data analysis approaches and strategies have been developed (e.g. general linear model [62], spatial decomposition with independent component analysis [30, 31, 33], dynamic causal modelling [66, 67], Granger causality [71, 77], etc.). Only the first two will be considered and described here because the others are out of scope of the current thesis.

1.1 General Linear Modelling

The linear effect of the HRF and modulation of experimental designs were used for brain's increased activity localization in the 1^{st} only fMRI voxel-wise studies [62, 63, 213, 214] where spatial statistical parametric maps (SPMs) were estimated with the general linear model (GLM, eq. 1.1) [62] between measured BOLD data from each voxel in matrix $\boldsymbol{Y}$ and the theoretical expected BOLD signal response for a given experiment paradigm (e.g. Fig. 1.1c or Fig. 1.1d) putted into the matrix of regressors[3] $\boldsymbol{X}$ as shown in Fig. 1.2 with 2 other model signals whose linear trends in signal $\boldsymbol{Y}$ are also estimated.

$$\boldsymbol{Y} = \boldsymbol{X}\boldsymbol{\beta} + \boldsymbol{\epsilon} \tag{1.1}$$

[1]Type of an external stimulation where stimulus duration is much lower and the inter-stimulus interval higher than the temporal sampling period of the captured signal.

[2]Type of an external stimulation where stimulus duration is much higher than the temporal sampling period of the captured signal.

[3]regressor = independent explanatory model variable

Between each voxel w and each regressor r, the value of the regression coefficient $\beta_{r,w}$ to a given voxel's BOLD signal is estimated. The matrix $\boldsymbol{\epsilon}$ contains the noise in the BOLD data dynamics whose powers are minimized during the GLM estimation [62]. In Fig. 1.2, there is shown for one voxel w what we are trying to fit ($\beta_{1,w}$-$\beta_{3,w}$), when we are looking for the task-evoked supra-thresholded voxel with 3 different regressors, where the regressor n. 1 $\boldsymbol{x}_1$ represents the theoretical task-related BOLD response and $\beta_{1,w}$ its regression coefficient in the voxel w.

The expectation maximization (EM) [151] algorithm is the most often used optimizing method for the $\boldsymbol{\beta}$ regression value estimations in fMRI area. The simplest estimation of $\boldsymbol{\beta}$ values with EM is usually performed with ordinary least square (OLS) algorithm (eq. 1.2) [62] or with weighted least square (WLS) algorithm (eq. 1.3) where $\boldsymbol{\Sigma}_{\boldsymbol{\epsilon}}$ is the covariance matrix of residual matrix $\boldsymbol{\epsilon}$ [49, 65].

$$\boldsymbol{\beta} = (\boldsymbol{X}^T\boldsymbol{X})^{-1}\boldsymbol{X}^T\boldsymbol{Y} \tag{1.2}$$

$$\boldsymbol{\beta} = (\boldsymbol{X}^T\boldsymbol{\Sigma}_{\boldsymbol{\epsilon}}^{-1}\boldsymbol{X})^{-1}\boldsymbol{X}^T\boldsymbol{\Sigma}_{\boldsymbol{\epsilon}}^{-1}\boldsymbol{Y} \tag{1.3}$$

Penalized least square (PLS, eq. 1.4) or weighted penalized least square (WPLS, eq. 1.5) solutions give effect to Tikhonov regularization [74] into estimations where $\boldsymbol{I}$ is the identity matrix and where appropriately chosen regularizing parameter λ guarantee the convergence.

$$\boldsymbol{\beta} = (\boldsymbol{X}^T\boldsymbol{X} + \lambda\boldsymbol{I})^{-1}\boldsymbol{X}^T\boldsymbol{Y} \tag{1.4}$$

$$\boldsymbol{\beta} = (\boldsymbol{X}^T\boldsymbol{\Sigma}_{\boldsymbol{\epsilon}}^{-1}\boldsymbol{X} + \lambda\boldsymbol{I})^{-1}\boldsymbol{X}^T\boldsymbol{\Sigma}_{\boldsymbol{\epsilon}}^{-1}\boldsymbol{Y} \tag{1.5}$$

Bayesian statistics [190] brings into account prior and posterior observations of optimized parameters. Fully Bayesian form of GLM solution with EM algorithm maximizing the data-model likelihood is shown in eq. 1.6 where diagonal matrix $\boldsymbol{\beta}_0$ contains prior mean values of optimized parameters and $\boldsymbol{\Sigma}_{\boldsymbol{\beta}_0}$ is a covariance matrix of the priors [65].

$$\boldsymbol{\beta} = (\boldsymbol{X}^T\boldsymbol{\Sigma}_{\boldsymbol{\epsilon}}^{-1}\boldsymbol{X} + \boldsymbol{\Sigma}_{\beta_0}^{-1})^{-1}(\boldsymbol{X}^T\boldsymbol{\Sigma}_{\boldsymbol{\epsilon}}^{-1}\boldsymbol{Y} + \boldsymbol{\Sigma}_{\beta_0}^{-1}\boldsymbol{\beta}_0) \tag{1.6}$$

When the regression coefficients $\boldsymbol{\beta}$ are estimated, the spatial effect of one or more regressors inside the single-subject brain's volume are often estimated with one-sample T-test (eq. 1.7 [214], where $\boldsymbol{c}$ is a row vector containing weights of contrast on regressors of interest and $\Sigma_{\boldsymbol{\epsilon},w}$ is variance of noise $\boldsymbol{\epsilon}$ in the voxel w), or with F-test (eq. 1.8, where $\Sigma_{\boldsymbol{\epsilon},w,1}$ is a noise variance without variability explained by the reduced model of interest n. $\boldsymbol{X}_1$, $\Sigma_{\boldsymbol{\epsilon},w}$ is a noise variance without variability

explained by full model $\boldsymbol{X}$, k_1 is number of degrees of freedom for the reduced model, k is number of degrees of freedom for the full model and t is number of fMRI signal time points). It applies everytime: $k_1 < k$.

$$T_w = \frac{\boldsymbol{c}\boldsymbol{\beta}_{\boldsymbol{w}}}{\sqrt{\boldsymbol{c}\Sigma_{\boldsymbol{\epsilon},w}(\boldsymbol{X}^T\boldsymbol{X})^{-1}\boldsymbol{c}^T}} \qquad T_w \in (-\infty;\infty) \tag{1.7}$$

$$F_w = \frac{t-k}{k-k_1} \cdot \frac{\Sigma_{\boldsymbol{\epsilon},w,1} - \Sigma_{\boldsymbol{\epsilon},w}}{\Sigma_{\boldsymbol{\epsilon},w}} \qquad F_w \in \langle 0;\infty) \tag{1.8}$$

Fig. 1.3 visualizes an example of some model matrix $\boldsymbol{X}$ (Fig. 1.3a) for whose single-subject 3D T-test map (of 1^{st} regressor $\boldsymbol{x}_1$ - Fig. 1.3b; and of 2^{nd} regressor $\boldsymbol{x}_2$ - Fig. 1.3d) and single-subject 3D F-test map (of the effect of 1^{st} two regressors $\boldsymbol{x}_1$ and $\boldsymbol{x}_2$ on final data error variance - Fig. 1.3c) can be estimated. And as you can see in the listed figures, each tested hypothesis disposes with different spatial pattern over brain and with different result's interpretation.

For group-averaged analyses over set of participants, the effect of some regressor can be estimated also within the one-sample t-test where $\langle \boldsymbol{c}\boldsymbol{\beta}_{\boldsymbol{w}} \rangle$ in eq. 1.9 characterizes the expectation over group in the voxel w, $\Sigma_{\langle \boldsymbol{c}\boldsymbol{\beta}_{\boldsymbol{w}} \rangle}$ is the variance over the group and s is number of participants in the analysis.

$$T_w = \sqrt{\frac{s}{\Sigma_{\langle \boldsymbol{c}\boldsymbol{\beta}_{\boldsymbol{w}} \rangle}}} \langle \boldsymbol{c}\boldsymbol{\beta}_{\boldsymbol{w}} \rangle \qquad T_w \in (-\infty;\infty) \tag{1.9}$$

If it is necessary to observe the group effect over the set of regressors in each voxel w, the most often used approach is the one-way ANOVA test (analysis of variance; eq. 1.10) over group of participants (index j) and several contrasts at different regressors (index i). The variable μ_{β_w} represents some fitted global β value in voxel w consistent over all contrasts, b_{wi} is the effect of each individual regressor i and ϵ_{wij} is an error in estimates for corresponding voxel, regressor and participant. The expectation of $i-th$ regressor can be estimated with eq.1.11. Following F-test (eq. 1.8) on ANOVA's residuals serves for group-averaged 3D SPM's visualization.

$$\boldsymbol{c}_i\boldsymbol{\beta}_{wij} = \mu_{\beta_w} + b_{wi} + \epsilon_{wij} \tag{1.10}$$

$$\mu_{\beta_{wi}} = \mu_{\beta_w} + b_{wi} \tag{1.11}$$

In pure fMRI data analyses, the GLM's main limitation is that it is applicable only for data with a task during measured experiment. It can not be used e.g. for analysing of resting-state[4] data. Nowadays, this experiment is commonly used for

[4]The experimental paradigm without participant's external stimulation with closed or opened eyes. The subject is instructed to not fall asleep.

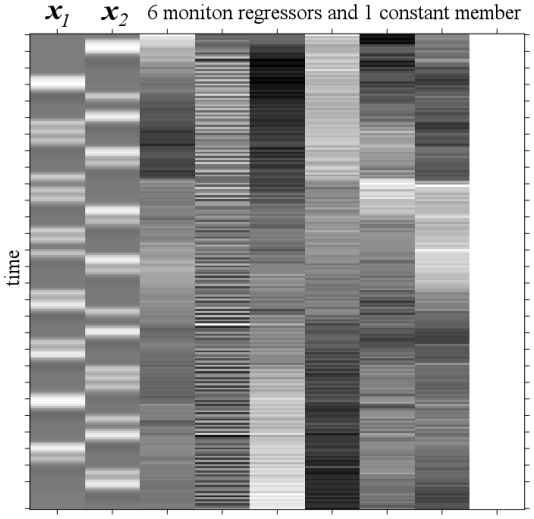

(a) Model matrix $\boldsymbol{X}$

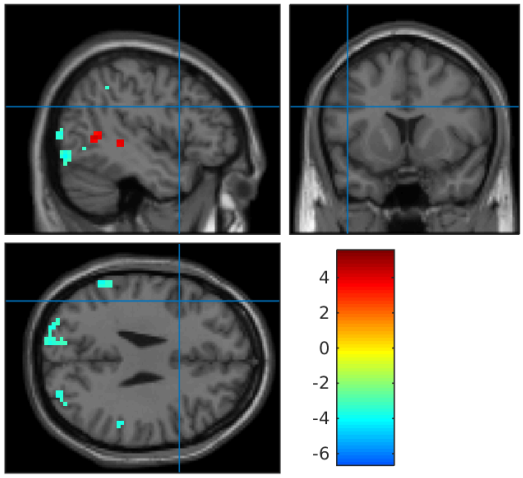

(b) T-test SPM for regressor $\boldsymbol{x}_1$

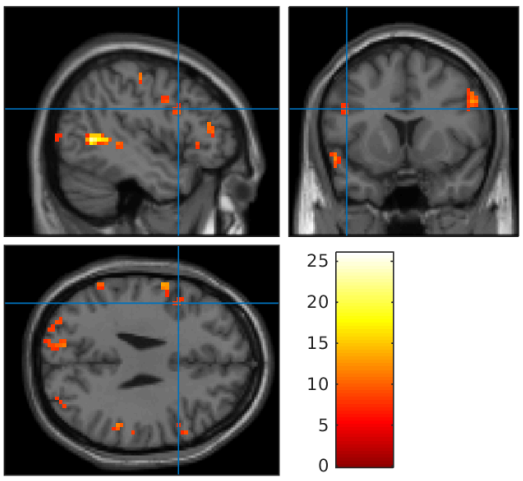

(c) F-test SPM for $\boldsymbol{x}_1$ and $\boldsymbol{x}_2$

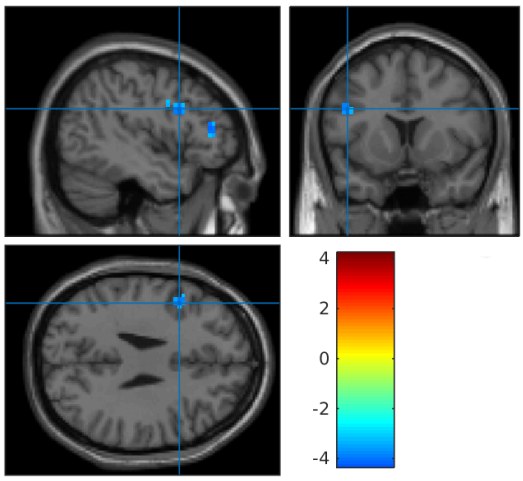

(d) T-test SPM for regressor $\boldsymbol{x}_2$

Fig. 1.3: Examples of single-subject 3D T-test and F-test based SPMs: Both SPMs are thresholded at level of statistical significance p<0.001 not corrected for multiple comparisons and projected on high-resolution anatomical T1-weighted MR image.

detection of so-called large scale brain networks (LSBNs) [1] predominantly with Independent Component Analysis [40, 92] (ICA) described in the continuous *sub-chapter 1.2 "Independent Component Analysis"*.

1.2 Independent Component Analysis

The ICA [40, 92] is a concurrent widely used neuroscientific data analysis method which does not need to know any information about external stimulus timings, belongs to the group of blind source separation techniques, maximizes the independence between sources with higher order statistics, and is able to visualize functionally connected brain areas from fMRI data [146]. The areas were initially called resting-state networks (RSNs) since they have been proven on resting-state datasets [1, 44, 141, 204]. Soon it became clear that they are observable whether external task is or is not presented and they started to be called large scale brain networks (LSBNs) [32, 142, 192]. Beside fMRI area, the ICA has wide application in EEG [23, 47, 105, 193] and MEG [57, 171] signal processing [94, 208].

The ICA algorithm (eq. 1.12) decomposes the original data $\boldsymbol{Y}$ at source matrix $\boldsymbol{S}$ where each row contains an orthogonal and independent component, and at mixing matrix $\boldsymbol{A}$ of estimated coefficients which characterizes the linear relationship between the original data and independent components [40, 92].

$$\boldsymbol{Y} = \boldsymbol{A}\boldsymbol{S} \tag{1.12}$$

If the dimensions of input matrix are $\boldsymbol{Y}(n_t, n_w)$ where n_t is number of time-points and n_w is number of voxels, we are talking about so-called spatial ICA [30, 33]. Then, the output matrices have dimensions $\boldsymbol{A}(n_t, n_c)$ and $\boldsymbol{S}(n_c, n_w)$, where n_c is number of estimated components (mostly ad-hoc set). In this case, each row of matrix $\boldsymbol{S}$ consists one 3D spatially orthogonal and independent component with highly correlated timecourses over all supra-thresholded voxels. The component's characteristic timecourse is hidden in corresponding column of matrix $\boldsymbol{A}$. It is mostly used ICA approach in fMRI area [1, 23, 32, 44, 141, 142, 146, 192, 204]. An example of one output IC with its timecourse and timecourse's power spectral density is shown in Fig. 1.4.

If the dimensions of input matrix are $\boldsymbol{Y}(n_w, n_t)$, then the output dimensions are $\boldsymbol{A}(n_w, n_c)$ and $\boldsymbol{S}(n_c, n_t)$, and the analysis is called temporal ICA [30, 33]. It is poorly used in fMRI area [18, 201] but widely used e.g. in EEG/MEG signal analysis and filtering [47, 57, 92, 105, 138, 193, 194, 208] where variable n_w characterizes number of leads. An example of temporal ICA EEG output is shown in Fig. 1.5.

Several optimizing techniques for eq. 1.12 estimations have been developed since 1994 when the ICA was initially presented. Their brief review is shown in the *sub-chapter 1.2.1 "ICA cost functions and optimizing algorithms"*. The strategies for blind-source decomposition of eq. 1.12 can be divided at single-subject [146] and multi-subject [31] techniques whose brief review is listed in the *sub-chapter 1.2.2 "ICA multi-subject extension"*.

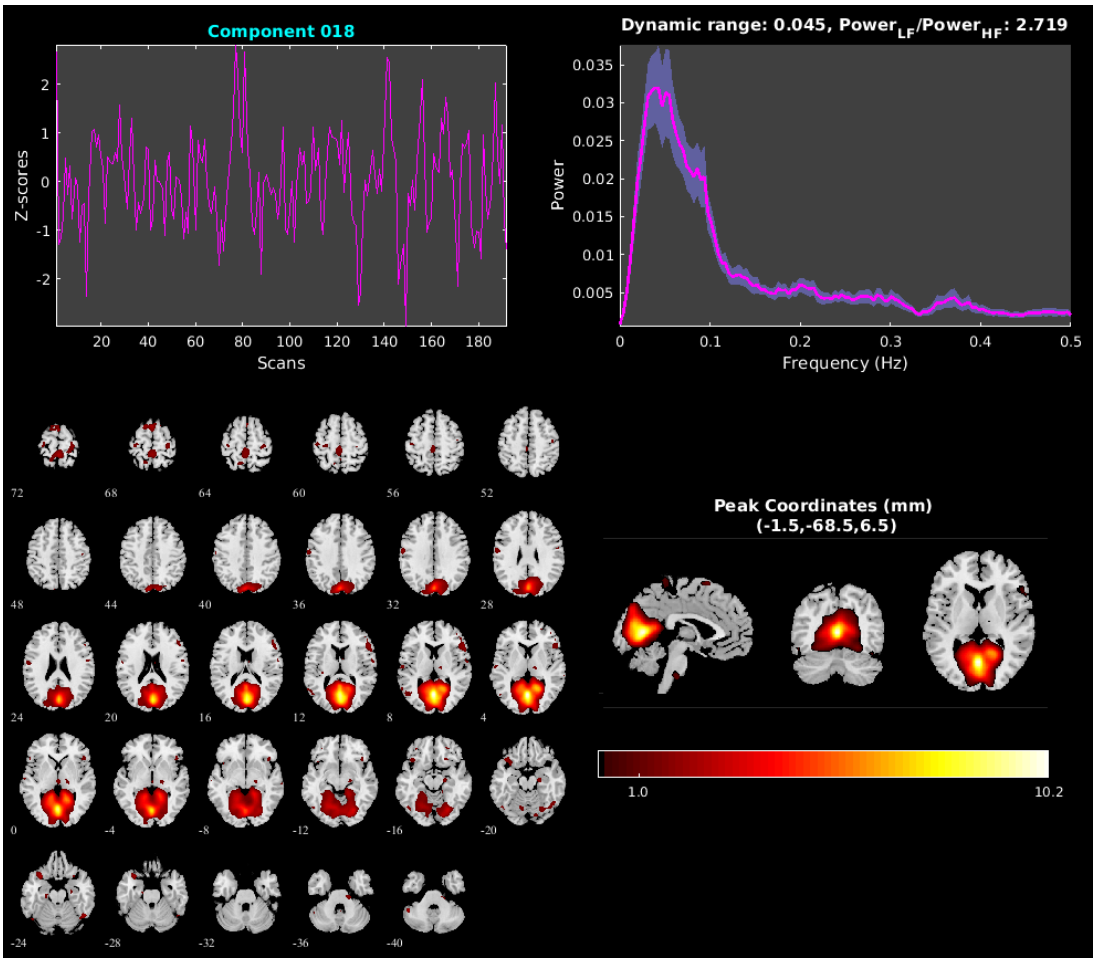

Fig. 1.4: Example of spatial-ICA output on resting-state fMRI data: *(down)* The output component characterizes the z-scored functional connectivity of visual cortex. *(left up)* The graph contains the averaged z-scored timecourse of the component. *(right up)* The graph describes the timecourse's power spectral density and its variability.

1.2.1 ICA cost functions and optimizing algorithms

Since everytime we are solving overdetermined problem of eq. 1.12 we can rewrite it after dimensionality reduction (e.g. with principal component analysis - PCA [104]) as eq. 1.13 where $\boldsymbol{y}, \boldsymbol{s} \in \mathbb{R}^{n_t}$, $\boldsymbol{A}$ is a full-rank square mixing matrix characterizing a linear mixture between as many observations y_t as sources (respectively components) s_t [31].

$$\boldsymbol{y}(w) = \boldsymbol{A}\boldsymbol{s}(w) \qquad 1 \leq w \leq n_w \tag{1.13}$$

In the current equation 1.13, the index w can be time (as in case of temporal-ICA), or a spatial or volume index (as in case of spatial-ICA). Then, the $y_t(w)$ and

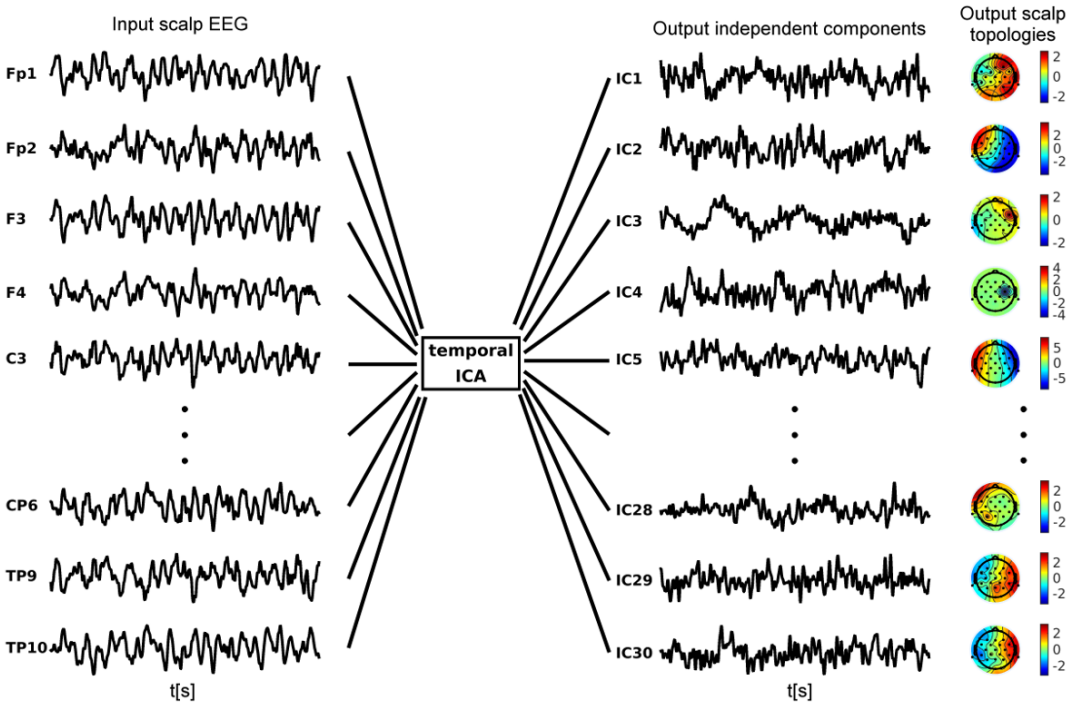

Fig. 1.5: Example of temporal-ICA output on visual oddball EEG data: Scalp topologies are projections of column coefficients of mixing matrix $\boldsymbol{A}$ for the corresponding component.

$s_t(w)$ can be considered for the t-th random process in $\boldsymbol{y}(w)$ and $\boldsymbol{s}(w)$. And when we have a set of observations $\boldsymbol{Y} \in \mathbb{R}^{n_t \times n_w}$, each row $\boldsymbol{y}_t^T$ reffers to a realization of n_w-dimensional random vector. Assuming that the sources are mutually independent, the demixing matrix $\boldsymbol{B}$ (eq. 1.14) forming the sources $\boldsymbol{s}(w)$ can be estimated using the assumptions about the data properties [31].

$$\boldsymbol{u}(w) = \boldsymbol{B}\boldsymbol{y}(w) \tag{1.14}$$

Data's non-Gaussianity is the most often used property, when the decomposition is solved with higher order statistics (HOS) where mutual information cost function $I_r(\boldsymbol{B})$ is optimized with maximum likelihood (ML) approaches most frequently [90, 92, 167], or with maximization of negentropy [159], or with explicit joint approximation diagonalization of eigenmatrices (JADE) [35]. Its natural formula can be written as eq. 1.15, where $H_r(u_t)$ is the entropy rate of t-th source estimate $\boldsymbol{u}_t$ and $H_r(\boldsymbol{y})$ is the constant entropy rate of observations with respect to $\boldsymbol{B}$ [31].

$$I_r(\boldsymbol{B}) = \sum_{t=1}^{n_t} H_r(u_t) - \log|\det(\boldsymbol{B})| - H_r(\boldsymbol{y}) \tag{1.15a}$$

$$H_r(u_t) = \lim_{k\to\infty} H[u_t(1), ..., u_t(k)]/k \tag{1.15b}$$

$$H_r(\boldsymbol{y}) = \lim_{k\to\infty} H[y(1), ..., y(k)]/k \tag{1.15c}$$

Because of mentioned properties, the statistical dependence over separated sources $\boldsymbol{u}_t$ is minimized by minimizing of the total entropy rate of all source estimates $\sum_{t=1}^{n_t} H_r(u_n)$. The regularization term $\log|\det(\boldsymbol{B})|$ penalizes ill-conditioned matrices and reduces eq. 1.15a to maximization of negentropy as the cost function. The most commonly used form assuming non-Gaussianity is eq. 1.16a, where independent and identically distributed (i.i.d.) samples (sample correlation ≈ 0) are assumed for observation matrix $\boldsymbol{Y} \in \mathbb{R}^{n_t \times n_w}$ and where "$\log p_{s_t}(u_t)$" is the source probability density function [31]. Variable $\boldsymbol{b}_t$ in eq. 1.16b is t-th row of the demixing matrix $\boldsymbol{B}$.

$$L(\boldsymbol{B}) = \sum_{w=1}^{n_w}\sum_{t=1}^{n_t} \log p_{s_t}(u_t) + n_w \log|\det(\boldsymbol{B})| \tag{1.16a}$$

$$u_t(w) = \boldsymbol{b}_t^T \boldsymbol{y}(w) \tag{1.16b}$$

The eq. 1.16 leads to the popular INFOMAX algorithm [12] with many ML forms using different density models (e.g. entropy bound minimization [135], or FastICA algorithm where demixing matrix $\boldsymbol{B}$ is constrained to be orthogonal eq. 1.17 [90], or efficient FastICA form called EFICA [114], etc.).

$$\boldsymbol{B}\boldsymbol{B}^T = \boldsymbol{I} \tag{1.17}$$

Except HOS algorithms expecting i.i.d. samples, second order blind identification (SOBI) [13, 219] and weights-adjusted SOBI (WASOBI) [218, 220] techniques were released for ICA estimations. They are able to differentiate several Gaussian sources with linear dependent non-zero covariance matrices $\boldsymbol{R}$ (eq. 1.18), e.g. based on diagonalization of those covariance matrices $\boldsymbol{R}$ [13].

$$\boldsymbol{R}_t = l\boldsymbol{R}_q \qquad\qquad l \neq 0 \tag{1.18}$$

The multi-subject extension of the INFOMAX algorithm [12] using fixed density model was used within the EEG data analysis pipeline of the current thesis. The multi-subject extension brings us to the following *sub-chapter 1.2.2 "ICA multi-subject extension"*.

1.2.2 ICA multi-subject extension

Any ICA can be performed at single-subject level or multi-subject level to aggregate group averaged independent components. Multi-subject extension is called group Indepdendent Component Analysis (gICA) [29, 31, 33, 55] and consists of several stages listed in Fig. 1.6 borrowed from [31].

Each gICA starts with reduction of data dimensions, most often with two-stage PCA [104]. Over various different implementations yielding to similar results, the

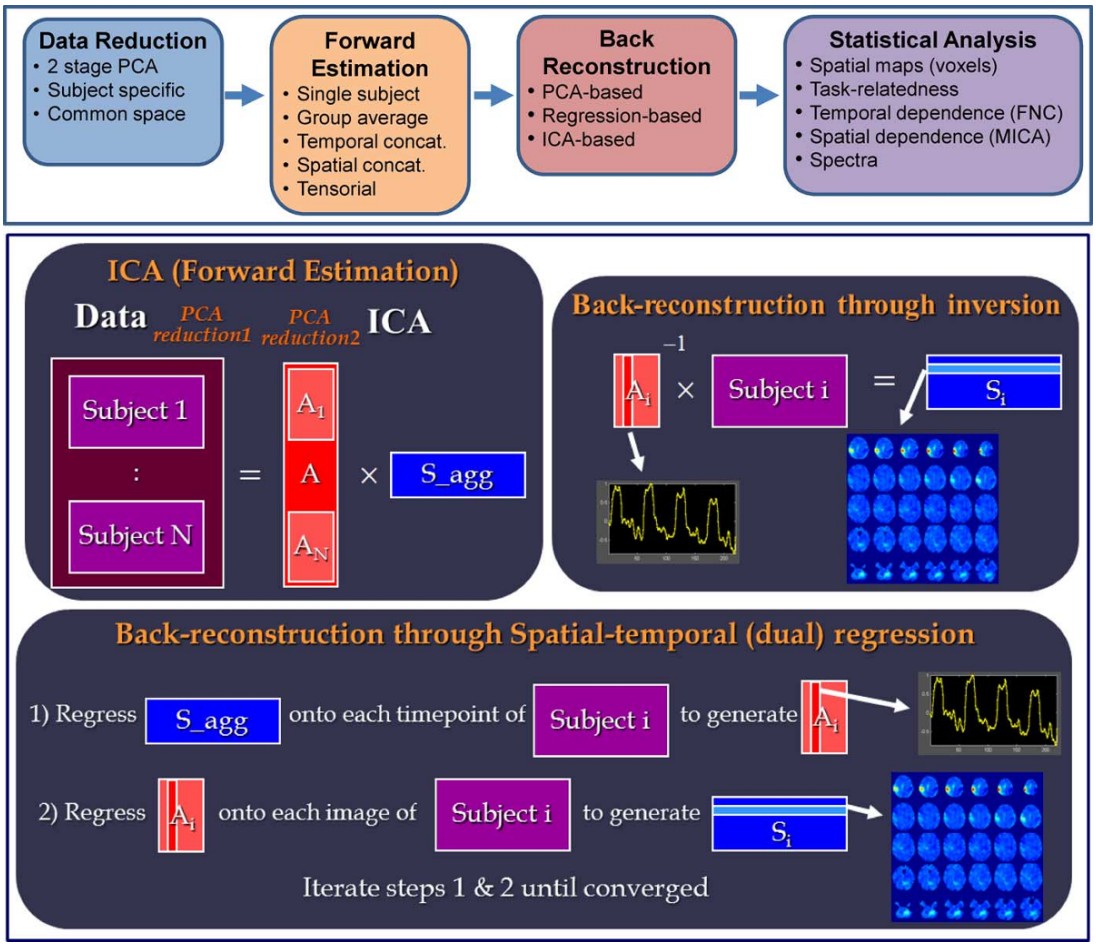

Fig. 1.6: Stages of gICA for spatial ICA of fMRI data: (The picture was borrowed from [31].) The detailed *"ICA (Forward Estimation)"* block illustrates temporally concatenated input data (after two-stage PCA), estimated mixing matrix $\boldsymbol{A}$ (containing subject specific mixing matrices $\boldsymbol{A}_i$ where $i \in \{1, 2, ..., N\}$) and group-averaged source matrix $\boldsymbol{S}_{agg}$. The *"Back-reconstruction through inversion"* block illustrates the basic principals of subject-specific source matrix $\boldsymbol{S}_i$ estimation which is used e.g. in PCA-based back-reconstructions [29]. The *"Back-reconstruction through Spatial-temporal (dual) regression"* block highlights the basic ideas of dual regression [9, 34] via two continuous GLMs as the concurrent back-reconstruction technique.

simple idea of the two-stage PCA can be summarized as follows. The first stage is estimated on single-subject level as separate PCA for each subject and session, and the second stage is estimated as PCA of concatenated reduced single-subject data on group level [31, 33, 55]. More detailed description of data dimensionality reduction via PCA is writen in *sub-chapter 1.2.3 "Data dimensionality reduction with two-stage PCA"* Concurrent to the two-stage PCA, clustering can be the other approach reducing the data dimensions on group level [27, 91, 93].

After the data dimension reduction, ICA Forward Estimation follows with five possible strategies as shown in Fig. 1.7. The first strategy (not-shown in Fig. 1.7) averages the data over subjects and makes the ICA on group-averaged data [185]. For well working ICA, this assumption presume common time courses and sources over subjects. So, list of experiments where the method is applicable is limited. The second strategy incorporates single-subject ICA estimates following with group inferences based on correlations over sources [28, 29], or retrospective matching [125], or clustering [56, 91, 93]. The big advantage of this approach is the ability to reveal unique single-subject spatial and temporal features. But simultaneously, the method fails for noisy data, where the noise can cause changes in ICA estimates which disable precise group evaluations [31].

The other three groups (temporal concatenation, spatial concatenation and tensor calculus) involve direct ICA estimations on group data (see Fig. 1.7). Both, temporal and spatial concatenations follows with one ICA calculus with subject specific parts over mixing or source matrices. For the temporal concatenation,

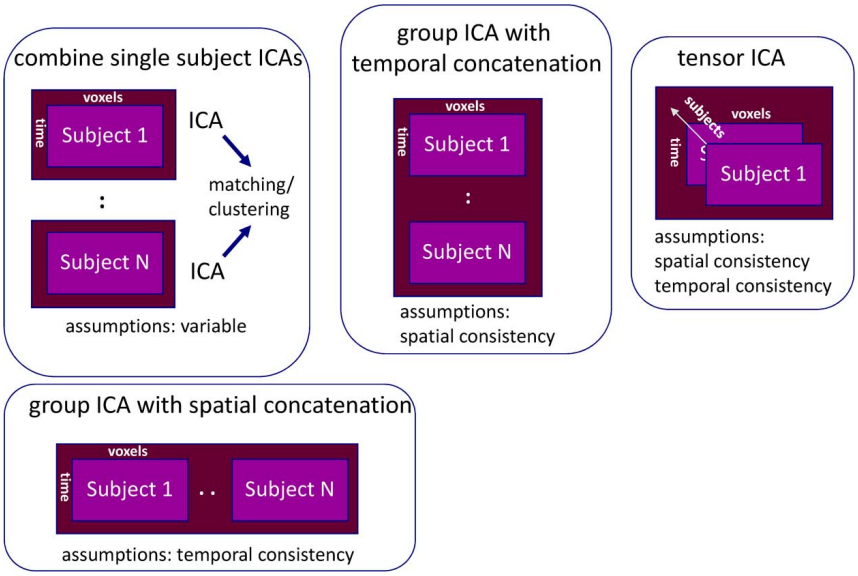

Fig. 1.7: Forward estimation approaches for spatial ICA of fMRI data: (The picture was borrowed from [31].)

we are getting one common source matrix and one group mixing matrix divisible into several subject-specific mixing sub-matrices. Hence, differences over subjects' time courses can be examined immediately, and over their sources after back-reconstruction [29, 2]. Similarly for the spatial concatenation, we are getting one common time course matrix, source matrix divisible into several subject-specific source sub-matrices and differences in time courses comparable over subjects after back-reconstruction [31]. Since both concatenations have been used and examined for fMRI data [29, 198], the temporal concatenation seems to work better possibly because of larger variance over time than over brain's volume space [31, 185]. Beside fMRI application, the *"temporal concatenation"* over trials [52] or epochs [21, 23, 120] also finds its application in EEG signal group blind source decompositions.

The last tensorial extension estimates a common time course matrix and a common source matrix but also allows to estimate subject specific matrices [10]. Although that method is still under development, its application will possibly be still limited since it assumes common time courses. So, it fails when they differ over subjects, e.g. resting state experiment or experiments with randomized events [31].

1.2.3 Data dimensionality reduction with two-stage PCA

Let $\boldsymbol{Z}$ be some input data matrix with dimensions $\boldsymbol{Z}(n_t, n_w)$ representing n_t-dimensional, zero mean, random row vector Z. Then, its covariance matrix $\boldsymbol{\Sigma}_Z$ can be rewritten as eq. 1.19 after singular value decomposition (SVD) at matrix of eigenvectors $\boldsymbol{F}_{n_t}$ and diagonal matrix of eigenvalues $\boldsymbol{e}_{n_t}$ [55, 104].

$$\boldsymbol{\Sigma}_Z = \boldsymbol{F}_{n_t} \boldsymbol{e}_{n_t} \boldsymbol{F}_{n_t}^T \tag{1.19}$$

Let the eigenvectors in matrix $\boldsymbol{F}_{n_t}$ and the eigenvalues in diagonal matrix $\boldsymbol{e}_{n_t}$ be ordered in descending trend of eigenvalues, then the first eigenvector specifies the direction of largest data variance. And, the eq. 1.19 can be rewritten as eq. 1.20 where matrices $\boldsymbol{F}$ and $\boldsymbol{e}$ of the first n_{t1} ordered eigenvectors and eigenvalues and forms the n_{t1} orthogonal basis [29, 31, 55].

$$\boldsymbol{\Sigma}_Z = \begin{bmatrix} \boldsymbol{F} & \boldsymbol{F}_2 \end{bmatrix} \begin{bmatrix} \boldsymbol{e} & 0 \\ 0 & \boldsymbol{e}_2 \end{bmatrix} \begin{bmatrix} \boldsymbol{F}^T \\ \boldsymbol{F}_2^T \end{bmatrix} \tag{1.20}$$

The best linear predictor (BLP) of $\boldsymbol{Z}$ is $\breve{\boldsymbol{Z}}$ (eq. 1.21) optimal in mean squared error (MSE) where $P_{C(\boldsymbol{F})} = \boldsymbol{F}\boldsymbol{F}^T$ is the perpendicular projection operator (PPO) onto the column space of $\boldsymbol{F}$, $C(\boldsymbol{F})$, since $\boldsymbol{F}$ is orthonormal [55].

$$\breve{\boldsymbol{Z}} = \boldsymbol{F}\boldsymbol{e}\boldsymbol{e}^{-1}\boldsymbol{Z}^* = \boldsymbol{F}\boldsymbol{F}^T\boldsymbol{Z} = P_{C(\boldsymbol{F})}\boldsymbol{Z} \tag{1.21}$$

The Moore-Penrose pseudoinverse simplifies the pseudoinverse at eq. 1.22 [55]. Since eq. 1.22 applies, the PCA-reduced data $\boldsymbol{Z}^*$ can be expressed as n_{t1} basis vectors of the orthogonal basis as eq. 1.23 [55].

$$\boldsymbol{Z}^- = (\boldsymbol{Z}^T\boldsymbol{Z})^{-1}\boldsymbol{Z}^T = \boldsymbol{Z}^T \tag{1.22}$$

$$\boldsymbol{Z}^* = \boldsymbol{F}^-\boldsymbol{Z} = \boldsymbol{F}^T\boldsymbol{Z} \tag{1.23}$$

Let $\boldsymbol{Y}_i$ be a input data matrix of subject i with dimensions $\boldsymbol{Y}(n_t, n_w)$ (preprocessed and normalized to the same template space) with zero mean of each row. Then the group temporally concatenated data can be expressed as eq. 1.24 for M subjects. The subject specific predicted data $\breve{\boldsymbol{Y}}_i$ after temporal concatenation can be expressed as eq. 1.25. The single-subject PCA reduced data is characterized with eq. 1.26 where $\boldsymbol{F}_i^- = \boldsymbol{F}_i^T$ is standardized reducing matrix with dimensions $\boldsymbol{F}_i^-(n_{t1}, n_w)$. Temporally concatenated first PCA reduced data can be finally written as eq. 1.27 where $\boldsymbol{Y}^*$ has dimensions $\boldsymbol{Y}^*(Mn_{t1}, n_w)$ [29, 31, 55].

$$\boldsymbol{Y} \equiv \left[\boldsymbol{Y}_1^T, \quad \ldots, \quad \boldsymbol{Y}_M^T\right]^T \tag{1.24}$$

$$\breve{\boldsymbol{Y}}_i = \boldsymbol{F}_i\boldsymbol{Y}_i^* = \boldsymbol{F}_i\boldsymbol{F}_i^-\boldsymbol{Y}_i = P_{C(\boldsymbol{F}_i)}\boldsymbol{Y}_i \tag{1.25}$$

$$\boldsymbol{Y}_i^* = \boldsymbol{F}_i^-\boldsymbol{Y}_i = \boldsymbol{F}_i^T\boldsymbol{Y}_i \tag{1.26}$$

$$\boldsymbol{Y}^* \equiv \left[\boldsymbol{Y}_1^{*T}, \quad \ldots, \quad \boldsymbol{Y}_M^{*T}\right]^T \tag{1.27}$$

For the first-stage PCA reduction of spatially concatenated data, the standardized reducing matrix $\boldsymbol{F}_0^- = \boldsymbol{F}_0^T$ with dimensions $\boldsymbol{F}_0^-(n_{t1}, n_t)$ is calculated from concatenated data (eq. 1.24) of dimensions $\boldsymbol{Y}(n_t, Mn_w)$. The subject specific predicted data $\breve{\boldsymbol{Y}}_{0i}$ after spatial concatenation can be expressed as eq. 1.28. Then, the $\boldsymbol{Y}^*$ are temporally concatenated as in eq. 1.27 but with reducing step of eq. 1.29 [10, 29, 31, 55].

$$\breve{\boldsymbol{Y}}_{0i} = \boldsymbol{F}_0\boldsymbol{Y}_i^* = \boldsymbol{F}_0\boldsymbol{F}_0^-\boldsymbol{Y}_i = P_{C(\boldsymbol{F}_0)}\boldsymbol{Y}_i \tag{1.28}$$

$$\boldsymbol{Y}_i^* = \boldsymbol{F}_0^-\boldsymbol{Y}_i = \boldsymbol{F}_0^T\boldsymbol{Y}_i \tag{1.29}$$

The group data mean PCA method is the last available first-stage PCA for single-subject data dimension reduction. Mean dataset over subjects is estimated in the first step with eq. 1.30 and enters to first PCA to obtain $\boldsymbol{F}_0^- = \boldsymbol{F}_0^T$ matrix

with dimensions $\boldsymbol{F}_0^-(n_{t1}, n_t)$. The subject specific predicted data $\breve{\boldsymbol{Y}}_{0i}$ after group mean estimation can be expressed as eq. 1.31. Then, the second subject-level PCA is performed to rotate each of the $\boldsymbol{F}_0^{-1}\boldsymbol{Y}_i$ to the principal directions of each subject reduced data $\boldsymbol{Y}_i^*$ (eq. 1.32) with dimensions $\boldsymbol{Y}_i^*(n_{t1}, n_t)$ [11, 31, 55].

$$\overline{\boldsymbol{Y}} = M^{-1}\sum_{i=1}^{M}\boldsymbol{Y}_i \tag{1.30}$$

$$\breve{\boldsymbol{Y}}_{0i} = \boldsymbol{F}_0\boldsymbol{F}_i\boldsymbol{F}_i^-\boldsymbol{F}_0^-\boldsymbol{Y}_i = P_{C(\boldsymbol{F}_i\boldsymbol{F}_0)}\boldsymbol{Y}_i \tag{1.31}$$

$$\boldsymbol{Y}_i^* = \boldsymbol{F}_i^-\boldsymbol{F}_0^-\boldsymbol{Y}_i = \boldsymbol{F}_i^T\boldsymbol{F}_0^T\boldsymbol{Y}_i \tag{1.32}$$

The second-stage PCA reduces the data $\boldsymbol{Y}^*$ of dimensions $\boldsymbol{Y}^*(Mn_{t1}, n_w)$ at aggregate matrix $\boldsymbol{H}$ (eq. 1.33) of dimensions $\boldsymbol{H}(n_{t2}, n_w)$, when applies: $n_{t2} < n_{t1} < n_t$. The matrix $\boldsymbol{G}^-$ in eq. 1.33 is the standardized reducing matrix of dimensions $\boldsymbol{G}(n_{t2}, Mn_{t1})$ [29, 31, 55].

$$\boldsymbol{H} \equiv \boldsymbol{G}^-\boldsymbol{Y}^* = \begin{bmatrix}\boldsymbol{G}_1^T, & \ldots, & \boldsymbol{G}_M^T\end{bmatrix}\begin{bmatrix}\boldsymbol{F}_1^-\boldsymbol{Y}_1 \\ \vdots \\ \boldsymbol{F}_M^-\boldsymbol{Y}_M\end{bmatrix} = \sum_{i=1}^{M}\boldsymbol{G}_i^T\boldsymbol{F}_i^T\boldsymbol{Y}_i = \sum_{i=1}^{M}\boldsymbol{H}_i \tag{1.33}$$

The predicted subject-compressed data $\breve{\boldsymbol{Y}}^*$ can be expressed with eq. 1.34. Then, the matrix $\breve{\breve{\boldsymbol{Y}}}_i$ in eq. 1.35 characterizes the predicted subject data [31, 33, 55].

$$\breve{\boldsymbol{Y}}^* = \boldsymbol{G}\boldsymbol{G}^-\boldsymbol{Y}^* = P_{C(\boldsymbol{G})}\boldsymbol{Y}^* = \begin{bmatrix}\boldsymbol{G}_1\sum_{i=1}^{M}\boldsymbol{G}_i^T\boldsymbol{F}_i^T\boldsymbol{Y}_i \\ \vdots \\ \boldsymbol{G}_M\sum_{i=1}^{M}\boldsymbol{G}_i^T\boldsymbol{F}_i^T\boldsymbol{Y}_i\end{bmatrix} \tag{1.34}$$

$$\breve{\breve{\boldsymbol{Y}}}_i = \boldsymbol{F}_i\breve{\boldsymbol{Y}}^* = \boldsymbol{F}_i\boldsymbol{G}_i\boldsymbol{H} = \boldsymbol{F}_i\boldsymbol{G}_i\sum_{i=1}^{M}\boldsymbol{G}_i^T\boldsymbol{F}_i^T\boldsymbol{Y}_i \tag{1.35}$$

The reduced and aggregate matrix $\boldsymbol{H}$ serves as the input to some ICA algorithm (see *sub-chapter 1.2.1 "ICA cost functions and optimizing algorithms"*) estimating eq. 1.36, where the generative linear latent variables $\hat{\boldsymbol{A}}$ and $\hat{\boldsymbol{S}}$ are the mixing matrix of dimensions $\hat{\boldsymbol{A}}(n_{t2}, n_{t2})$ related to subject time courses and the aggregate source matrix of dimensions $\hat{\boldsymbol{S}}(n_{t2}, n_w)$ [31, 33, 55, 92].

$$\boldsymbol{H} = \hat{\boldsymbol{A}}\hat{\boldsymbol{S}} \tag{1.36}$$

After estimation of group aggregated components in the matrix $\hat{\boldsymbol{S}}$, the single subject components (respectively sources) and their time courses can be estimated with the back-reconstruction which is described in more details within following *sub-chapter 1.2.4 "Back-reconstruction to single subject estimates"*.

1.2.4 Back-reconstruction to single subject estimates

The back-reconstruction methods serve to reveal the subject-specific time courses and sources from group aggregated results, and can be divided into 2 groups:

1. Method called GICA, revealing the single-subject mixing and source matrices from PCA projected and compressed data using direct inversion [29, 31, 33, 55].
2. Spatio-temporal regression (STP; or dual regression), using aggregated matrices as regressors in 2 following GLMs as schematically shown in Fig. 1.6 [9, 34, 55].

Only the first group has been used within the current thesis. The GICA methods can be divided into 3 groups. The youngest approach called GICA3 assumes that the subject specific TCs $\boldsymbol{R}_i$ are the subject specific PCA back-projected mixing matrix, as written in 1.37. Natural estimator $\tilde{\boldsymbol{R}}_i$ and the subject specific back-projection (eq. 1.38) are characterized with substituting of $\boldsymbol{A}$ by aggregated mixing matrix $\hat{\boldsymbol{A}}$ [31, 55].

$$\boldsymbol{R}_i \equiv \boldsymbol{F}_i(\boldsymbol{G}_i^T)^- \boldsymbol{A} = \boldsymbol{F}_i\boldsymbol{G}_i(\boldsymbol{G}_i^T\boldsymbol{G}_i)^{-1}\boldsymbol{A} \tag{1.37}$$

$$\tilde{\boldsymbol{R}}_i \equiv \boldsymbol{F}_i(\boldsymbol{G}_i^T)^- \hat{\boldsymbol{A}} = \boldsymbol{F}_i\boldsymbol{G}_i(\boldsymbol{G}_i^T\boldsymbol{G}_i)^{-1}\hat{\boldsymbol{A}} \tag{1.38}$$

Since eqs. 1.33 and 1.36 can be rewritten as eq. 1.39, the subject specific reduced data $\boldsymbol{H}_i$ can be expressed as eq. 1.40. The natural estimator for subject specific SMs $\tilde{\boldsymbol{S}}_i$ is than eq. 1.41 [31, 55].

$$\boldsymbol{H} = \sum_{i=1}^{M} \boldsymbol{H}_i = \sum_{i=1}^{M} \boldsymbol{G}_i^T\boldsymbol{F}_i^T\boldsymbol{Y}_i = \hat{\boldsymbol{A}}\sum_{i=1}^{M} \boldsymbol{S}_i = \hat{\boldsymbol{A}}\hat{\boldsymbol{S}} \tag{1.39}$$

$$\boldsymbol{H}_i = \boldsymbol{G}_i^T\boldsymbol{F}_i^T\boldsymbol{Y}_i = \hat{\boldsymbol{A}}\boldsymbol{S}_i \tag{1.40}$$

$$\tilde{\boldsymbol{S}}_i = \hat{\boldsymbol{A}}^-\boldsymbol{G}_i^T\boldsymbol{F}_i^T\boldsymbol{Y}_i \tag{1.41}$$

The oldest GICA1 method estimates subject specific TCs $\hat{\boldsymbol{R}}_i$ with eq. 1.42, and SMs $\hat{\boldsymbol{S}}_i$ with eq. 1.43 [29, 55]. The hybrid approach GICA2 uses eq. 1.42 for the TC estimations, and eq. 1.41 for the SM estimations [55].

$$\hat{\boldsymbol{R}}_i \equiv \boldsymbol{F}_i\boldsymbol{G}_i\hat{\boldsymbol{A}} \tag{1.42}$$

$$\hat{\boldsymbol{S}}_i = \hat{\boldsymbol{A}}^-\boldsymbol{G}_i\boldsymbol{F}_i^T\boldsymbol{Y}_i = \hat{\boldsymbol{A}}^-(\boldsymbol{G}_i^T\boldsymbol{G}_i)^{-1}\boldsymbol{G}_i^T\boldsymbol{F}_i^T\boldsymbol{Y}_i \tag{1.43}$$

1.2.5 Model order and stability of ICA

The quality and relevance of final ICA estimates are sensitive to several ad-hoc analysis settings, e.g. number of used principal components, number of final independent components, optimizing algorithm, single-subject or multi-subject estimations, etc.

The final number of ICA components seems to be the crucial input parameter, while low set number is not able to divide more present independent data phenomenons and very high set number shatters the one independent phenomenon at more divided sub-phenomenons. For that reasons, several information theoretic criteria (ITC) were derived to make automatic data-driven selection of the model order [31]. The criteria are able to estimate optimal number of set components for a given input data. The most commonly used ITC are Akaike's information criterion (AIC) [37], Kullback-Leibler information criterion (KIC) [37] and the maximum description length (MDL; or so-called Bayesian information criterion - BIC) [175, 186]. Li et al. (2007) showed the applicability of those criteria within ICA of fMRI data, when they introduced sub-sampling scheme for effective automatic obtaining of set of independent and identically distributed (i.i.d.) samples [136].

The stability of the estimated ICs is the other crucial and qualitative parameter which can be quantitatively measured and optimized. One possible solution brought Himberg, Hyvärinen and Esposito et al. (2003-2005) with their software called ICASSO which makes more ICA runs with same analysis settings, but with different and random initial prior conditions. After several runs, the global optimum is finding with hierarchical clustering algorithm, since the compactness of each cluster is evaluated via the "*cluster quality index*" (I_q, eq. 1.45) [56, 79, 80].

Let C to be a set of indices of all estimated components, C_m to be the set of indices belonging to the m-th cluster, $|C_m|$ to be the size of the m-th cluster, C_{-m} to be the set of indices not-belonging to the m-th cluster, $\boldsymbol{R}$ (eq. 1.44) to be the mutual correlation matrix, $\boldsymbol{\Sigma_Y}$ to be the covariance matrix of original data $\boldsymbol{Y}$, $\boldsymbol{Q} = |\boldsymbol{R}|$ to be the similarity matrix, and $q_{i,j}$ to be the scalar value in matrix $\boldsymbol{Q}$. Then, the cluster quality index (I_q, eq. 1.45) computes the difference between the average intracluster similarities and average intercluster similarities [79, 80].

$$\boldsymbol{R} = \boldsymbol{B}\boldsymbol{\Sigma_Y}\boldsymbol{B}^T \tag{1.44}$$

$$I_q(C_m) = \frac{1}{|C_m|^2} \sum_{i,j \in C_m} q_{i,j} - \frac{1}{|C_m||C_{-m}|} \sum_{i \in C_m} \sum_{j \in C_{-m}} q_{i,j} \tag{1.45}$$

As expected, it is important to set final number of output components carefully and properly also for ICASSO runs, since the cluster stability indices are decreasing with increasing number of set output components [136].

1.3 EEG-fMRI data fusion

In simultaneous EEG-fMRI, we are not trying to explain the measured BOLD signal $\boldsymbol{y}_w$ with expected theoretical BOLD response $\boldsymbol{x}_1$ as shown in Fig. 1.2 with eq. 1.1, but we are finding how to transform some signal or both signals to become comparable. The motivation is to be able to visualize the functionally relevant brain network without a-prior knowledge of the stimulus timings as a blind search data-driven analysis.

Because of the delayed BOLD signal in front of neural activity with immediate EEG changes [86, 139, 157], the simplest linear way of the signal's comparison describes eq. 1.46. There, the BOLD signal $\boldsymbol{y}$ is equal to some latent EEG signal $\boldsymbol{e}$ derived from raw EEG, down-sapmled to fMRI temporal sampling and convolved with some impulse response function (IRF) $\boldsymbol{h}$ characterizing the BOLD signal delay.

$$\boldsymbol{y} = \boldsymbol{e} * \boldsymbol{h} \tag{1.46}$$

The fixed canonical hemodynamic response function (HRF, Fig. 1.1b) is the most often used IRF for the BOLD signal delay modeling [14, 73, 75, 121, 123, 124, 127, 128, 141, 142, 143, 148, 153, 164, 177, 181, 183, 187, 221]. However, linear combinations of hemodynamic response basis functions [61] better accounts for differences in HRF shape and timings across subjects and brain areas [97, 131, 144, 178]. Alternatively, HRFs may be estimated in a data-driven manner by deconvolution of the EEG and fMRI time courses [23, 46, 215]. Accounting for different IRFs may be useful since the IRF shape differs depending on the fMRI voxel location [45, 46], and the frequency band of the EEG signal that it is related to [23, 45, 46, 144]. Or even within a fMRI voxel location due to hemodynamic changes, including those that results from focal epilepsy [97, 131, 178].

Beside the question of the IRF's proportions, the EEG signal processing into $\boldsymbol{e}$ form (eq. 1.46) becomes much more fundamental problem because we need to fulfil two basic conditions:

1. Transform the raw EEG signal onto comparable form with the BOLD signal.
2. Still keep the advantage of better EEG's temporal resolution inside a transformed signal, although it was down-sampled onto fMRI timings.

Previously most often used transformations of raw EEG signal to the latent $\boldsymbol{e}$ form can be divided at two distinct groups. The 1^{st} approach, initially used for EEG triggering [117, 211] and often implemented on task data, emphasizes the detection of previously defined EEG waveform shapes (i.e. graphoelements), including evoked or event-related potentials (EPs or ERPs) [14, 50, 51, 140, 142, 152, 156] or epileptic spikes [82, 130, 209]. Sometimes EEG source reconstruction (projecting the scalp EEG signal into brain's volume) is used for the fusion within the LORETA algorithm

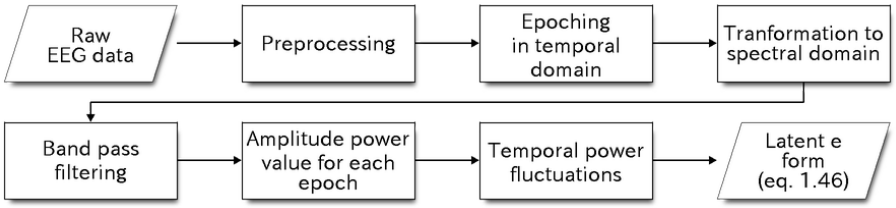

Fig. 1.8: Basic transformation of raw EEG signal into the latent $\boldsymbol{e}$ form: via spectral power fluctuations for the single electrode lead.

(low resolution brain electromagnetic tomography) [156, 166, 209], sometimes parallel ICA is estimated when the parameters of the mixing matrix $\boldsymbol{A}$ (eq. 1.12) are influenced by both signals simultaneously during optimizing process [50, 51, 152], sometimes ERPs are compared with dynamics of independent fMRI functional netwroks [140, 142]. The rest of fusion approaches using predominantly multiple regression analysis between the signals (e.g. [14, 82, 130]).

The 2^{nd} most common approach (which is in the scope of the current thesis) is to integrate EEG spectra with fMRI BOLD signal [23, 45, 46, 73, 75, 81, 108, 121, 123, 124, 126, 127, 128, 141, 143, 144, 145, 148, 153, 168, 177, 181, 183, 184, 187, 215, 221]. The simplest idea of raw EEG signal transformation into the latent form $\boldsymbol{e}$ characterizing the EEG spectra can be described within the block diagram in Fig. 1.8 for the single electrode lead. That idea was used in initial EEG-fMRI fusion studies (2002-2003) predominantly investigating coupling between absolute EEG α-band[5] power and the BOLD signal [73, 127, 128, 153], and keeps not-changed until the most recent articles (2015-2017) already investigating the whole EEG frequency range [123, 221]. Although the basic principle has not changed, there is several ways how the analysis can be performed and how the final results can be influenced and interpreted.

Within the initial studies, the single electrode outputs of fixed frequency band of interest were averaged over set of electrodes of interest, and voxel-wise correlated [73] or regressed [127, 128, 153] with the concurrent simultaneously acquired BOLD signal. The resulting 3D statistical parametric map characterizes the relationship between the latent EEG signal $\boldsymbol{e}$ in each voxel. Since the evidence of stable LSBNs [1, 44] has been noticed in fMRI data, comparison of averaged EEG power fluctuations of distinct frequency band with BOLD dynamics of LSBNs is the other possible way for the data fusion, characterizing the p-value of the statistical significance between both dynamics [81, 141]. Unfortunately for that kind of the EEG processing steps, the strong inter-subject variability [75] and single-subject temporal in-stability [148]

[5] α is the label in the neuroscience literature for the EEG signal's frequency band of interest, typically approximately about 8-12Hz.

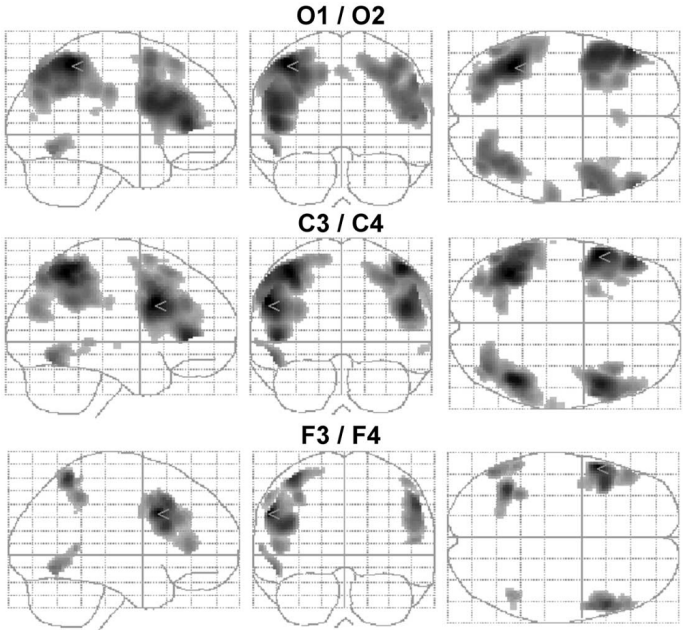

Fig. 1.9: Similar EEG-fMRI results for different electrodes of interest: The results are showing negative coupling between EEG α-band absolute power and BOLD signals in the dorsal attention network for O1/O2, C3/C4 and F3/F4 electrodes. (The picture was borrowed from [127].)

were monitored in EEG-fMRI results. More, it seems that latent EEG signals $\boldsymbol{e}$ from different electrodes are highly correlated in original scalp space and bring quite similar EEG-fMRI results without dependence on choice of electrodes of interest, as noticed directly within the current doctoral thesis [123] and in-directly within concurrent study too (Fig. 1.9) [127]. Beside the electrode averaging problem, we [123] and other researchers [45, 141, 221] are also observing for absolute EEG power that fluctuations of the latent signal $\boldsymbol{e}$ are highly correlated over different frequency bands.

To overcome all mentioned issues, blind source separation (BSS) techniques started to be used during EEG signal transformations at the latent form $\boldsymbol{e}$. The first possible implementation with the temporal ICA of the raw EEG signal [92, 138, 194] is summarized within the block diagram in Fig. 1.10. The current approach was truly and successfully incorporated within several pure EEG [165], interleaved EEG-fMRI [222] and simultaneous EEG-fMRI studies [181, 183, 184], although temporal ICA appears work well for removing eye blink and eye movement artifacts, but appears less successful in decomposing distinct EEG oscillations measured in the absence of an explicit task (i.e. during 'rest') [94, 134].

In order to isolate distinct EEG oscillations (i.e. signal from signal), a variety of approaches have been developed to decompose real valued or complex

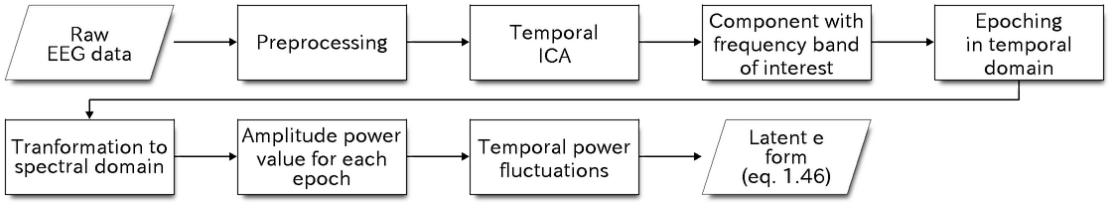

Fig. 1.10: Transformation of raw EEG signal into the latent $\boldsymbol{e}$ form with temporal ICA: Raw EEG signal is transformed from temporal-scalp space to the temporal space of orthogonal and independent components with topology scalp projections (as shown in Fig. 1.5)

valued EEG spectra, or to decompose short distinct raw EEG signals in temporal domain [5, 15, 42, 84, 94, 107, 150, 158, 172, 188, 199, 207]. These approaches are generally applied to individual subjects data, which requires identification of similar components across the separate decompositions. In order to overcome this problem, and in order to aggregate information across the group of subjects, various multi-subject extensions have been developed and implemented [20, 22, 23, 41, 43, 52, 87, 88, 116, 137, 143, 144, 173]. All algorithms for BSS of EEG oscillations are briefly summarized in the *sub-chapter 1.3.1 "Blind source separation of EEG oscilations"*.

Despite isolating of distinct EEG oscillations and localizing their sources, we would like to transform the raw EEG signal into the latent form $\boldsymbol{e}$ characterizing the neuronal activity which would corresponds to the onset of experimental task design. There already exist some work and hypotheses about that issues and they are summarized within the *sub-chapter 1.3.2 "Task-related variability within EEG latent form"*.

The last sub-chapter of the current chapter is called *1.3.3 Limits of the state of the art, and improvement proposals*, emphasizes the limits of the current state of the art and designs the solution proposals which are implemented and tested within the current thesis.

1.3.1 Blind source separation of EEG oscilations

The standard temporal ICA model supposes that the neural activity source comes from the perfectly synchronized manner within spatially fixed cortical domains. This assumption might be too strong, as it does not take into account the possible spatio-temporal dynamics of the underlying neural processes, e.g. propagation of neuronal activity, traveling wave patterns of activity, or synchronization between different brain areas with a non-zero phase [5].

For that reasons, Anemüller et al. (2003) proposed the convolutive ICA of EEG signals as a complex ICA of different spectral bands. Let n_c to be number of channels c, and $d_i(t)$ to be the measured raw EEG signal in time point t where $c \in \{1, 2, ..., n_c\}$. Then, signal's spectral time-frequency representation $d_c(T, \omega)$ can be expressed with eq. 1.47, where ω denotes the frequency and $b_\omega(\tau)$ expresses the basis function which extracts the spectral band ω from the time domain and which is centered at time T [5].

$$d_c(T, \omega) = \sum_\tau d_c(T + \tau) b_\omega(\tau) \tag{1.47}$$

Hence, the data matrix $\boldsymbol{D}$ is transformed from original dimensions $\boldsymbol{D}(n_c, n_t)$ into dimensions $\boldsymbol{D}(n_c, n_T, n_\omega)$. For the short-time Fourier transformation, the basis function $b_\omega(\tau)$ is eq. 1.48, where $l(\tau)$ is a windowing function (e.g. Hanning window) with window length $2K$, $\tau \in \{-K, ..., K-1\}$ and $\omega \in \{0, ..., K\}$ [5].

$$b_\omega(\tau) = l(\tau) e^{-i2\pi\omega\tau/2K} \tag{1.48}$$

For each frequency band ω, the linear mixing model with frequency specific mixing matrix $\boldsymbol{A}(\omega)$ can be written with eq. 1.49 and optimized within some ICA optimizing algorithm. Annemüller et al. (2003) perforemd complex INFOMAX ICA algorithm, since they modelled sources $s_c(T, \omega)$ with complex random variables with a circular symmetric non-Gaussian probability density functions [5].

$$\boldsymbol{D}(T, \omega) = \boldsymbol{A}(\omega) \boldsymbol{S}(T, \omega) \tag{1.49}$$

With wavelet transforms [179, 180] or Cohen's classes [38, 39] for time-frequency transformations, Bernat et al. (2005) built a 2D matrix $\boldsymbol{D}$ of dimensions $\boldsymbol{D}(n_c, n_T * n_\omega)$ consisting of EEG signal energy over electrodes, time and frequencies. That matrix, they decomposed with PCA and classified the components related to ERP timings [15]. Hu et al. (2010,2015) presented that those PCs can be decomposed with time-frequency multiple linear regression at signals related to even-related potentials, event-related desynchronizations and event-related synchronizations [83, 84].

Hyvärinen et al. (2010) built matrix $\boldsymbol{D}$ (of same dimensions as Bernat et al. (2005)) consisting of complex-valued output coefficients of short-time Fourier transform (eqs. 1.47 and 1.48), and implemented the complex FastICA decomposition of eq. 1.50 [16, 94], where the complex mixing matrix $\boldsymbol{A}$ has dimensions $\boldsymbol{A}(n_c, m)$, the source matrix $\boldsymbol{S}$ has dimensions $\boldsymbol{S}(m, n_T * n_\omega)$ and m is a number of decomposed independent components.

$$\boldsymbol{D} = \boldsymbol{A}\boldsymbol{S} \tag{1.50}$$

Shou et al. (2012) performed the same single-subject ICA decomposition of high density EEG data as Hyvarinen et al. (2010) with band-pass filtering (5-30Hz) before the following ICA. As they are writing, this step incorporation should help to the ICA algorithm to choose the frequency-specific signals that are related to neural oscillatory processes, and thus helping the identification of rhythmic brain activations [188]. Kauppi et al. (2013) used current ICA analysis setting, implemented the classifier of the outputting ICs based on Spectral Linear Discriminant Analysis (Spectral LDA) and tested it on MEG data [107]. Congedo et al. (2008, 2010) have brought a concurrent problem solution with the normative ICA which estimates the decomposition with approximate joint diagonalization of Fourier cospectral matrices (AJDC) [42, 43].

All the previous methods belongs to the family of time-frequency analyses and decompositions. The spatio-spectral decomposition is the concurrent analysis strategy able to separate and extract neural oscillations from multi-channel electrophysiological recordings. Wu et al. (2010) built a 2D matrix $\boldsymbol{D}$ of dimensions $\boldsymbol{D}(n_T, n_c * n_\omega)$ consisting of complex coefficients from fast Fourier transform of the raw EEG signal, and estimated group-ICA decomposition (eq. 1.36) of the matrix $\boldsymbol{D}$ with eq. 1.51 at aggregated independent spatiospectral patterns in source matrix $\hat{\boldsymbol{S}}$ of dimensions $\hat{\boldsymbol{S}}(m, n_c * n_\omega)$ and components' aggregated time-courses in mixing matrix $\hat{\boldsymbol{A}}$ of dimensions $\hat{\boldsymbol{A}}(n_T, m)$ whose back-reconstructed forms were comparable with simultaneous single-subject fMRI-BOLD signals [215].

$$\boldsymbol{D} = \boldsymbol{H} = \hat{\boldsymbol{A}}\hat{\boldsymbol{S}} \tag{1.51}$$

Ramkumar et al. (2012) designed quite similar single-subject spatiospectral ICA decomposition as Wu et al. (2010) with the difference that they transformed the spatial information from the scalp space with linear operator to the source space [172]. Simultaneously, they tested concurrent spatial ICA on source spaced EEG data, but the spatiospectral ICA of complex coefficients achieved better results [172].

Bridwell et al. (2013) simplified Wu's et al. (2010) group-ICA spatiospectral approach, since they used only absolute power of originally complex coefficients. Over the simplification, they still found frequency dependent relationships with the simultaneously captured BOLD signal [23]. Bridwell et al. (2016) showed that WASOBI and COMBI appear to be the best optimizing algorithms from 12 tested for the spatiospectral ICA and that WASOBI, COMBI, INFOMAX and FastICA are estimating the largest number of stable sources within real datasets [21].

Bro et al. (1998) introduced the parallel factor analysis (PARAFAC) [24]. Miwakeichi et al. (2004) used it for the direct decomposition of the 3D matrix $\boldsymbol{D}$ of dimensions $\boldsymbol{D}(n_c, n_T, n_\omega)$ at orthogonal components with characteristic and unique

spatial-temporal-spectral pattern for each component [150]. The PARAFAC decomposition of EEG spectra was several times successfully implemented within the simultaneous EEG-fMRI data analysis [143, 144, 145]. As the PARAFAC was initially used only for real values and as complex-ICA exists, the complex-PARAFAC was derived already in 2000 too [189] (but not-used for EEG data analysis). Since the PARAFAC represents 3-way array decomposition with dimensions channels-frequencies-time, van der Meij et al. (2015,2016) presented 4-way array decomposition with dimensions channels-channels-frequencies-time utilizing cross-spectral density matrices able to detect between-channel phase coupling [206, 207].

Except blind decomposition of EEG spectra, blind source separation at orthogonal or independent time-locked spatiotemporal patterns started to be concurrently investigated with several different strategies. Kovacevic and McIntosh (2007) used group-ICA decomposition of short raw EEG trials related to the stimulus timings [116]. Bridwell et al. (2014) showed that kind of analysis is able to find the ERP amplitude decreases for schizophrenic patients within the auditory oddball task [20]. Recently, Takeda et al. (2016) designed the algorithm which is estimating the onsets of the mixture of different spatiotemporal patterns from whole raw records [199].

Eichele et al. (2011) have presented software toolbox called EEGIFT (extending previous GIFT software optimized for fMRI data) optimized for EEG data group-ICA analysis of any possible settings, i.e. time-frequency ICA, spatiospectral ICA or spatiotemporal ICA, with many optimizing methods available (INFOMAX, FastICA, COMBI, SOBI, WASOBI, etc.)[23, 29, 52]. Lio et al. (2013) tested most of optimizing algorithms over themselves during group-ICA estimations and written that the second order statistics based algorithms seems to produce more robust results than higher order statistics or combine hybrid algorithms [137]. It seems to be in line with Bridwell's et al. (2016) conclusions [21].

1.3.2 Task-related variability within EEG latent form

Thu current sub-chapter deals with existing transformations of EEG spectra into forms whose fluctuations are correlated to the external stimulus vector. Klimesch (1999) claims that α-band relative EEG power fluctuations corresponds to the experimental onsets better than the absolute EEG power fluctuations [110]. Kilner et al. (2005) proposed the theoretic heuristic approach comparing EEG and BOLD signals on the level of neuronal activity, since their solution (relation 1.52) expects that changes in BOLD signal b are proportional to neuronal activity a which is proportional to changes in root mean square frequency of whole normalized (relative) EEG power spectrum $p(\omega)$ [108]. The character $\tilde{}$ indicates variables during increased activity, while variables without $\tilde{}$ represent signal values during rest. The normal-

ized (relative) EEG power can be more extensively rewritten with standard spectral density $g(\omega)$ with eq. 1.53.

$$\left[\frac{\tilde{b}}{b}\right]^2 \propto (1+a)^2 \propto \frac{\int \omega^2 \tilde{p}(\omega) d\omega}{\int \omega^2 p(\omega) d\omega} \tag{1.52}$$

$$p(\omega) = \frac{g(\omega)}{\int g(\omega) d\omega} \tag{1.53}$$

Kilner's et al. (2005) heuristic approach expects that three interconnected postulates applies for the EEG signal:

1. The envelope of the signal's spectral density is stable and unchangeable before and after neuronal activation (Fig. 1.11).
2. The raw signal is more rougher after activation and mean root square frequency increases (Fig. 1.11).
3. The described changes are consistent over whole frequency range (Fig. 1.11).

Rosa et al. (2010) simplified Kilner's et al. (2005) theoretic heuristic model at relation 1.54, when they considered the denominators of relation 1.52 for constant members. The simplified heuristic model was able to visualize the stimulated primary visual cortex from simultaneous EEG-fMRI data better than other standard used approaches utilizing absolute EEG power fluctuations [177].

$$\tilde{b} \propto \sqrt{\int \omega^2 \tilde{p}(\omega) d\omega} \tag{1.54}$$

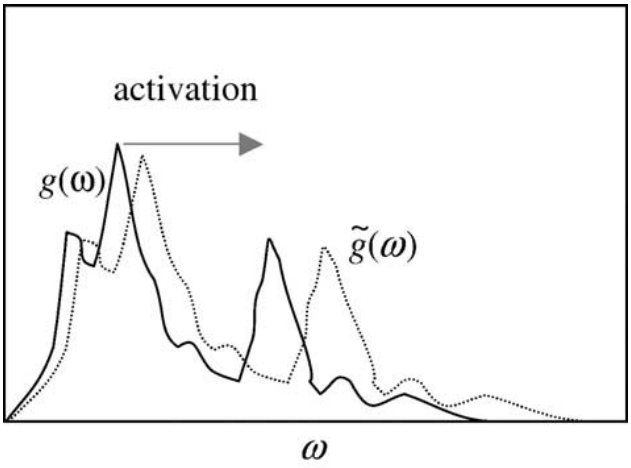

Fig. 1.11: The change of EEG spectral density after neural activation: expected by Kilner et al. (2005); full line - before activation, dotted line - after activation [108].

1.3.3 Limits of the state of the art, and improvement proposals

It is known that different brain rhythms (frequencies) are dominant for different cognitive states [26]. Although Miller (2010) experimentally measured the broadband spectral changes of local field potentials and their shift to higher frequencies after activations of neural tissue [149], the basic heuristic model (eqs. 1.52 and 1.54) [108, 177] neglects the inconsistent changes over different frequencies which are observed e.g. for the EEG α-band rhythm in comparison to the other EEG rhythms [111]. So, we are expecting that it is one of the crucial limitation which is tested within the current Ph.D. thesis.

From the point of view of the statistics and random variable theories, the expression $\int \omega^2 \tilde{p}(\omega)$ characterizes truly the mean root square frequency because it is the 2^{nd} order moment of the random variable ω, since eq. 1.55 applies for the random variable x.

$$EX(x) = \int x^2 p(x) dx \tag{1.55}$$

But from the point of view of signal processing theory, the function ω^2 in the expression $\int \omega^2 \tilde{p}(\omega)$ represents the filtering properties emphasizing higher frequencies of the relative EEG power in front of the power of lower frequencies, as visualized in Fig. 1.12. But if we admit the possibility that some frequencies could behave inconsistently to the others, it means that more possible filtering solutions could exist. And, we are getting from the basic simplified heuristic model (eq. 1.54) to the generalized spectral heuristic model (eq. 1.56) (which we have proposed within solving of the Ph.D. thesis [121]) where $g(\omega)$ characterizes the general filtering function (e.g. the α-band or γ-band[6] pass filters as shown in Fig. 1.12).

$$\tilde{b} \propto \sqrt{\int g(\omega) \tilde{p}(\omega) d\omega} \tag{1.56}$$

Implementation of the generalized spectral heuristic model (eq. 1.56), obtained results, its advances in front of classic absolute power fluctuations in distinct frequency bands, comparison with classic heuristic model and other evaluations with following discussions are described within the *chapter 3. Generalized EEG-fMRI spectral heuristic model*, and bring novel knowledges into EEG-fMRI fusion methods.

[6] γ is the label in the neuroscinece literature for the EEG signal's frequency band of interest, typically all frequencies over 20Hz.

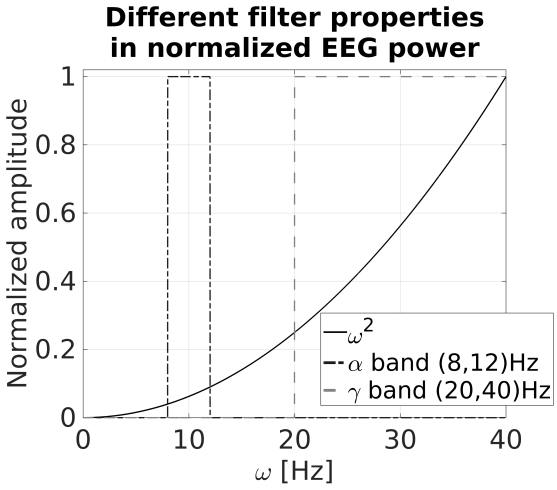

Fig. 1.12: Different filter properties for heuristic models [121].

Although the generalized spectral heuristic model allows more spectral patterns with various dynamic behaviours, it is not still utilizing the advantages of multi-channel recordings. As in case of classic absolute power fluctuations (e.g. [45, 75, 127]), the averaging over selected electrodes of interest is the most often used procedure [177, 187]. But that procedure brings very similar results over different electrode selections as evaluated and described in *chapter 3. Generalized EEG-fMRI spectral heuristic model*.

As shown before, the different EEG oscillations with different spectral properties can have different spatial sources (e.g. [94, 183]). The incorporation of the spatial information into the generalized heuristic model seems to be the other logical step and it can be written as relation 1.57 characterizing generalized spatiospectral heuristic model (which we introduced [121]).

$$\tilde{b} \propto \sqrt{\int \int g(c,\omega)\tilde{p}(c,\omega)dcd\omega} \tag{1.57}$$

Within the current thesis, the estimation of the generalized spatiospectral heuristic model was designed with incorporation of Bridwell's et al. (2013) decomposition [23] into independent EEG spatiospectral patterns. Since the decomposition is a quite novel technique whose stability and relevance has not been tested over set of different datasets yet, the submitted thesis is evaluating that properties for both decompositions (originally used absolute EEG power decomposition, and novelly used relative EEG power decomposition utilizing the spatiospectral heuristic model). Simultaneously, the relevance for the EEG-fMRI data fusion and correspondence of decomposed signals to the external stimulation timings are evaluated and assessed too. As the novel knowledges, all the procedures and obtained results are described

in the best details within the *chapter 4. EEG spatiospectral patterns for EEG-fMRI fusion.*

The all main objectives of the submitted Ph.D. thesis are summarized within the *chapter 2. Ph.D. thesis objectives.*

2 PH.D. THESIS OBJECTIVES

The process of the full automatic and well-working EEG-fMRI data fusion which is single-subject specific is still the not-solved task in the area of the basal research. The main and crucial objective of the current thesis is to try to design and find the optimal EEG-fMRI data processing pipeline which would be able to blindly estimate and visualize the task-related brain networks directly from the captured data, without any prior knowledge about the stimulus timings inside the analysis pipeline. For that final goal, the set of listed partial objectives was designed:

1. Select the EEG signal processing strategy which is usable for the blind search analysis.
2. Design the models for the data fusion which could work better than current state of the art.
3. Design the evaluation and evaluate the correspondence of obtained results with experimental external stimulation.
4. On available real simultaneous EEG-fMRI data, estimate the fusion with designed models, with previously implemented methods and compare the results over the different approaches.
5. Evaluate the designed models and their new contributions to the current knowledge.
6. Present the obtained results in neuroscience or biomedical engineering journals with impact factor as two original research papers (at minimum).
7. Share the implemented software libraries as the doctoral thesis attachment.

To the 1^{st} of the seven partial objectives, we have limited on EEG signal processing methods utilizing the EEG spectra, since a man need to know the stimulus timings for ERP estimations in the most of temporal or spatiotemporal decompositions [14, 20, 116]. It is not necessary for the EEG spectra processing or decomposition.

To the 2^{nd} of the partial objectives, we have designed the generalized spectral and spatiospectral heuristic models (eqs. 1.56 and 1.57) [121] which we are testing and comparing with previous methods within the submitted thesis.

To the rest of partial objectives, they are described and processed in more details within the following chapters: *3. Generalized EEG-fMRI spectral heuristic model*, *4. EEG spatiospectral patterns for EEG-fMRI fusion* and *5. Ph.D. thesis outcomes and conclusions*.

3 GENERALIZED EEG-FMRI SPECTRAL HEURISTIC MODEL

3.1 Introduction

As summarized within *chapters 1. Simultaneous EEG-fMRI data analysis: a brief state of the art* and *2. Ph.D. thesis objectives*, the blind visualization of task-related networks directly from the simultaneous EEG-fMRI data is still not-well known transformation. The limited number of divergent models and few results verified on limited number of experiments exist [108, 177, 181, 187]. Since relative EEG power fluctuations should characterize task-related variability better than absolute EEG power [110] and since α-band should have opposite EEG-fMRI coupling than the other bands [111], we were investigating effect of different power types in distinct frequency bands (consistent with literature [26]) on final EEG-fMRI results and we were evaluating the results' relevance to the external stimulation timings. Except that effect, we have used different selections of electrodes of interest to see the effect of that choice.

Beside EEG signal filtration on distinct frequency bands, the classic heuristic model [108, 177] was used as the other different data processing method. The similarities and differences between obtained results were quantitatively and qualitatively assessed over two datasets with different tasks (visual oddball task and semantic decision task) within the current chapter.

Simultaneously since we are comparing absolute versus relative power based results, we are testing if the transformation between absolute and relative power (eq. 1.53) is the linear or non-linear operation over time. If it would be linear the regressed EEG-fMRI SPMs would be similar, otherwise they will differ.

3.2 Materials and Methods

3.2.1 Concept of the method

The experimental fMRI and EEG data were simultaneously acquired during event-related visual oddball experiment and then jointly analyzed. To enable joint analysis between both types of data, the EEG data were converted into temporal sequences of discrete (short-time based, possibly temporally weighted) power values in each of the δ (0–4 Hz), θ (4–8 Hz), α (8–12 Hz), β (12–20 Hz) and γ (20–40 Hz) frequency bands. The temporal resolution of the sequences was given by the repetition of the fMRI scans (TR). The time series that were obtained this way were then used

as regressors in the GLM thus enabling the detection of the expected relations between the local fMRI BOLD activities in individual voxels and the EEG power series of selected combinations of lead signals in chosen frequency bands. The results, averaged over the subject group to provide group analysis, are presented as spatial maps of the found relationships individually for particular chosen parameters (e.g. selected frequency band, chosen statistical thresholding, different temporal weighting of the power series, etc.) [123]. The similar analysis was performed with classic heuristic model (eq. 1.52) [108] simplified as Rosa et al. (2010) did (eq. 1.54) [177] and the obtained results were compared with results of generalized spectral heuristic model (1.56) [121], where the generalized functions $g(\omega)$ were the above mentioned band-pass filters.

3.2.2 Visual oddball task and EEG-fMRI acquisition

A visual oddball task was performed by 22 subjects (7 women; age 23 $\pm$ 2 years; 1 left-handed man). Informed consent was obtained from all subjects after all of the procedures were fully explained, and the study received the approval of the local ethics committee. Three stimulus types were presented randomly to each subject. Each stimulus consisted of a single yellow uppercase letter shown for 500 ms on the black background. Inter-stimulus intervals varied from 4 to 6 seconds. A total of 336 stimuli consisted of targets (letter X, 15%), frequents (letter O, 70%) and distractors (letters other than X and O, 15%). Subjects were instructed to press a button held in their right hand whenever the target stimulus appeared and not to respond to distractor or frequent stimuli. The experiment was divided into four consequential sessions for each person [19, 123].

The imaging was performed by a 1.5 T *Siemens Symphony* scanner equipped with *Numaris 4 System (MRease)*. Functional images were acquired using gradient echo, echo-planar imaging sequence: TR = 1660 ms; TE = 45 ms; FOV = 250 $\times$ 250 mm; FA = 80$\circ$; matrix size = 64 $\times$ 64 (3.9 $\times$ 3.9 mm); slice thickness = 6 mm; 15 transversal slices per scan. The whole task was divided into four equal runs of 256 scans and 84 stimuli. An anatomical T1-weighted high-resolution brain scan (160 sagittal slices, resolution 256 $\times$ 256 resampled to 512 $\times$ 512, slice thickness = 1.17 mm) was added to the functional data of each subject.

The scalp EEG data, with reference electrode between Cz and Fz electrodes, were acquired simultaneously during the fMRI scanning by a 30-electrode MR compatible EEG system (*BrainProducts, Germany*) with a sampling frequency of 5 kHz [123].

3.2.3 Semantic decision task and EEG-fMRI acquisition

A semantic decision task was performed by 42 healthy subjects (22 right-handed men, 2 left-handed men, 18 right-handed women; age 25 ± 5 years). Informed consent was obtained from all subjects after all of the procedures were fully explained, and the study received the approval of the local ethics committee. The task was designed with a block stimulation paradigm which elicits robust language network activation [68]. During the probe block, sentences with semantic error created by a phonemic exchange (e.g. The cat was chased by fog) were presented randomly among semantically correct sentences. The sentences were replaced with a series of the X's or O's, (e.g. 'Xxxx xx xxxx xxx.') during the control block. Nine control and eight probe blocks alternated during the experiment. Each block lasted 24s, and consisted of six different control or probe stimuli presented for 3.5s followed by a black screen for 0.5s. Subjects viewed the stimuli through a mirror mounted on the head coil. Responses were not requested from the subjects during the task. After the session, no subjects reported any problems with reading the sentences [120, 144].

The imaging was performed by a 1.5 T *Siemens Symphony* scanner equipped with *Numaris 4 System (MRease)*. High-resolution anatomical T1-weighted MPRAGE images were acquired (160 sagittal slices, matrix size 256 x 256 resampled to 512 x 512, slice thickness = 1.17mm, TR = 1700ms, TE = 3.96ms, FOV = 246mm, FA = 15°). Parameters of fMRI acquisition using gradient echo, echo-planar imaging sequence were: 230 scans, TR = 1850ms, TE = 40ms, FA = 80°, voxel size = 3.9 x 3.9 x 6 mm 3 , no gap between slices, 20 transversal slices. The field of view covered supratentorial regions.

Simultaneously, scalp EEG data were recorded with a 30-electrode MR compatible EEG system (*BrainProducts, Germany*). ECG were recorded to remove physiological artifacts from EEG. Signals were sampled at 5 kHz with 0.5μV resolution for EEG, and 10μV for ECG [121].

3.2.4 EEG and fMRI data preprocessing

EEG preprocessing was done using *BrainVision Analyzer 2.0* (*BrainProducts, Germany*) software. The raw EEG data were corrected for the gradient artifacts [3] and down-sampled to 250 Hz. Thereafter, the IIR filter with the pass-band of 1 Hz to 40 Hz was applied. Cardiac artifacts were suppressed by mean artifact subtraction. For the visual oddball EEG data, eye-blinking artifacts were removed using decomposition by temporal ICA [40, 106] and back reconstruction without the eye-blink related component, which were chosen according to specific temporal and spatial topography.

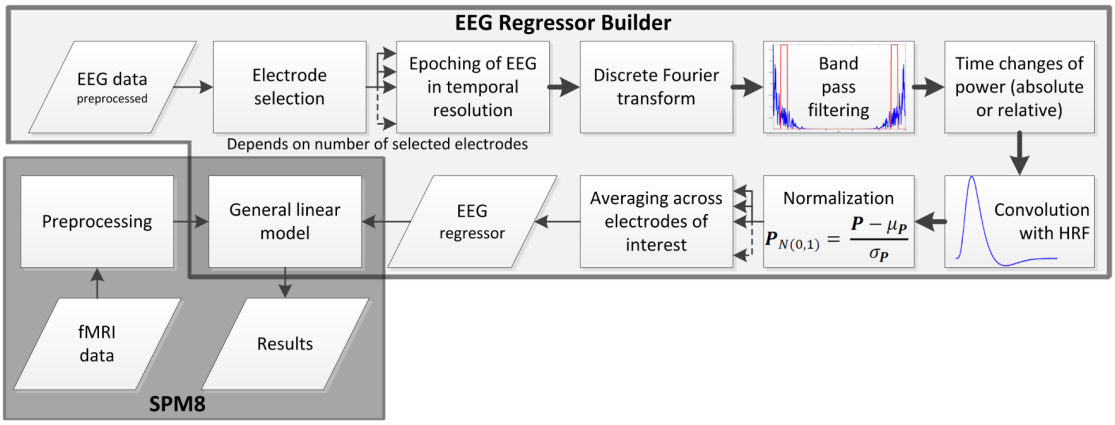

Fig. 3.1: Block diagram of the EEG Regressor Builder pipeline [123]

FMRI data were preprocessed in the SPM8 (*Statistical Parametric Mapping version 8, Wellcome Trust Centre for Neuroimaging, UK*). The first preprocessing step was motion artifact minimization, done by aligning all brain scans with registering process utilizing linear rigid geometric transformations [99]. Functional images were co-registered with the high-resolution anatomical image with linear affine geometric transformations [99]. To enable later group studies, the images were normalized to the standardized template of the head in MNI[1] coordinates with non-linear registrations [60] and re-sampled to $3 \times 3 \times 3$ mm isotropic resolution. Images were smoothed by an isotropic spatial filter with a Gaussian profile of FWHM[2] $= 8$ mm to increase the signal to noise ratio (SNR) and to make the random errors more normally distributed. Finally, the time series of each voxel was filtered to discard the component of the BOLD signal with time periods longer than 128 s which mostly contains slow drifts and physiological noise [123].

3.2.5 EEG regressor deviations for the distinct frequency bands

EEG regressors were calculated with our EEG Regressor Builder software [122]. The entire process is described below and shown in a block diagram in Fig. 3.1.

Signals measured at the electrodes of interest were selected from the pre-processed EEG data. Each of these signals was segmented onto TR long epochs with corresponding temporal resolution, where TR is the fMRI repetition time. Each EEG

[1]Montreal Neurological Institute
[2]Full Width at Half Maximum

signal epoch was transformed into the spectral domain by Discrete Fourier Transform (DFT; eq. 3.1).

$$DFT\{f_n\} = \{F_k = \sum_{n=0}^{N-1} f_n e^{-j\frac{2\pi kn}{N}}\} \tag{3.1}$$

The frequency band of interest for a given epoch (T) was filtered by zeroing spectral lines outside the band of interest. The absolute (P_a; eq. 3.2) or relative (P_r; eq. 3.3) power values were calculated from each filtered band for every epoch. The $g(k)$ is the binary vector with value 1 for k-th spectral lines belonging to the frequency band of interest. The analysed frequency range was from 0 ($k = 1$) to 40 ($k = N$) Hz divided at typical different frequency bands of interest, i.e. $\delta(0-4Hz)$, $\theta(4-8Hz)$, $\alpha(8-12Hz)$, $\beta(12-20Hz)$ and $\gamma(20-40Hz)$.

$$P_a(T) = \sum_{k=1}^{N} |g(k)F_k(T)|^2 \tag{3.2}$$

$$P_r(T) = \frac{\sum_{k=1}^{N} |g(k)F_k(T)|^2}{\sum_{k=1}^{N} |F_k(T)|^2} \tag{3.3}$$

The power values were calculated for TR-long[3] rectangular epoch windows with its temporal shift TR/2 over time. For re-sampling to the fMRI acquisition timings, the final vector of EEG power fluctuations was down-sampled with temporal weighting expressed within eq. 3.4.

$$P\left(T\right) = \frac{1}{2}P\left(T - \frac{T}{2}\right) + P\left(T\right) + \frac{1}{2}P\left(T + \frac{T}{2}\right); T \in \{0, TR, 2TR, ..., n_tTR\} \tag{3.4}$$

After temporal weighting, vectors of temporal power changes were convolved with canonic HRF to respect the similar convolution of the neural events producing the BOLD signals, as characterized with eq. 1.46. Only valid samples without convolution edge effects were used. Convolved vectors were then normalized by the equation 3.5 where $\mu_{\boldsymbol{P}}$ is mean power and $\sigma_{\boldsymbol{P}}$ standard deviation of the power vector [123].

$$\boldsymbol{P}_{N(0,1)} = \frac{\boldsymbol{P} - \mu_{\boldsymbol{P}}}{\sigma_{\boldsymbol{P}}} \tag{3.5}$$

3.2.6 Experiments with visual oddball EEG data

In order to determine the sensitivity of the regressor calculation to the task-related variability with respect to the choice of the above and below mentioned parameters,

[3]TR is the repetition time of fMRI scanning.

the EEG regressors were calculated for several types of parameter settings, and the influence on the resulting group statistical parametric EEG-fMRI maps was monitored. The studied parameters were electrodes of interest, frequency bands of interest and types of power values (absolute/relative).

The regressors were calculated for the following parameter combinations: three groups of electrodes (*O1-O2-Oz*, *C3-CP1-CP5* and *all 30 electrodes*), both types of power values (*absolute and relative*), and five frequency bands of interest δ*(0–4 Hz)*, θ*(4–8 Hz)*, α*(8–12 Hz)*, β*(12–20 Hz)* and γ*(20–40 Hz)*. Altogether 30 regressors were calculated for each subject. The selection of electrodes was substantiated as follows: *O1-O2-Oz* electrodes were chosen because primarily the visual cortices were stimulated during the experiment. *C3-CP1-CP5* electrodes are near to the motor cortices which should be activated in reaction to the target stimulus. The global signal power is defined by *all 30 electrodes* [123].

3.2.7 Joint EEG-fMRI analysis

The derived EEG regressors were compared with single-subject fMRI data within voxel-wise general linear modelling (described in the *sub-chapter 1.1 "General Linear Modelling"*) separate for each EEG regressor calculation settings. The model matrix always looked like that shown in Fig. 3.2 which contains four EEG regressors from four separate sessions and constant terms in BOLD signals for each session. To preserve task-related variability in the data, regressors describing the stimulation event were not used.

Since 30 EEG regressors were calculated for 22 subjects it means that 660 separate GLM estimations were performed with the SPM8 scripts. For each person, 30 SPMs were estimated. Because the analysis examines only their mutual influence, one SPM represents 3D correlation map between local BOLD signal and EEG regressor with a given parameter setting for corresponding subject.

During the second analytical phase, group analyses were estimated from SPMs of subjects via a one-sample t-test (similar as eq. 1.7 but over group of subjects), always using (for the whole group) a particular chosen parameter setting for EEG regressor calculation. The whole analysis output was 30 group-averaged SPMs describing above mentioned correlations.

3.2.8 Assesment of group-averaged EEG-fMRI SPMs

The purpose of the group results evaluation was firstly to determine whether and to what degree the temporal EEG power changes are reflected in the fMRI data of a

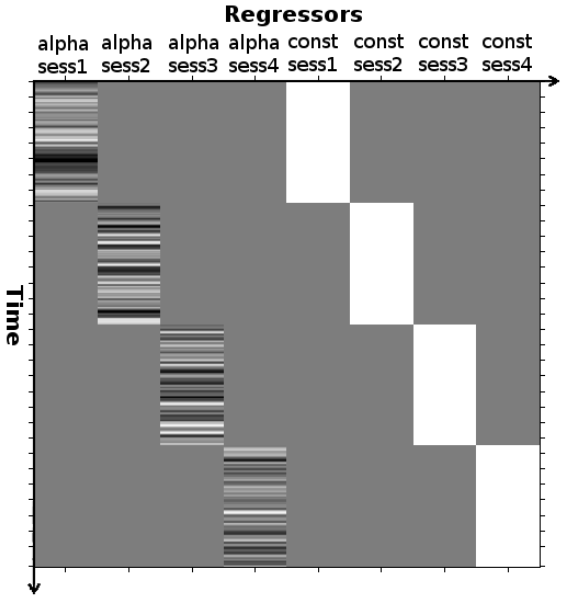

Fig. 3.2: Model matrix $\boldsymbol{X}$ in visual oddball joint EEG-fMRI analysis: It contains four EEG regressors and constant members for four separate sessions

visual oddball experiment and how the degree and localization of these correlations are related to the experiment task.

The secondary monitored effect was the effect of parameters in EEG regressor calculation on the resulting group SPMs. The results of the group analysis, in the form of the 3D maps of correlation, were assessed with visual inspection and based on not-normalized mutual information between final group SPMs with different parameter setting during EEG regressor calculations.

Different parameter analysis settings (e.g. frequency band, power value,...) can bring different or similar resulting group activation maps. The assessment of similarity of topology of group activation maps with different parameter sittings was based on joint histogram with 8-bit coding and not-normalized mutual information (MI) [99] between two different 3D activation maps. The maps were reshaped to form 1D vectors and MI was then calculated between them according to eq. 3.6 where I_{AB} is mutual information, H_A is entropy of activation map A, H_B is entropy a activation map B and H_{AB} is joint entropy of both maps [99, 123].

$$I_{AB} = H_A + H_B - H_{AB} \tag{3.6}$$

3.2.9 Assesment of task-related variability in EEG regressors

The assesment was performed with GLM (eq. 1.1) optimized with LMS algorithm (eq. 1.2). EEG regressors for different parameter settings were in matrix $\boldsymbol{Y}$ and the model signals in matrix $\boldsymbol{X}$ were the stimulus vectors with convolved canonical HRF. Group analyses across subjects were performed via one sample t-tests separately for each type of stimulation [123].

3.3 Results

3.3.1 Absolute versus relative power EEG-fMRI results

Within the current subsection, all mentioned results were obtained only from visual oddball dataset. The semantic decision dataset was not investigated for observing of the same result properties. Figure 3.3 visualize that different group SPMs are obtained with absolute and relative EEG power regressors with the same setting of other parameters (frequency band of interest, electrode selection). It indicates that relative power provides different information about brain activity than that conveyed by the absolute power [123].

Figure 3.4 shows that the relative EEG power in different frequency bands of interest correlates with the BOLD signal in different brain areas when other parameters (type of power value, electrode selection) are identical. Relative δ band and relative α band depict similar activation map with 2 differences: positively correlated clusters with BOLD signal for relative δ band are negatively correlated for relative α band and vice versa. Relative α band has higher t-values in SPMs opposite to the relative δ band [123].

Figure 3.5 illustrates the positive and negative correlations of the absolute EEG power with the BOLD signal for all five frequency bands of interest. Based on visual inspection, it seems that absolute EEG power correlates in very similar way across different frequency bands and contains some broad spectrum component which is mostly represented in α, β and γ frequency bands, less but still in δ and θ bands [123]. In comparison with figure 1.9, it seems that Laufs et al. (2003) [127] obtained very similar results for α band on resting-state dataset.

Except visual inspection, the resulting SPMs were compared with mutual information coefficients (MICs). As you can see in figure 3.6, the linear trend between different EEG-fMRI SPMs starts to be observable in mutual histograms since the MIC is higher than 0.75.

Tab. 3.1: MICs between EEG-fMRI SPMs over different power types and frequency bands: O1-O2-Oz electrodes of interest; On diagonal, there are entropies of given SPMs. Except the diagonal, values higher than 0.75 are highlighted in bold [123].

Absolute power					Relative power						
δ	θ	α	β	γ	δ	θ	α	β	γ		
4.62	**1.15**	0.48	**0.77**	0.70	0.47	0.55	0.49	0.40	0.52	δ	
	4.79	0.52	**0.85**	0.66	0.40	**0.78**	0.49	0.37	0.55	θ	
		4.68	**0.80**	0.69	0.40	0.36	0.49	0.33	0.48	α	Abs. p.
			4.67	**0.82**	0.33	0.43	0.39	0.30	0.56	β	
				4.59	0.32	0.36	0.37	0.33	0.35	γ	
					4.35	0.41	**0.99**	0.38	0.30	δ	
						4.49	0.62	0.30	0.35	θ	
							4.70	0.36	0.33	α	Rel. p.
								4.04	0.30	β	
									4.32	γ	

MICs in table 3.1 truly confirm that all three properties observed with visual inspection applies. The EEG-fMRI SPMs of different frequency bands share higher mutual information for absolute EEG power than for relative EEG power where the values are much lower. Other words, EEG-fMRI SPMs trully differs for relative power over different frequency bands (except relative δ and α bands where the similarity was observed). And finally the third property, all absolute and relative EEG-fMRI SPMs differ mutually, except absolute and relative θ bands.

Both evaluations (the visual inspection and MICs in table 3.2) confirm, that different selection of electrodes of interest does not affect and does not change the final group-averaged EEG-fMRI results.

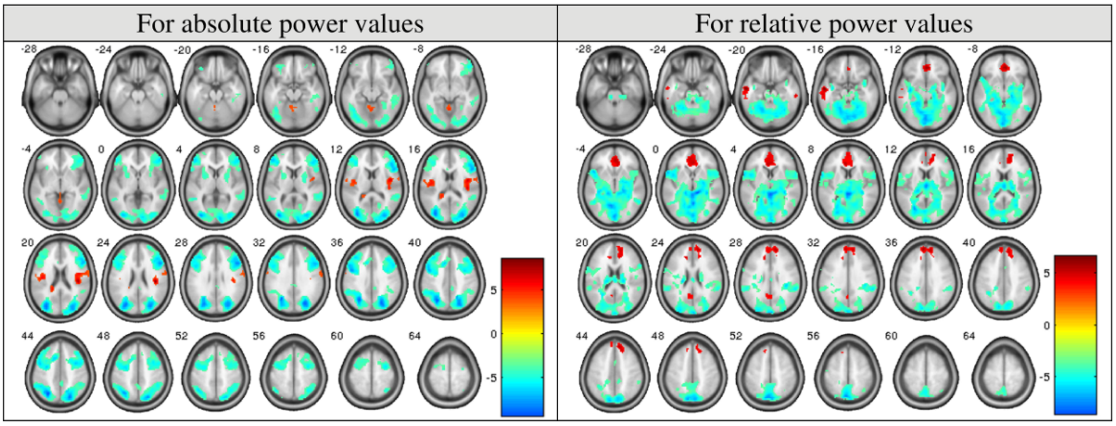

Fig. 3.3: Correlations between BOLD signal and EEG power fluctuations in α band for all 30 electrodes of interest ($p < 0.001$ uncorrected) [123].

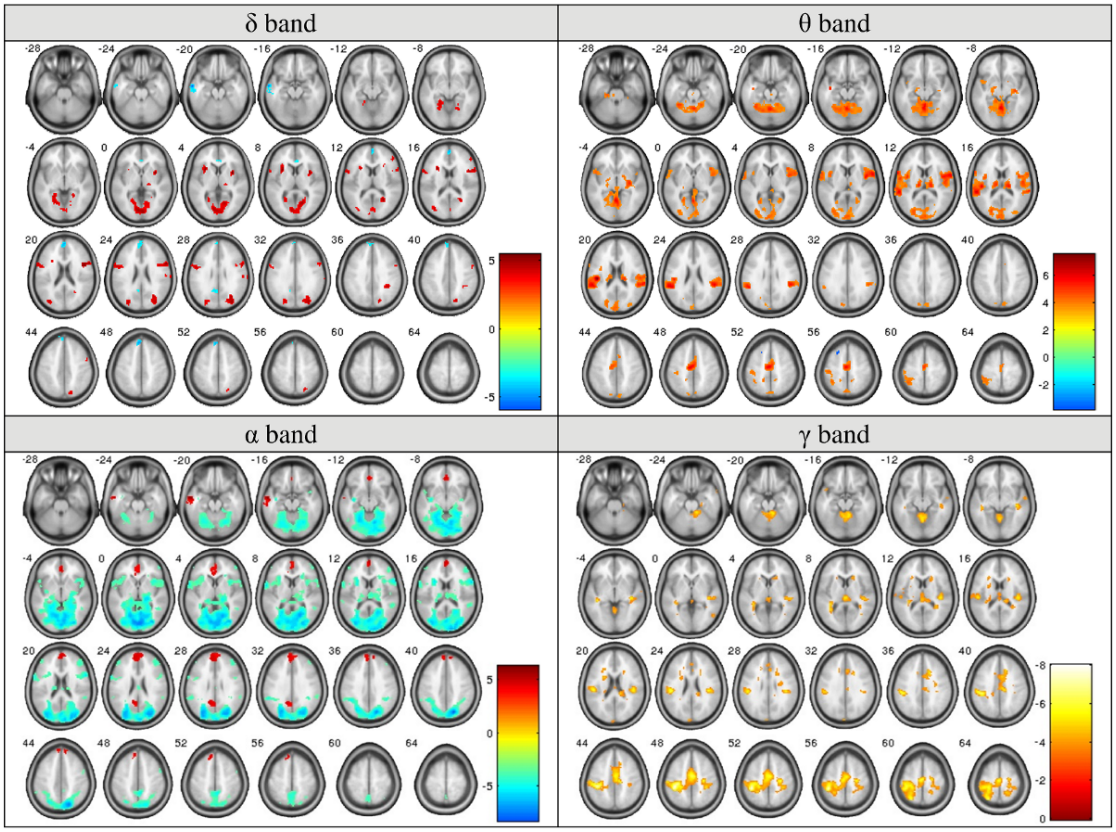

Fig. 3.4: Correlations between relative power values of EEG and BOLD signal for δ, θ, α and γ band from O1-O2-Oz electrodes ($p < 0.001$ uncorrected; for relative β band, statistically significant clusters were not observed) [123].

The GLM between EEG regressors and stimulus vectors with following group-averaging t-test indicates that relative EEG power consist more task-related variability than absolute EEG power (table 3.3). That means that heuristic approaches

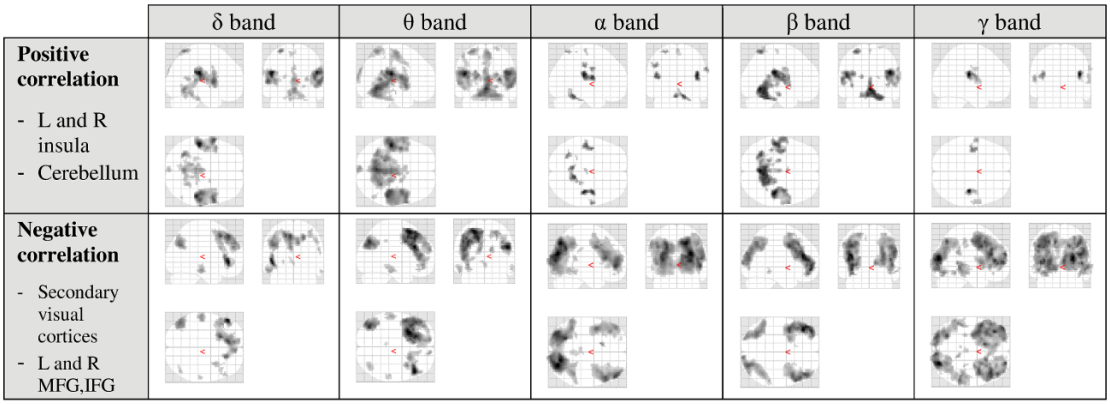

Fig. 3.5: Correlations of absolute power values with BOLD signal (O1-O2-Oz electrodes, $p < 0.001$ uncorrected) [123].

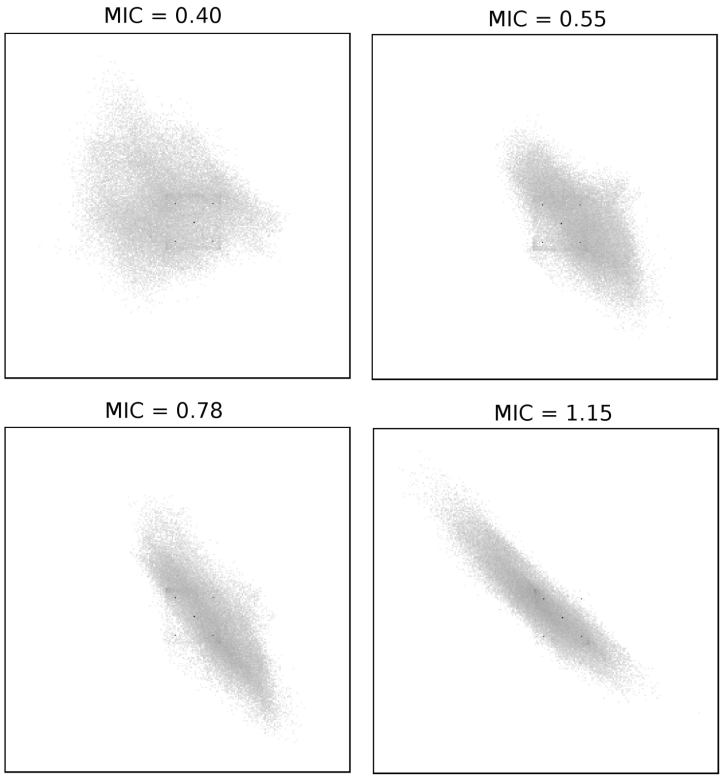

Fig. 3.6: Mutual histograms for different MICs between different group-averaged EEG-fMRI SPMs.

should be more usable for visualization of task-related networks from EEG-fMRI data than absolute EEG power fluctuations. Since classic heuristic model (eq. 1.54) [108, 177] assumes only one possible solution in relative EEG power filtration (Fig. 1.12) and since we have found heterogeneous EEG-fMRI SPMs for different fre-

Tab. 3.2: MICs between EEG-fMRI SPMs over different electrodes of interest: α band; On diagonal, there are entropies of given SPMs. Except the diagonal, values higher than 0.75 are highlighted in bold [123].

Absolute power			Relative power				
O1-O2-Oz	C3-CP1-CP5	30-electrodes	O1-O2-Oz	C3-CP1-CP5	30-electrodes		
4.68	**1.00**	**1.16**	0.49	0.38	0.40	O1-O2-Oz	
	4.59	**1.52**	0.40	0.35	0.36	C3-CP1-CP5	A.p.
		4.73	0.42	0.37	0.40	30-electrodes	
			4.70	**0.89**	**1.03**	O1-O2-Oz	
				4.62	**1.38**	C3-CP1-CP5	R.p.
					4.77	30-electrodes	

Tab. 3.3: The relationship between task-related regressors and EEG-derived regressors: The group t-values show effect of each stimulus type on EEG-derived regressors derived from all 30 electrodes. The significance level set to $p < 0.05$ uncorrected. Significant t-values are highlighted in bold [123].

Stimulus	Absolute power					Relative power				
	δ	θ	α	β	γ	δ	θ	α	β	γ
Target	**3.89**	**5.25**	1.81	**2.84**	0.76	**3.07**	**4.76**	**-5.13**	**-2.69**	**-4.79**
Frequent	1.10	0.54	0.14	0.42	-0.88	**2.09**	-0.26	**-2.12**	-0.65	**-2.69**
Distractor	1.42	1.59	-0.47	0.61	-0.42	**2.09**	1.99	**-4.01**	-0.56	**-3.02**

quency bands of relative EEG power, generalized spectral heuristic model (eq. 1.56) could be more accurate for task-related network visualizations. Results of testing this hypothesis are included within the following *sub-chapter 3.3.2 "Classic versus generalized spectral heuristic model"*.

3.3.2 Classic versus generalized spectral heuristic model

Visual inspection and MICs were used for evaluations of similarities and differences between EEG-fMRI SPMs estimated with classic heuristic model or with some frequency band of interest of relative EEG power (i.e. generalized spectral heuristic model [121]). The assessment was performed on both datasets (visual oddball and semantic decision tasks).

Figure 3.7 illustrates the EEG-fMRI SPM for classic heuristic model (eq. 1.54) on visual oddball dataset and it seems to be the most similar to the result of relative γ band (Fig. 3.4). Such observation is consistent with the fact, that both filters reach maximal gain in the same frequency range 20-40Hz (Fig. 1.12). Activated supra-thresholded sensory-motor cortices are truly contralateral to the right-handed pushed button on target stimuli [121]. That brain network can be considered as task-related based on relative γ band results (Tab. 3.3 and Fig. 3.4). Mutual information coefficients (Tab. 3.4) confirm the conlusion that the classic heuristic model result is the most similar to the relative γ band result.

Except sensory-motor network, relative δ and α band patterns demonstrate task-related visual network to be activated (Fig. 3.4 and Tab. 3.3). Classic heuristic model is insensitive to that network. Other words based on visual oddball data results, the generalized spectral heuristic model is able to visualize more task-related networks than classic heuristic model.

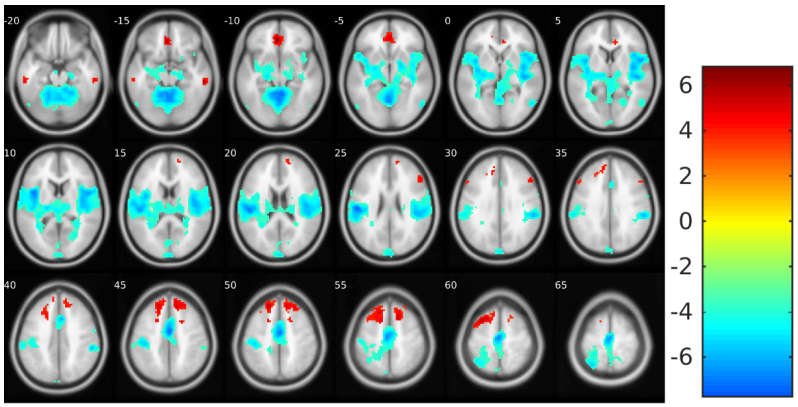

Fig. 3.7: Group EEG-fMRI SPMs for classic heuristic model from visual oddball task data ($p<0.001$ uncorrected) [121].

Tab. 3.4: MICs between EEG-fMRI SPMs over different frequency bands and classic heuristic model for visual oddball task: all 30 electrodes of interest; On diagonal, there are entropies of given SPMs. Except the diagonal, values higher than 0.75 are highlighted in bold [121].

δ	θ	α	β	γ	HM	
4.28	0.49	**1.10**	0.48	0.48	0.70	δ
	4.26	0.70	0.33	0.38	0.64	θ
		4.56	0.43	0.43	0.65	α
			3.88	0.45	0.51	β
				4.32	**0.98**	γ
					4.45	HM

In confrontation to that conclusion, visual inspection of semantic decision data results present much lower diversity in differences of EEG-fMRI results over different frequency bands (Fig. 3.8). Beside relative θ band, all other bands and heuristic model could visualize the stimulated visual network [121]. Although the diversity is lower, the matrix of MICs (Tab. 3.5) has same properties as the same matrix for visual oddball task (Tab. 3.4).

Tab. 3.5: MICs between EEG-fMRI SPMs over different frequency bands and classic heuristic model for semantic decision task: all 30 electrodes of interest; On diagonal, there are entropies of given SPMs. Except the diagonal, values higher than 0.75 are highlighted in bold [121].

δ	θ	α	β	γ	HM	
4.46	0.21	**0.89**	0.56	0.52	0.72	δ
	4.11	0.30	0.26	0.26	0.27	θ
		4.49	0.48	0.44	0.58	α
			4.24	0.49	0.65	β
				4.32	**1.29**	γ
					4.40	HM

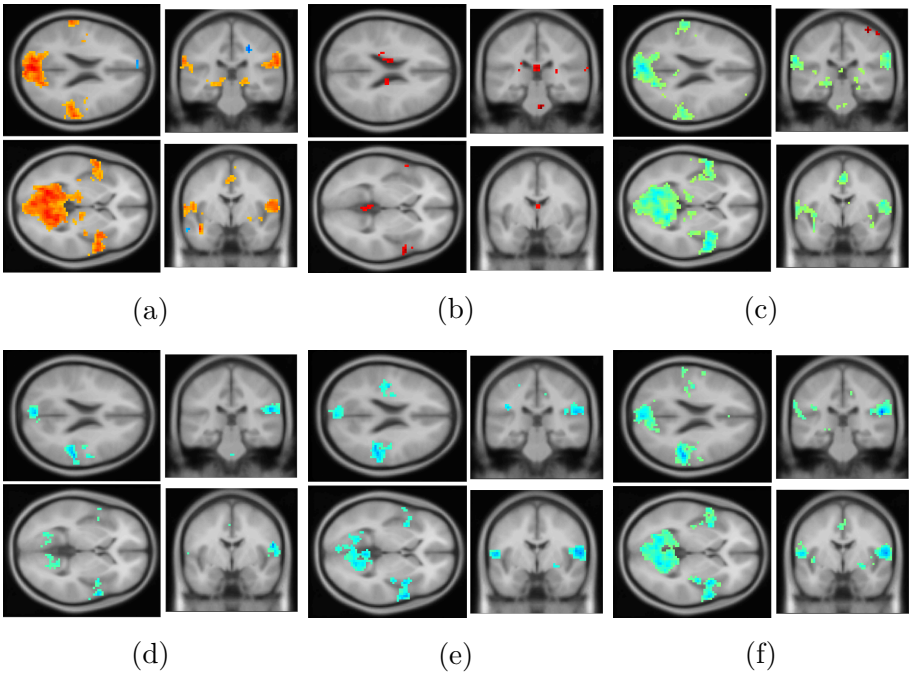

(a) (b) (c)

(d) (e) (f)

Fig. 3.8: Group-averaged EEG-fMRI SPMs for semantic decision task in slices $[-63\ -28\ 22]_{MNI}$ and $[-60\ 4\ 2]_{MNI}$ between the BOLD signal and **(a)** relative δ band; **(b)** relative θ band; **(c)** relative α band; **(d)** relative β band; **(e)** relative γ band; **(f)** classic heuristic model (p<0.001 uncorrected) [121]

3.4 Discussion

3.4.1 Visual oddball data results

Presented poor effect of the averaging over different electrode selections on final group EEG-fMRI results is consistent with previous De Munck's et al. (2009) observations [45].

Mantini et al. (2007) and De Munck et al. (2009) have already observed on resting-state datasets the broad band character of absolute EEG power correlating similarly with BOLD signal [45, 141]. Our results are extending the knowledge about the information, that the component is present whether the subjects are externally stimulated or are not. Except these studies and our results (Fig. 3.5), it is clear that Laufs et al. (2003) [127] recorded also this broad band component effect (Fig 1.9) when they regressed absolute α band power in BOLD signal, they only did not know it in that times. Except broad band negative correlations corresponding to Laufs et al. (2003) results, we are observing positive correlations between EEG absolute power and BOLD signal in insular structures which Goldman et al. (2002) [73] presented before. Positive correlations in thalamus were not found, although Goldman et al. (2002), Moosmann et al. (2003) and Gonçalves et al. (2006) presented it [73, 75, 153]. Altogether the comparison denotes that the broad spectrum character of absolute EEG power does not describe the activity associated with the experiment in the BOLD signal, but probably it shows a task-unrelated network, which is alluded in both resting-state and oddball studies [141, 142], and which is active in the waking state whether the subject's eyes are open or closed [123].

Physiological interpretation of relative EEG power correlations can be divided into three groups [123]:

1. primary stimulated primary and secondary visual cortices observed for α band pattern and partly also for δ band (Fig. 3.4)
2. lateralized secondary stimulated sensory-motor and motor cortices observed for γ band pattern (Fig. 3.4) and classic heuristic model (Fig. 3.7)
3. deep centers of the brain observed for α band pattern (Fig. 3.4)

3.4.2 Semantic decision data results

Although we are observing similar properties of the relative power results over both examined datasets (Tabs. 3.4 and 3.5), semantic decision dataset results are quite speculative. The result diversity over different frequency bands is lower than for visual oddball data. And, we did not find activations in stimulated speech cortices (Broca's and Wernicke's areas), found to be positively correlated with fMRI analysis

without EEG on same dataset [121] and be correlated with EEG spectra decomposed with Parallel Factor Analysis (PARAFAC) on the same dataset [144].

Since the most of activation is observed in visual network and since the eye-blinking artifact (with expected broad band character) was not filtered out from the semantic decision EEG data, it is possible that current EEG-fMRI results were distorted by that artifact. Although the actual results are possibly distorted, the keeping the eye-blinking artifact within one EEG dataset had its justification, as you will read in following *chapter 4 "EEG spatiospectral patterns for EEG-fMRI fusion"*, where we have tested if spatiospectral group-ICA is able to isolate the eye-blinking artifact into one separate component and filter it out from physiological EEG sources (e.g. PARAFAC decomposition of EEG spectra was able to do it [144]).

To repair actual state in actual analysis, my bachelor student Lukáš Dobiš is working on his bachelor thesis *"Effect of eye-blinking artifact on results of simultaneous EEG-fMRI data fusion"* under my supervision in the current academic year. So, next year new actualized and improved results can be expected.

3.4.3 Classic or generalized spectral heuristic model?

The classic heuristic model (eq. 1.54) seems to be sensitive to the very similar EEG signal properties as relative γ band pattern (Tabs. 3.4 and 3.5) and insensitive to the properties characterized by relative α band pattern in visual oddball data (Figs. 3.4 and 3.7). Since the results of relative α band pattern are potentially also task-related (Tab. 3.3), it can be expected that generalized spectral heuristic model (eq. 1.56) [121] can visualize more physiological task-related networks than classic heuristic model [108, 177]. Evaluations and assessments based on semantic decision data would be more possible and relevant, when the EEG-fMRI results will be known from the data with removed eye-blinking artifact.

Approximately in the same time, when we were performing experiments and published some of results described within the current chapter, Sclocco et al. (2014) [187] presented full spectral heuristic model (eq. 3.7).

$$\tilde{b} \propto \sqrt{\int \omega^2 g(\omega) \tilde{p}(\omega) d\omega} \tag{3.7}$$

The equation expect both filtering functions (Fig. 1.12), i.e. the fixed frequency in square ω^2 as in eq. 1.54 and variable filtering function $g(\omega)$ as in eq. 1.56. The comparison of our results with this more generalized model should be done in the future.

3.4.4 Current study limits and possible future work

One of important limitations of the current study is that all validations of task-related variability were more targeted on spatial pattern similarity of EEG-fMRI GLM and the temporal coherence of signals was not considered [123].

Another limitation is that fixed canonical HRF was used across whole EEG frequency range. In recent years, it has been showed with different analysis methods that although the amplitude time delay is consistent, the impulse response function (IRF) between EEG and BOLD signal differs with respect to frequency band of interest [23, 46]. In the future work, it might be more beneficial to calculate with different IRFs or to deconvolve IRFs between task-related regressors and BOLD signal [123].

As it was shown here and also in previous publication [45], the averaging over electrode selection has not probably crucial effect on group SPM results. It seems that EEG signal decomposition on independent components as in [23, 94, 184] could be more beneficial for signal processing during the following analyses [123]. How to utilize the spatiospectral heuristics (eq. 1.57) [121] into the EEG-fMRI analysis will be described and presented within the following chapter *chapter 4 "EEG spatiospectral patterns for EEG-fMRI fusion"*.

Within the future research, the generalized spectral heuristic model (eq. 1.56) should be compared with Sclocco's et al.(2014) full spectral heuristic model (eq. 3.7). This missing comparison definitely limits current thesis.

All presented results and conlusions should be once more revalidated on semantic decision dataset, when the eye-blinking artifact will be suppressed in raw EEG data.

3.5 Conclusion

The conclusions are predominantly declared based on visuall oddball data results, since the semantic decision data results were possibly damaged by the eye-blinking artifact.

The visual oddball data results show that the absolute and relative EEG powers are indicators of different brain processes, and that they are associated differently with fMRI data. From that point of view transformation between absolute and relative EEG power fluctuations can be considered as non-linear operation. While the absolute power showed dominantly a broad spectrum component in task-unrelated networks, the relative power showed activity in the visual, sensory-motor, and motor networks. Simultaneously it has been showed that relative power describes the task-related activity better than absolute power and that it is able to suppress the

broad spectrum component. From this point of view, it has been shown that relative EEG power appears to be a better indicator of task-related activations for joint EEG-fMRI analysis [123].

Matrices of mutual informations between EEG-fMRI SPMs of different heuristic models has similar structure over both tested datasets. Classic heuristic model visualized similar EEG-fMRI SPMs which are observed with generalized spectral heuristic model for γ frequency band. More on visual oddball data, the generalized spectral heuristic model demonstrated task-related visual network for α band pattern, which were not observable with the classic heuristic model. From that point of view, generalized spectral heuristic model was able to see more task-related networks and should be preferred because of that before the classic model, since the γ band pattern is able to see similar activations as the classic model.

The current analyses and experiments brought two main novelties into the current state of the art. Relative EEG power could be more usable in task-related networks visualizations from simultaneous EEG-fMRI data. And, generalized spectral heuristic model could visualize more task-related networks than the classic model.

4 EEG SPATIOSPECTRAL PATTERNS FOR EEG-FMRI FUSION

4.1 Introduction

As it results from previous *chapter 3 "Generalized EEG-fMRI spectral heuristic model"*, the averaging over different electrodes of interest does not change significantly the final group-averaged EEG-fMRI results. To utilize the spatial information from EEG better, we have started to work with novel blind source separation technique (BSS) called spatiospectral group-ICA (eq. 1.51) presented by Wu et al. (2010) and Bridwell et al. (2013) [23, 215]. Since different ICA algorithms with following group classifications of patterns present success rate of stable patterns lower than 40% [91, 93], we have first examined the stability of the group EEG spatiospectral estimates over three different simultaneous EEG-fMRI datasets which we had available (visual oddball, semantic decision and resting-state paradigms).

Since we have got much higher stabilities than previously obtained classifiers, the fusion of stable independent EEG spatiospectral pattern fluctuations with BOLD signal was the following step and is in scope of the following text.

Except the stability of spatiospectral estimates and their fusion with fMRI data, we were observing and testing, whether spatiospectral group-ICA of EEG signal is able to isolate eye-blinking artifact into a separate component and filter it out from the signal. Similarly as in previous chapter, we are testing the relationships between spatiospectral pattern fluctuations and external stimulus vectors, if they were present during the experiment.

4.2 Materials and Methods

4.2.1 Concept of the method

Three experimental fMRI and EEG datasets were simultaneously acquired during event-related visual oddball, block-designed semantic decision and resting-state experiments and then analysed. Spatiospectral group-ICA belonging to BSS algorithms was used for the isolation of distinct EEG oscillations separately for each EEG dataset. Single-subject spatiospectral patterns were obtained with following back-reconstruction from aggregated group averages. All single-subject spatiospectral patterns from all three experiments were clustered using K-means clustering algorithm and stable EEG spatiospectral patterns were looking for. The stability was tested for both powers (absolute and relative). The block diagram of the whole

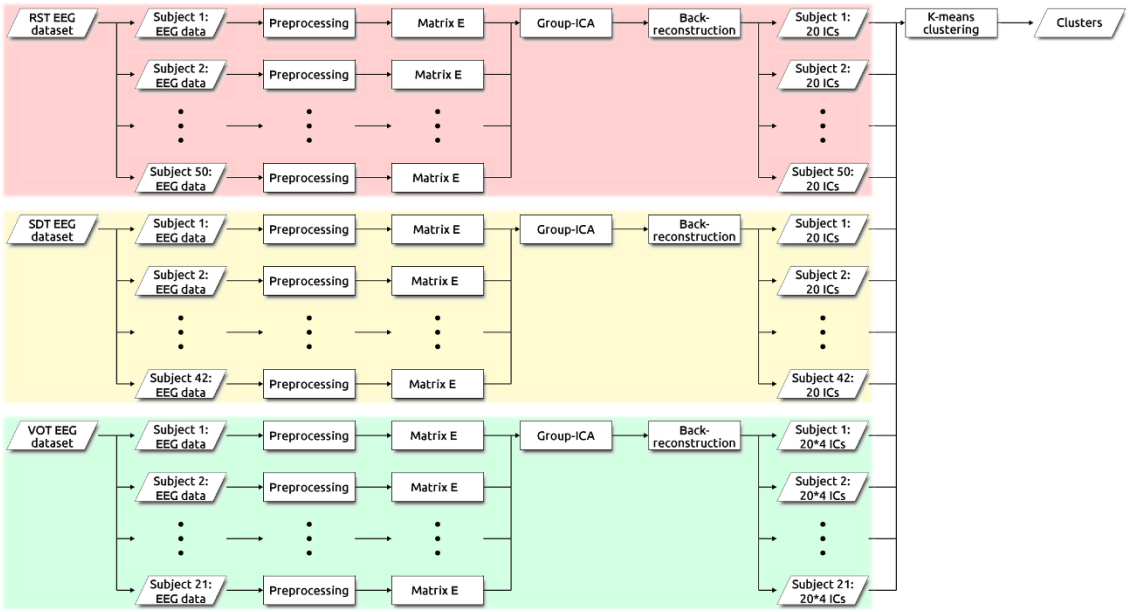

Fig. 4.1: Block diagram of the EEG spatiospectral pattern clustering pipeline: from resting-state (RST), sematic decision (SDT) and visual oddball (VOT) EEG datasets [120]

EEG data processing pipeline is shown in Fig. 4.1, where the matrix $\boldsymbol{E}$ is the single-subject matrix $\boldsymbol{D}$ in eq. 1.51 (i.e. before the two-stage PCA, where matrix $\boldsymbol{D}$ is derived).

For the stable spatiospectral patterns, the relationships between their time-courses (columns in single-subject matrices $\boldsymbol{A}$ back reconstructed from matrix $\hat{\boldsymbol{A}}$ in eq. 1.51) and stimulus vectors were examined with similar GLM and following group one-sample t-test as in previous chapter for absolute/relative power fluctuations averaged over electrodes of interest.

And, the time-courses of the stable patterns were fused with fMRI-BOLD signals via GLMs where variable hemodynamic response functions were modelled to overcome some limitations rising from the *sub-chapter 3.4.4 "Current study limits and possible future work"*. The group-averaged EEG-fMRI SPMs were then estimated within an one-way ANOVA test.

4.2.2 Visual oddball and semantic decision datasets

Same EEG-fMRI datasets with same acquisition parameters was used as described within previous *subchapters 3.2.2 "Visual oddball task and EEG-fMRI acquisition"* and *3.2.3 "Semantic decision task and EEG-fMRI acquisition"*

4.2.3 Resting-state paradigm and EEG-fMRI acquisition

Fifty healthy subjects participated in a 15 min "resting-state" experiment (30 right handed men, 20 right-handed women; age 25 ± 5 years). Subjects were instructed to lie still within the fMRI scanner with their eyes closed, not to think of anything specific, and not to fall asleep.

The imaging was performed by a 1.5 T *Siemens Symphony* scanner equipped with *Numaris 4 System (MRease)*. High-resolution anatomical T1-weighted MPRAGE images were acquired (160 sagittal slices, matrix size 256 x 256 resampled to 512 x 512, slice thickness = 1.17mm, TR = 1700ms, TE = 3.96ms, FOV = 246mm, FA = 15°).

Functional images were acquired using gradient echo, echo-planar imaging sequence: TR = 3000 ms; TE = 40 ms; FOV = 220 × 220 mm; FA = 90°; matrix size 64 × 64 (3.9 × 3.9 mm); slice thickness = 3.5 mm; and 32 transversal slices which covered the whole brain excluding part of the cerebellum. 300 functional scans were acquired in 1 continuous session.

Simultaneously, scalp EEG data were recorded with a 30-electrode MR compatible EEG system (*BrainProducts, Germany*). ECG were recorded to remove physiological artifacts from EEG. Signals were sampled at 5 kHz with 0.5μV resolution for EEG, and 10μV for ECG.

4.2.4 Equipment and participants over paradigms

The equipment was identical during acquisitions of the three paradigms described below, and the subjects within two paradigms partially overlapped (among the 50 and 42 individuals who participated in the resting state and semantic decision paradigms, respectively, 29 subjects participated in both). The visual oddball participants were a separate group of subjects than the other two tasks [120].

4.2.5 EEG and fMRI data preprocessing

The preprocessing steps were the same as in previous *sub-chapter 3.2.4 "EEG and fMRI data preprocessing"*. The eye-blinking artifact was not removed from resting-state EEG dataset, since the subjects had closed eyes.

4.2.6 EEG spatiospectral decomposition

For each session, the preprocessed EEG signal from each lead was normalized such that the time course was normally distributed $N(0, 1)$, and divided into 1.66 s (the shortest repetition time of fMRI scanning TR) epochs without overlap. Each epoch

was transformed to the spectral domain with fast Fourier transform (FFT), generating a vector (length = 67) of complex valued spectral coefficients between 0-40Hz. Complex values were converted to absolute/relative power. The output vector of 67 real absolute/relative power values comprised a 3D matrix $\boldsymbol{E}$ with dimensions n_T, n_c and n_ω. Dimension n_T is the total number of EEG epochs ($n_T = 540$ for RST; $n_T = 255$ for SDT; $n_T = 256$ for VOT), dimension n_c is the total number of leads ($n_c = 30$) and dimension n_ω is the total number of spectral coefficients ($n_\omega = 67$). The 3D matrix $\boldsymbol{E}(n_T, n_c, n_\omega)$ was transformed into a 2D matrix $\boldsymbol{E}(n_T, n_c * n_\omega)$. Matrix $\boldsymbol{D}$ is estimated with two-stage PCA (for more details see *sub-chapter 1.2.3 "Data dimensionality reduction with two-stage PCA"*) from $\boldsymbol{E}$ matrices of all subjects and used as input into group spatiospectral ICA decomposition (eq. 1.51) [23], returning a group aggregated mixing matrix $\hat{\boldsymbol{A}}$ with dimensions $\hat{\boldsymbol{A}}(n_T, m)$ and a group aggregated source matrix $\hat{\boldsymbol{S}}$ with dimensions $\hat{\boldsymbol{S}}(m, n_c * n_\omega)$. The dimension m is the number of set and decomposed independent components [120].

The first stage PCA reduced dimensionality of single-subject matrices $\boldsymbol{E}$ at 50 dimensions from original 540 dimensions for RST, 255 for SDT and 256 for VOT. The second stage PCA reduced the group variability at 20 principal components. Group spatiospectral ICA was conducted separately for each paradigm and power type, and the data were decomposed to $m = 20$ independent spatiospectral components. The PCA data reduction and whole group ICA decomposition were performed using the GIFT toolbox [29] with the INFOMAX optimizing algorithm [12, 21] (for more details see *sub-chapter 1.2.1 "ICA cost functions and optimizing algorithms"*). The reproducibility of group components was examined using 10 ICASSO itterations when the cluster quality index (I_q; eq. 1.45) evaluated the cluster's stability [79, 80] (for more details see *sub-chapter 1.2.5 "Model order and stability of ICA"*).

The analysis outputs are group-derived aggregated matrices $\hat{\boldsymbol{A}}$ and $\hat{\boldsymbol{S}}$ for each paradigm and separate $\boldsymbol{A}$ and $\boldsymbol{S}$ matrices generated by back reconstruction against each individual subject's data (for more details see *sub-chapters 1.2.2 "ICA multi-subject extension" and 1.2.4 "Back-reconstruction to single subject estimates"*). The spatiospectral matrices $\boldsymbol{S}$ were collected across subjects and paradigms for clustering (separately for each power type), as described below. The relationship between spatiospectral components/sources and task dynamics were examined by relating the source time course (i.e. mixing matrix) $\boldsymbol{A}$ with the respective stimulus time course [120].

4.2.7 Clustering of spatiospectral maps across paradigms

For each subject, paradigm and session (4 sessions for VOT data), we have one matrix $\boldsymbol{S}$ with dimensions $\boldsymbol{S}(20, 2010)$ containing 20 back-reconstructed spatiospec-

tral patterns. For similarity/dissimilarity assessment of the spatiospectral patterns across paradigms, we have performed k-means clustering, a conventional algorithm belonging to multivariate methods for dimensionality reduction. Because we had 50 single-subject $\boldsymbol{S}$ matrices for "rest", 42 single-subject $\boldsymbol{S}$ matrices for semantic decision task and $21 \times 4 = 84$ single-subject $\boldsymbol{S}$ matrices for visual oddball task, there are $(50+42+84)*20 = 3520$ different spatiospectral patterns comprising matrix $\boldsymbol{C}$, with dimensions $\boldsymbol{C}(3520, 2010)$ as input for k-means clustering. K-means clustering was performed with Pascual-Marqui et al. (1995) optimizing method [166] with set 40 final clusters. Clustering was repeated 50 times with random initial conditions and the result with minimal residuals was selected as the final clustering result [120].

After clustering, a few post-processing steps were necessary in some cases: IF a given cluster consists of spatiospectral patterns from subjects from RST, subjects from SDT and subjects from VOT; AND IF another cluster contains the same spatiospectral pattern with subjects from the three paradigms then those 2 clusters are combined and considered as one final cluster [120].

4.2.8 Assessment of intra- and inter-cluster correlations

The correlation was computed between single-subject, single-session and single-paradigm spatiospectral patterns within the k-means cluster (intra-cluster correlations) and between patterns of different clusters (inter-cluster correlations). These correlations were averaged separately within and across clusters to assess the similarity of patterns within clusters compared to across clusters. The mean coefficients (r) were transformed at t-values (Eq. 4.1), and then respectively at p-values (Eq. 4.2) of statistical significance characterizing the probability if intra- or inter-cluster components are similar or not (number of samples $n = 2010$). The function C in Eq. 4.2 is the cumulative density function for t-distribution depending on |t|-value and on the difference between number of samples n and degrees of freedom (=1).

$$t = \frac{r}{\sqrt{\frac{1-r^2}{n-2}}} \tag{4.1}$$

$$p = 2(1 - C(|t|, n-1)) \tag{4.2}$$

4.2.9 Spatiospectral pattern dynamics and stimuli vectors

For each subject, paradigm and session, we have got one matrix $\boldsymbol{A}$ with dimensions $\boldsymbol{A}(n_T, 20)$ containing the back-reconstructed time course of each spatiospectral component. Relationships between these dynamics and stimulus vector timings (in matrix $\boldsymbol{X}$) were assessed with a single-subject general linear model (eq. 4.3) solved

with the least mean square algorithm (eq. 1.2) and a continuous group one-sample t-test for the each stimulus vector as implemented previously [62, 123, 120].

$$\boldsymbol{A} = \boldsymbol{X}\boldsymbol{\beta} + \boldsymbol{\epsilon} \tag{4.3}$$

4.2.10 Topologies and average spectral densities of stable spatiospectral patterns

The topology $\boldsymbol{v}_z$ of each group-averaged *z-th* spatiospectral pattern was estimated with eq. 4.4 as the sum of spatiospectral pattern $\boldsymbol{S}_z$ over frequencies, normalized to a mean of 0 and standard deviation of 1 with eq. 4.5, where $\overline{v_z}$ is the mean value and $\sigma_{\boldsymbol{v}_z}$ is variance of the unnormalized vector $\boldsymbol{v}_z$. The average spectral density $\overline{q_z(\omega)}$ of each *z-th* group averaged spatiospectral pattern was calculated with eq. 4.6 as the averaged sum of *z-th* spatiospectral pattern $\boldsymbol{S}_z$ over channels c. Its confidence interval was computed over channels with equations 4.7 and 4.8, where $\overline{\sigma_{q_z}(\omega)}$ is the variance of the spectral density for each frequency ω.

$$v_z(c) = \sum_{n=1}^{n_\omega} S_m(c, n) \tag{4.4}$$

$$\boldsymbol{v}_{z_{N(0,1)}} = \frac{\boldsymbol{v}_z - \overline{v_z}}{\sigma_{\boldsymbol{v}_z}} \tag{4.5}$$

$$\overline{q_z(\omega)} = \frac{1}{n_c} \sum_{k=1}^{n_c} S_z(k, \omega) \tag{4.6}$$

$$\overline{\sigma_{q_z}(\omega)} = \frac{1}{n_c - 1} \sum_{k=1}^{n_c} (S_m(k, \omega) - \overline{q_z(\omega)}) \tag{4.7}$$

$$\boldsymbol{q}_z \in \langle \overline{\boldsymbol{q}_z} - 2\sqrt{\overline{\boldsymbol{\sigma}_{\boldsymbol{q}_z}}}; \overline{\boldsymbol{q}_z} + 2\sqrt{\overline{\boldsymbol{\sigma}_{\boldsymbol{q}_z}}} \rangle \tag{4.8}$$

4.2.11 EEG-fMRI GLM with variable HRFs

Relationships between fMRI voxel time courses and spatiospectral map time courses (columns in individual $\boldsymbol{A}$ matrices) were examined using the GLM (eq. 1.1) [62] with the individual time course convolved with the canonical HRF (regressor 1), convolved with the 1^{st} temporal derivative of the HRF (regressor 2) or convolved with the 2^{nd} temporal derivative of the HRF (regressor 3) as in [144]. Using the canonical HRF and 1^{st} and 2^{nd} temporal derivatives helps account for variability in the IRF's shape across subjects, tasks, and voxels.

Separate GLMs were performed for each stable spatiospectral pattern, paradigm and subject. In addition to the three EEG regressors, the model matrix $\boldsymbol{X}$ contained

a DC component. Regression matrices $\boldsymbol{\beta}$ were estimated over all GLMs with the ReML algorithm (Restricted Maximum Likelihood) implemented in SPM12 software (*Wellcome Trust Centre for Neuroimaging, London, UK*) in the MATLAB programming environment (*MathWorks, Natick, USA*).

Group-averaged EEG-fMRI results were estimated with a one-way ANOVA test (implemented in SPM12) of 3 EEG-derived single-subject spatial $\boldsymbol{\beta}$-maps for each of 3 EEG regressors. The $\boldsymbol{\beta}$ weights served as dependent variables in separate ANOVA tests conducted for each paradigm and spatiospectral pattern, generating group-averaged spatial EEG-fMRI F-maps. The final F-maps were thresholded at $p < 0.001$ uncorrected for multiple testing errors (i.e. with a critical absolute F-value of 5.71), and the criteria that clusters contain 100 voxels or more.

4.2.12 Estimation of group-averaged EEG-fMRI IRFs

For each supra-threshold voxel i, the local EEG-fMRI IRF $\boldsymbol{h}_i$ was estimated with equation 4.9, where $\beta_{i,1}$ is the group-averaged regression coefficient of the 1^{st} EEG regressor (convolved with the canonical HRF $\boldsymbol{\rho}$), $\beta_{i,2}$ is the group-averaged regression coefficient of the 2^{nd} EEG regressor (convolved with 1^{st} temporal (t) derivation of canonical HRF), and $\beta_{i,3}$ is the group-averaged regression coefficient of the 3^{rd} EEG regressor (convolved with 2^{nd} temporal derivation of canonical HRF) as expected in [61]. The distributions of estimated HRFs were examined across supra-threshold voxels, separately for each spatiospectral pattern, and paradigm.

$$\boldsymbol{h}_i = \beta_{i,1}\boldsymbol{\rho} + \beta_{i,2}\frac{d\boldsymbol{\rho}}{dt} + \beta_{i,3}\frac{d^2\boldsymbol{\rho}}{dt^2} \tag{4.9}$$

4.3 Results

4.3.1 EEG spatiospectral decomposition

The percent of variance explained in absolute EEG power after dimensionality reduction through the 1^{st}-stage PCA is demonstrated in Fig. 4.2a for the RST dataset, in Fig. 4.2b for the SDT dataset and in Fig. 4.2c for the VOT dataset. In all three cases, the first 50 principal components explain about 95% of variability [120]. For the relative EEG power, the same results are visualized in Fig. 4.2d for the RST dataset, in Fig. 4.2e for the SDT dataset and in Fig. 4.2f for the VOT dataset. The explained variability by the first 50 PCs is about 5% lower than for the previous absolute power.

The 20 independent group EEG spatiospectral components, and their reproducibility over 10 ICASSO estimates are shown for absolute power in Fig. 4.3 for

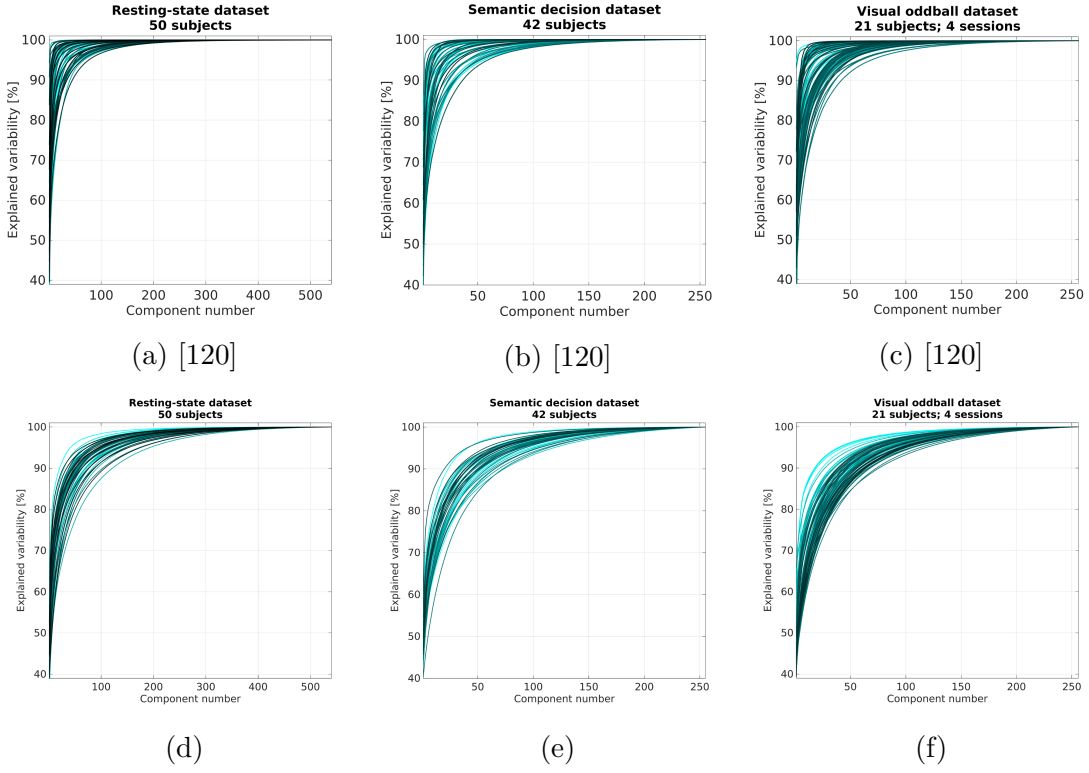

(a) [120] (b) [120] (c) [120]

(d) (e) (f)

Fig. 4.2: EEG data dimensionality after 1^{st}-stage PCA decomposition: (**a-c** results for the absolute power; (**d-f**) results for the relative power

RST data, Fig. 4.4 for SDT data and Fig. 4.5 for VOT data. The most reproducible component estimates were achieved for the resting-state paradigm (Fig. 4.3b,c) where all cluster quality values were above 0.9. The last 3 or 4 cluster quality indexes of the least reliable components were between 0.7 and 0.9 for semantic decision (Fig. 4.4b,c) and visual oddball (Fig. 4.5b,c) data. Same results for relative power are shown in Fig. 4.6 for RST data, Fig. 4.7 for SDT data and Fig. 4.8 for VOT data. Relative EEG power results have lower cluster stability over ICASSO runs, since the cluster quality indices (I_q) are lower (Figs. 4.6b, 4.7b and 4.8b) than for absolute EEG power (Figs. 4.3b, 4.4b and 4.5b), and CCA projections are also less compact (Figs. 4.6c, 4.7c and 4.8c) than for the absolute power (Figs. 4.3c, 4.4c and 4.5c) [120].

Visual inspection among the spatiospectral maps generated across paradigms (Figs. 4.3a, 4.4a and 4.5a) suggests that similar components may be observed across all three datasets (e.g. for absolute power: RST com. n. 10, SDT com. n. 14 and VOT com. n. 17; or RST com. n. 19, SDT com. n. 13 and VOT com. n. 13; or RST com. n. 16, SDT com. n. 15 and VOT com. n. 15; etc.) [120]. Similar visual observations you may find also among the relative EEG power components (Figs. 4.6a, 4.7a and 4.8a).

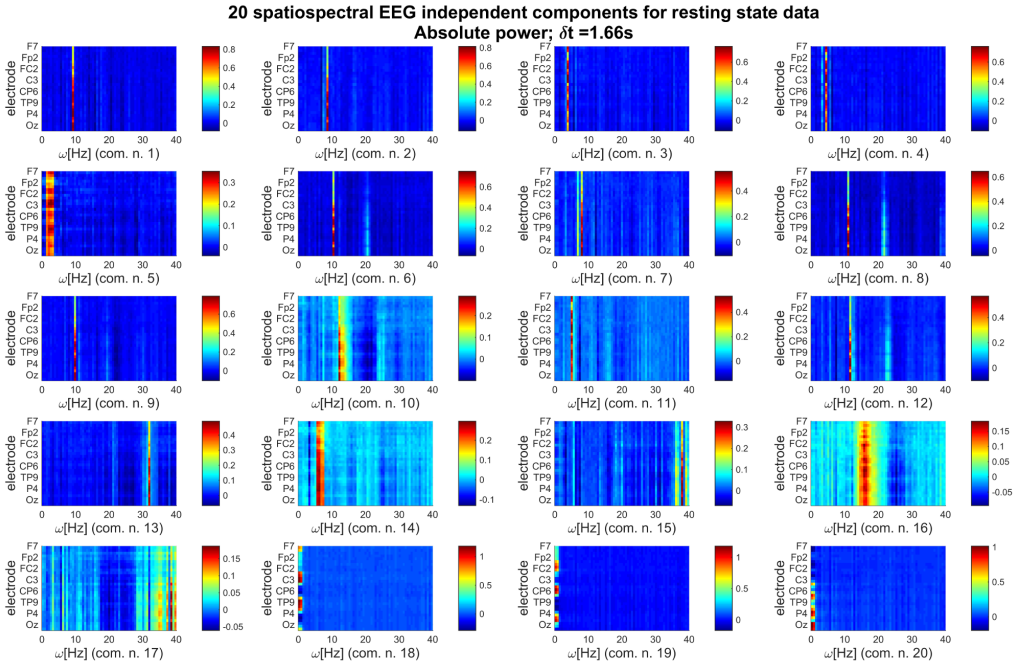

(a)

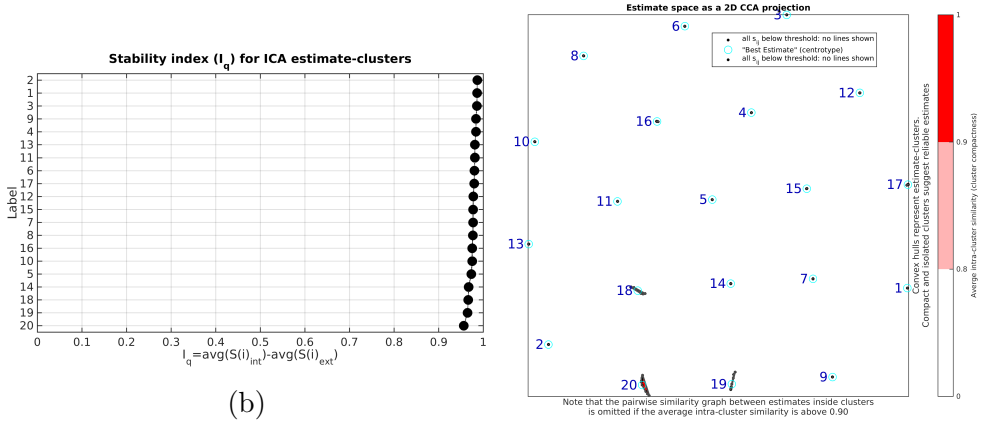

(b)

(c)

Fig. 4.3: Absolute EEG power group-averaged independent EEG spatiospectral pattern results for resting-state paradigm: (**a**) 20 independent spatiospectral patterns; Spatial distribution of electrodes in matrices is: F7, F3, Fp1, Fz, Fp2, F4, F8, FC6, FC2, FC1, FC5, T7, C3, Cz, C4, T8, CP6, CP2, CP1, CP5, TP9, P7, P3, Pz, P4, P8, TP10, O2, Oz, O1. (**b**) Cluster quality indexes I_q [80, 136] are indicated in rank order for each of the 20 components (y-axis). (**c**) Components were projected into 2D space using curvilinear component analysis (CCA). Clusters are enclosed by red convex hulls and grey lines connect similar components. Each of the 20 clusters represent each of the 20 components (labeled within the plot) [120].

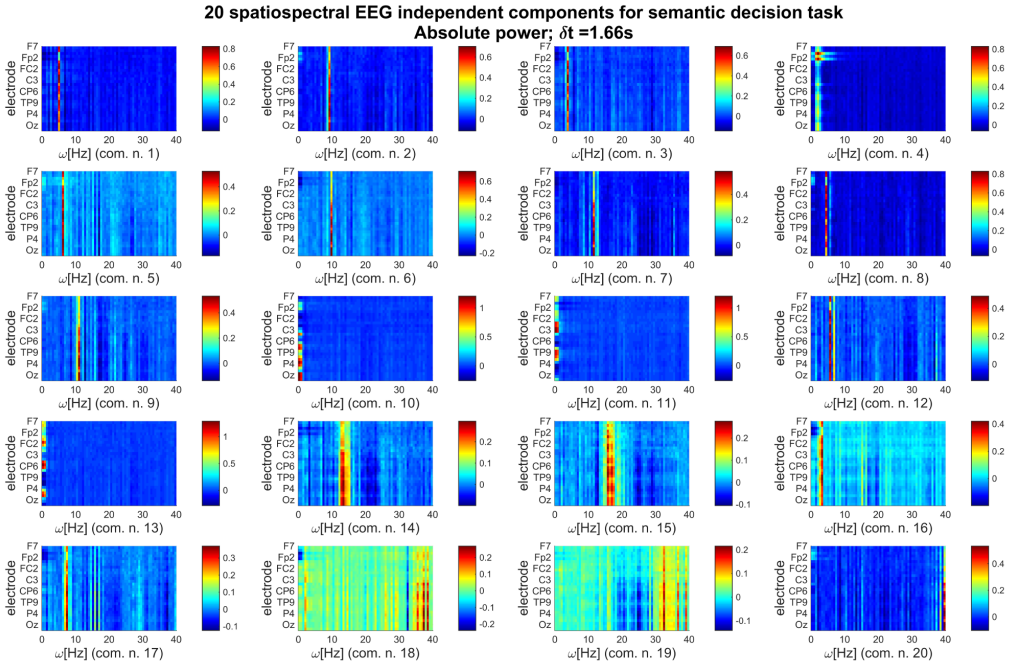

(a)

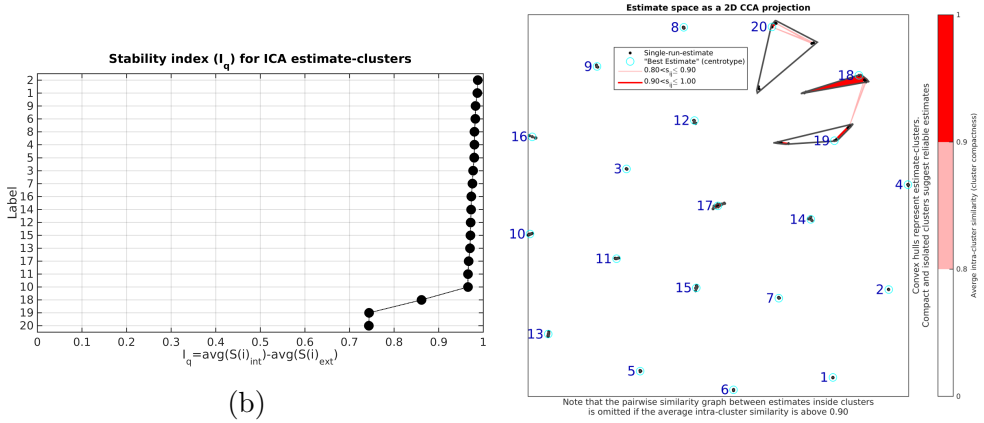

(b)

(c)

Fig. 4.4: Absolute EEG power group-averaged independent EEG spatiospectral pattern results for semantic decision paradigm: (**a**) 20 independent spatiospectral patterns; Spatial distribution of electrodes in matrices is: F7, F3, Fp1, Fz, Fp2, F4, F8, FC6, FC2, FC1, FC5, T7, C3, Cz, C4, T8, CP6, CP2, CP1, CP5, TP9, P7, P3, Pz, P4, P8, TP10, O2, Oz, O1. (**b**) Cluster quality indexes I_q [80, 136] are indicated in rank order for each of the 20 components (y-axis). (**c**) Components were projected into 2D space using curvilinear component analysis (CCA). Clusters are enclosed by red convex hulls and grey lines connect similar components. Each of the 20 clusters represent each of the 20 components (labeled within the plot) [120].

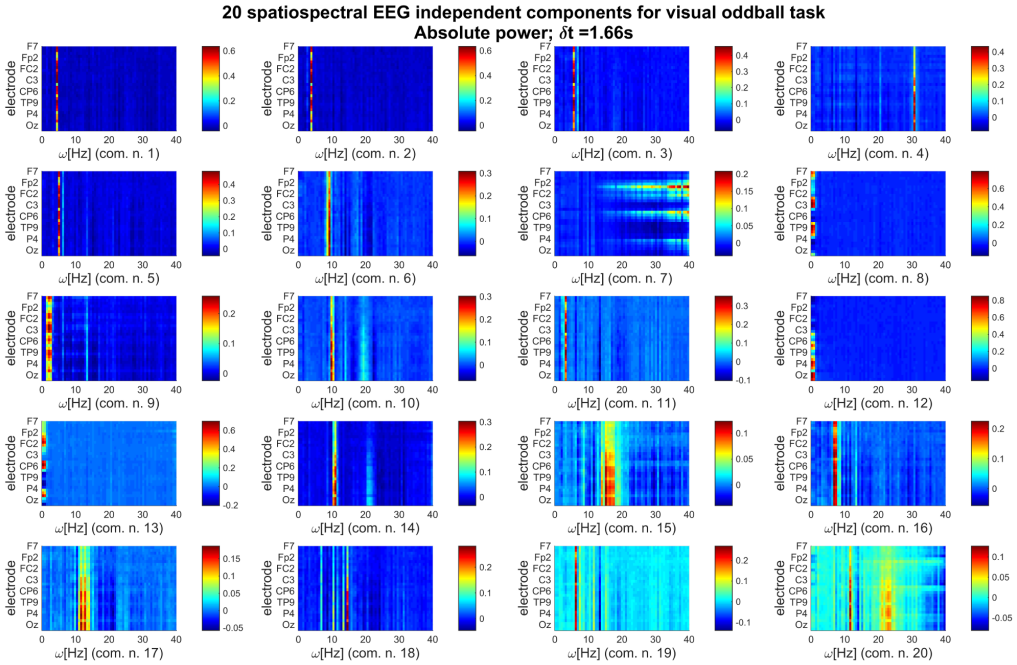

(a)

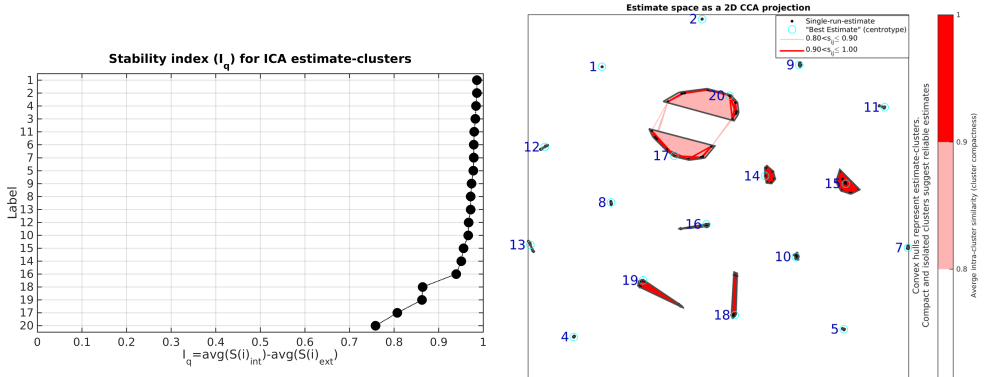

(b)

(c)

Fig. 4.5: Absolute EEG power group-averaged independent EEG spatiospectral pattern results for visual oddball paradigm: (**a**) 20 independent spatiospectral patterns; Spatial distribution of electrodes in matrices is: F7, F3, Fp1, Fz, Fp2, F4, F8, FC6, FC2, FC1, FC5, T7, C3, Cz, C4, T8, CP6, CP2, CP1, CP5, TP9, P7, P3, Pz, P4, P8, TP10, O2, Oz, O1. (**b**) Cluster quality indexes I_q [80, 136] are indicated in rank order for each of the 20 components (y-axis). (**c**) Components were projected into 2D space using curvilinear component analysis (CCA). Clusters are enclosed by red convex hulls and grey lines connect similar components. Each of the 20 clusters represent each of the 20 components (labeled within the plot) [120].

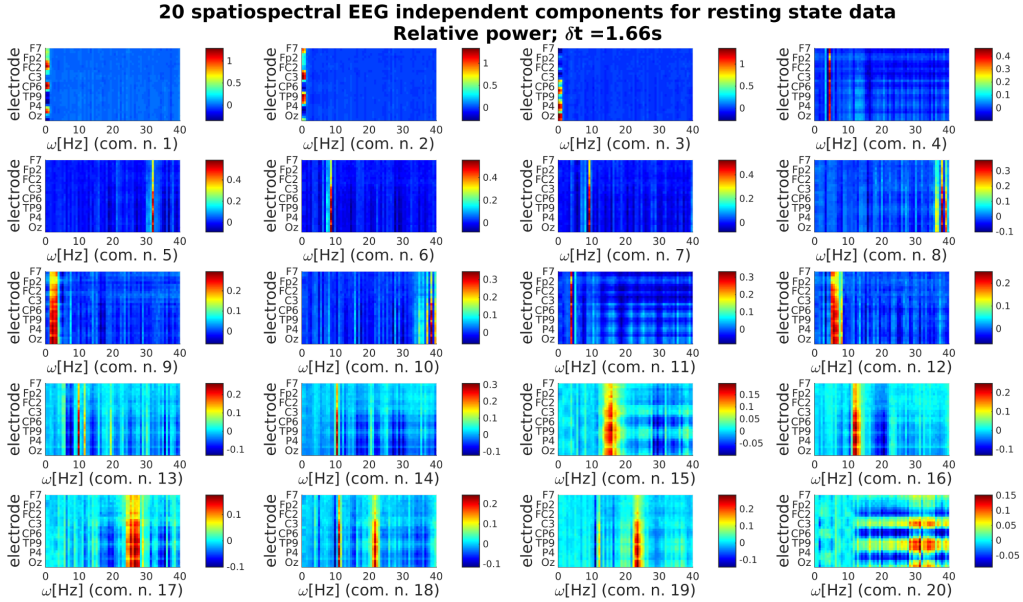

(a)

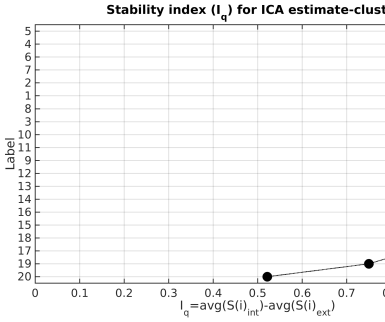

(b)

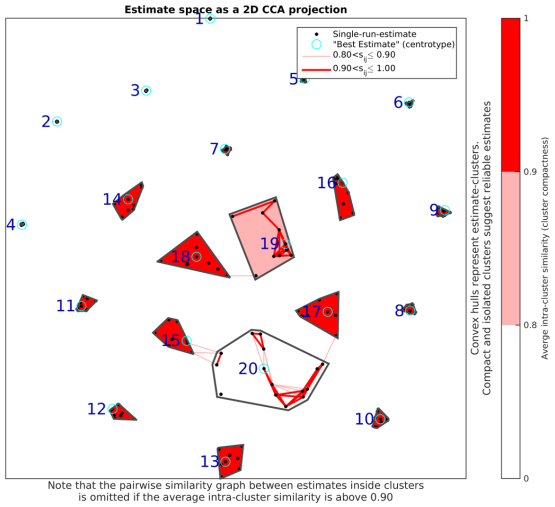

(c)

Fig. 4.6: Relative EEG power group-averaged independent EEG spatiospectral pattern results for resting-state paradigm: (**a**) 20 independent spatiospectral patterns; Spatial distribution of electrodes in matrices is: F7, F3, Fp1, Fz, Fp2, F4, F8, FC6, FC2, FC1, FC5, T7, C3, Cz, C4, T8, CP6, CP2, CP1, CP5, TP9, P7, P3, Pz, P4, P8, TP10, O2, Oz, O1. (**b**) Cluster quality indexes I_q [80, 136] are indicated in rank order for each of the 20 components (y-axis). (**c**) Components were projected into 2D space using curvilinear component analysis (CCA). Clusters are enclosed by red convex hulls and grey lines connect similar components. Each of the 20 clusters represent each of the 20 components (labeled within the plot) [120].

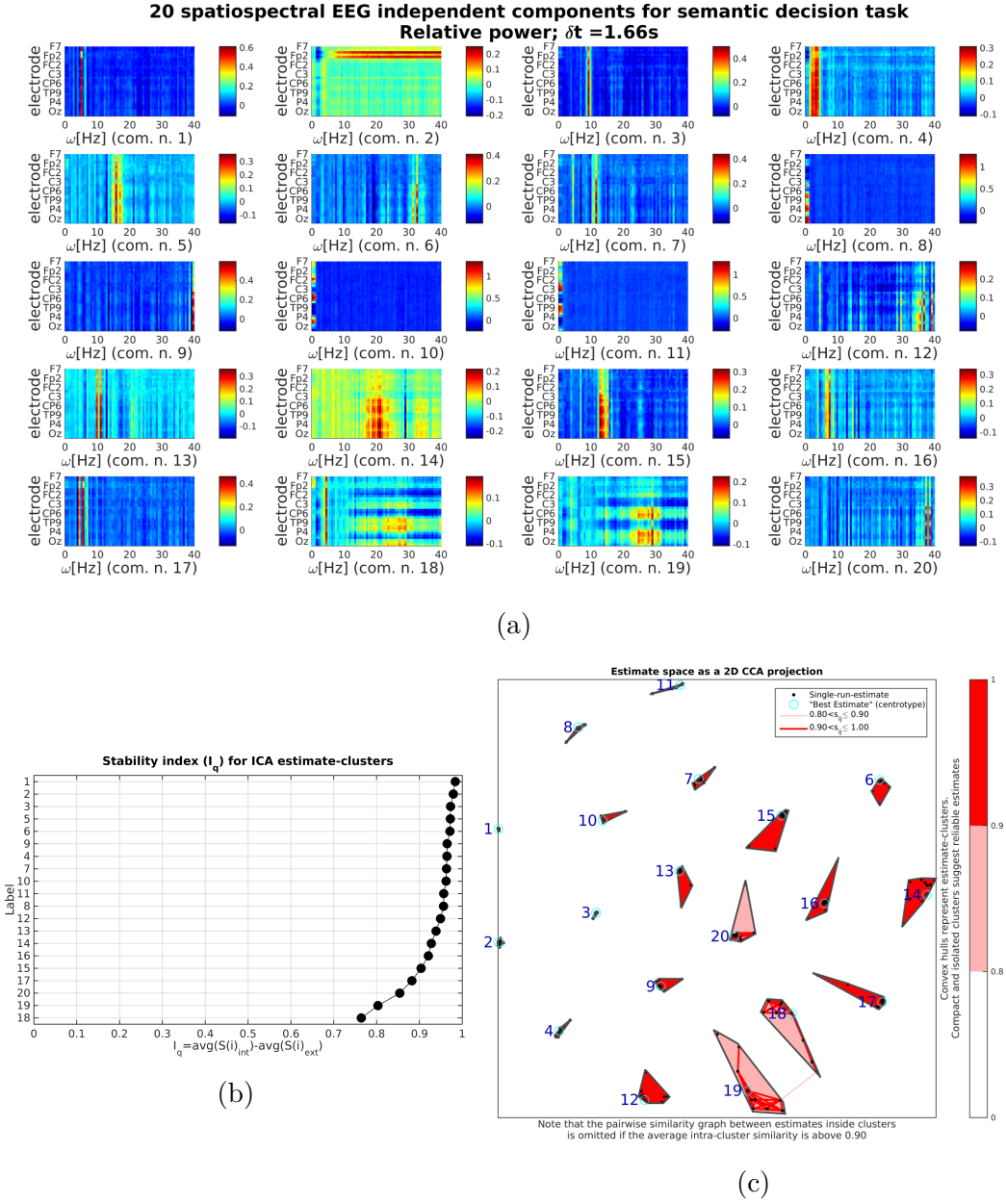

Fig. 4.7: Relative EEG power group-averaged independent EEG spatiospectral pattern results for semantic decision paradigm: (**a**) 20 independent spatiospectral patterns; Spatial distribution of electrodes in matrices is: F7, F3, Fp1, Fz, Fp2, F4, F8, FC6, FC2, FC1, FC5, T7, C3, Cz, C4, T8, CP6, CP2, CP1, CP5, TP9, P7, P3, Pz, P4, P8, TP10, O2, Oz, O1. (**b**) Cluster quality indexes I_q [80, 136] are indicated in rank order for each of the 20 components (y-axis). (**c**) Components were projected into 2D space using curvilinear component analysis (CCA). Clusters are enclosed by red convex hulls and grey lines connect similar components. Each of the 20 clusters represent each of the 20 components (labeled within the plot) [120].

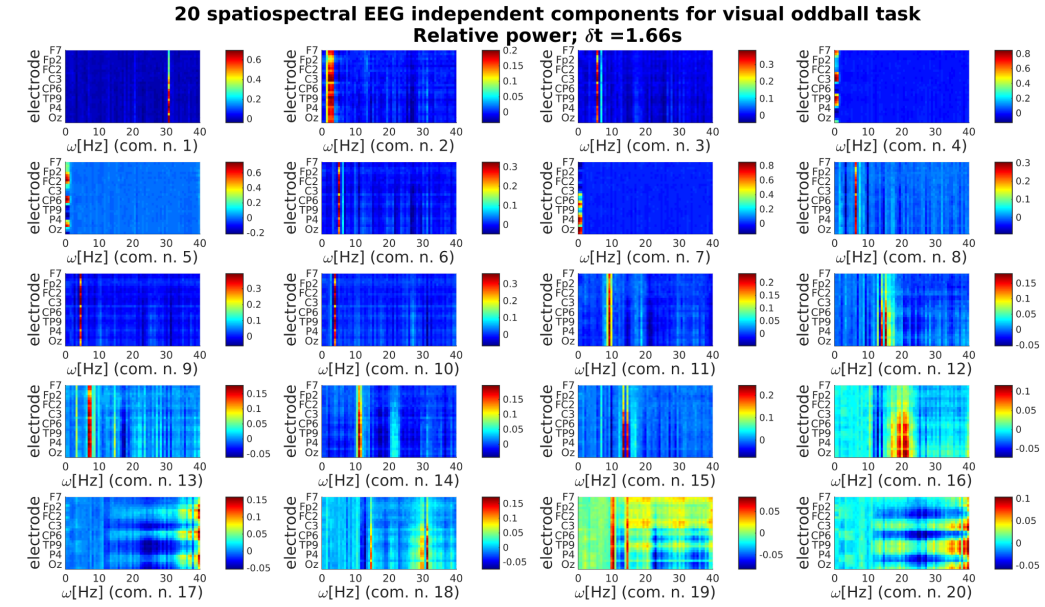

(a)

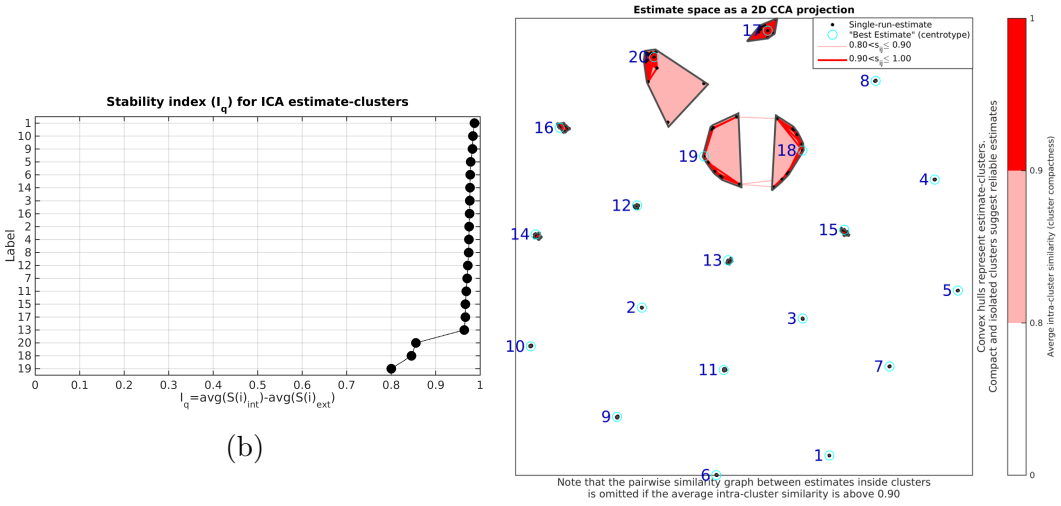

(b)

(c)

Fig. 4.8: Relative EEG power group-averaged independent EEG spatiospectral pattern results for visual oddball paradigm: (**a**) 20 independent spatiospectral patterns; Spatial distribution of electrodes in matrices is: F7, F3, Fp1, Fz, Fp2, F4, F8, FC6, FC2, FC1, FC5, T7, C3, Cz, C4, T8, CP6, CP2, CP1, CP5, TP9, P7, P3, Pz, P4, P8, TP10, O2, Oz, O1. (**b**) Cluster quality indexes I_q [80, 136] are indicated in rank order for each of the 20 components (y-axis). (**c**) Components were projected into 2D space using curvilinear component analysis (CCA). Clusters are enclosed by red convex hulls and grey lines connect similar components. Each of the 20 clusters represent each of the 20 components (labeled within the plot) [120].

Since we have visually observed similar group-averaged spatiospectral patterns, we have designed single-subject k-means clustering of the patterns and tested whether some patterns are really stable over datasets. The obtained results for both power types are presented within following subchapter.

4.3.2 K-means clustering of the spatiospectral patterns

The k-means clustering was performed separately for each power type with same algorithm settings. For each power type, the original 3520 dimensions (i.e. 3520 spatiospectral patterns) were reduced to 40 representative cluster centroids. Forty output clusters were selected after examining the compactness, i.e. σ_{mcv} (characterizing predictive residual variance with eq. 22 in [166]) and σ_{μ} (characterizing residual variance with eq. 10 in [166]) of clusters generated with 2–250 output centroids, and identifying the lowest norm at 40 (see Fig. 4.9). The relationships and distances among the 40 centroids are demonstrated for absolute power within the dendrogram in Fig. 4.10 [120].

All following results will be shown for the absolute EEG power analysis, until the relative power will be mentioned. The cluster spatiospectral features were examined by averaging the patterns separately for each experimental paradigm. These maps appear similar across the three paradigms in instances where many subjects contributed clusters to the average maps, as indicated by cluster 39 within Fig. 4.11. The similarity of patterns within a representative cluster was demonstrated by computing the correlations between spatiospectral patterns within cluster 39 (intra-cluster correlation) and between cluster 39 and the patterns within each of the other clusters (inter-cluster correlations) (Fig. 4.12). The intra-cluster correlations were significantly larger than zero (t-value: 21.67; p-value: $2.2 \cdot 10^{-16}$), while the inter-cluster correlation values did not statistically differ from zero (|t|-values ranged from 0.21 to 1.85 and p-values ranged from $6.5 \cdot 10^{-2}$ to $8.35 \cdot 10^{-1}$ respectively) [120].

While the distributions in Fig. 4.12 are symmetric, the mean intra-cluster and inter-cluster correlation coefficients are indicated within Fig. 4.13a as a summary of the the original 3520 $\times$ 3520 similarity matrix used for k-means clustering. The figure indicates that the majority of inter-cluster correlation coefficients did not statistically differ from 0, while all mean intra-cluster coefficients were significantly larger than 0 (Fig. 4.13b–d).

The Fig. 4.14 demonstrates the full simplified absolute EEG power k-means clustering result over all three tested paradigms. The simplified result visualization is shown in Fig. 4.15, where representative spatiospectral map is demonstrated for each cluster and radial dendrogram projection is included. K-means clustering

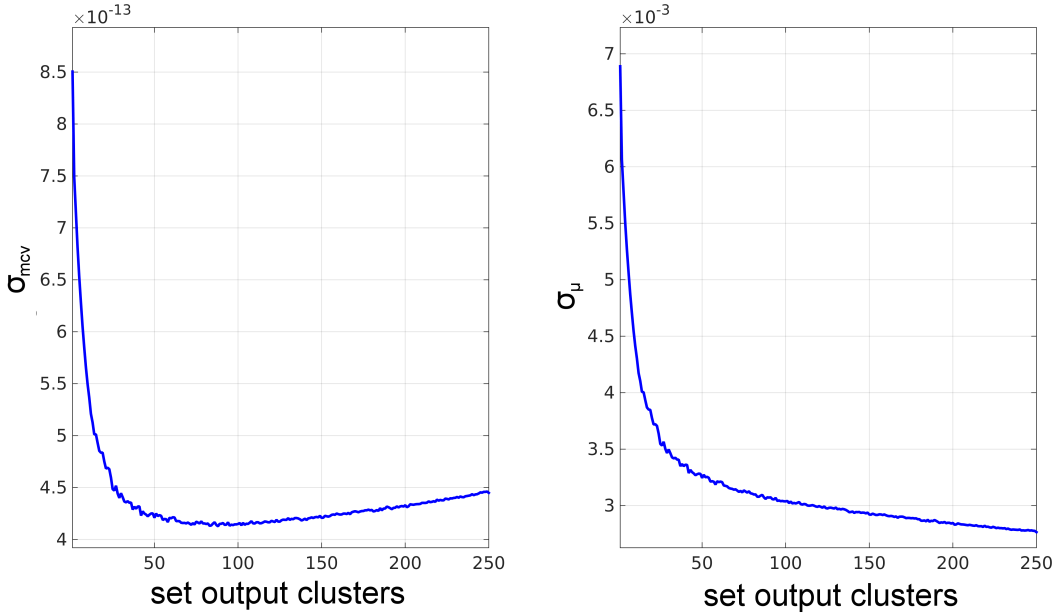

(a) Residuals for the absolute power

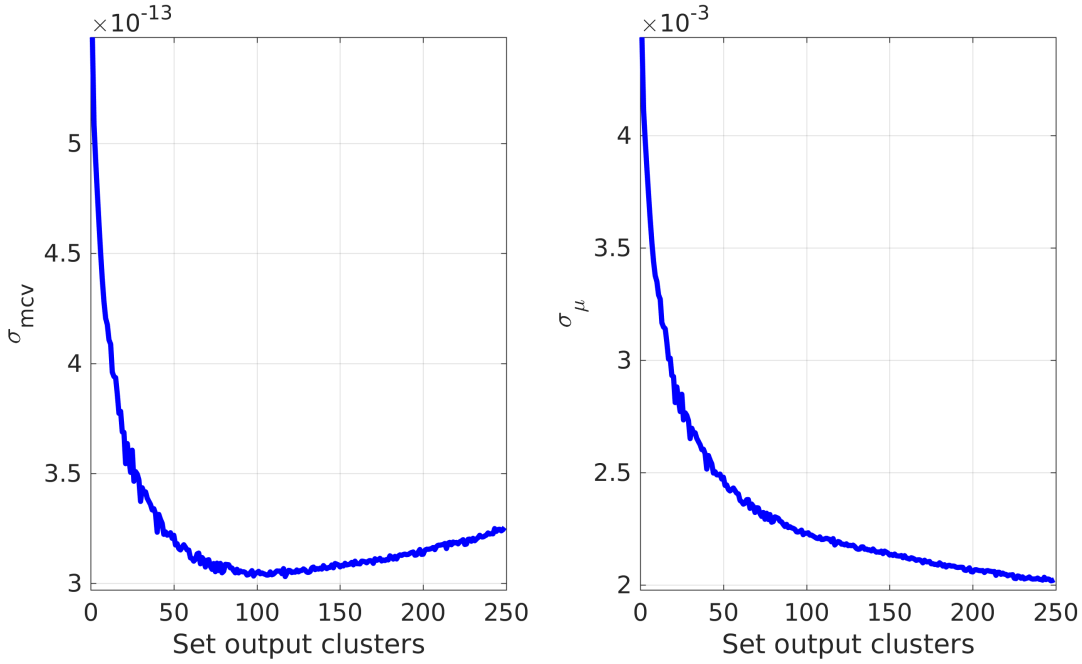

(b) Residuals for the relative power

Fig. 4.9: Residual variance (σ_μ; eq. 10 in [166]) and predictive residual variance (σ_{mcv}; eq. 22 in [166]) observed over a range of output cluster numbers. The norm appears to be the lowest around 40 for each function, thus, we have used 40 output clusters within the current manuscript [119, 120].

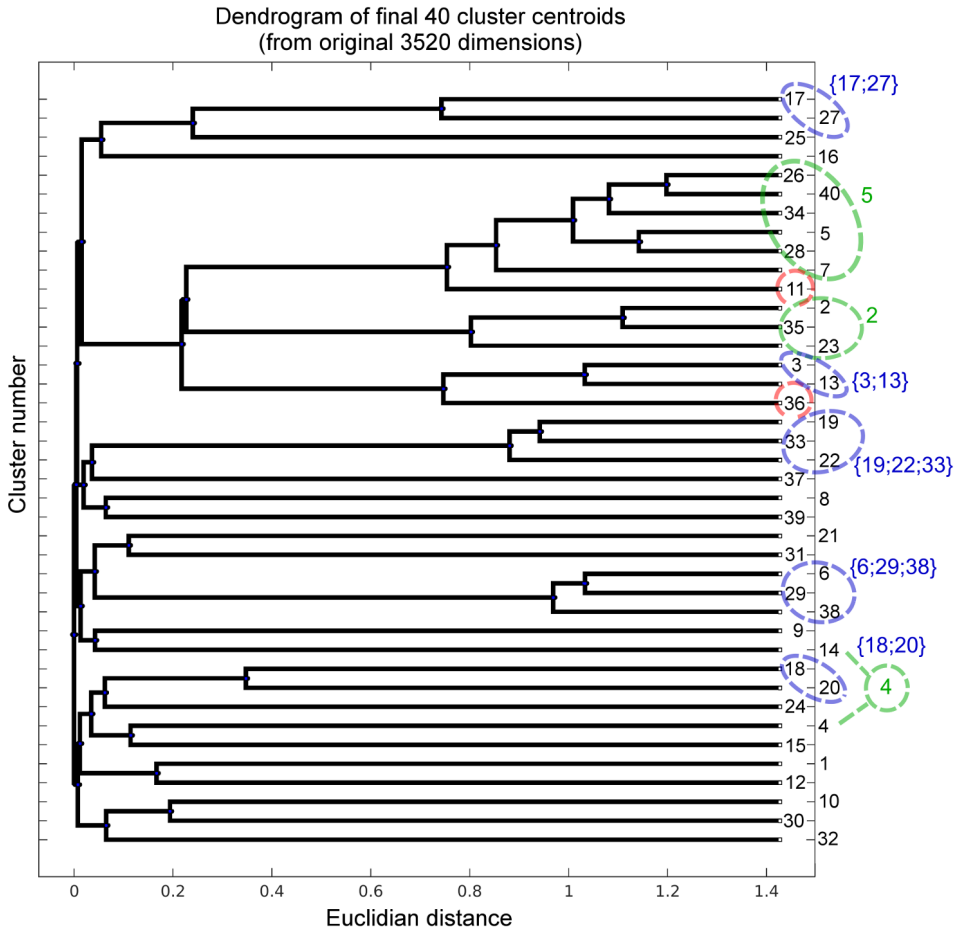

Fig. 4.10: Dendrogram of 40 clusters for absolute power: The greencircled clusters are the clusters combined during post-processing described within the Materials and Methods. The blue-circled clusters are the clusters which were not combined in post-processing, but were combined post hoc based upon visual inspection of the spatiospectral patterns. The red-circled clusters are residuals which account for less than 5% of the single-subject spatiospectral patterns within any experimental paradigm. [120].

analysis indicates that similar EEG spatiospectral patterns appear across different tasks. Fifteen clusters (cl. numbers 2, 4, 5, 9, {13; 3}, 16, {17; 27}, {18; 20}, 30, 32, 37, 39) define 12 different spatiospectral patterns which are observable in all tasks, with more than 89% of subjects from each dataset present within each cluster. In general, these spatiospectral maps appear consistent with maps generated in previous studies [21, 23] and appear biologically plausible, demonstrating power within characteristic EEG frequency bands [120].

The spatiospectral pattern in cluster 27 (4.14) appears to capture eye artifacts, with peak values appearing over frontal electrodes. This cluster may have separated

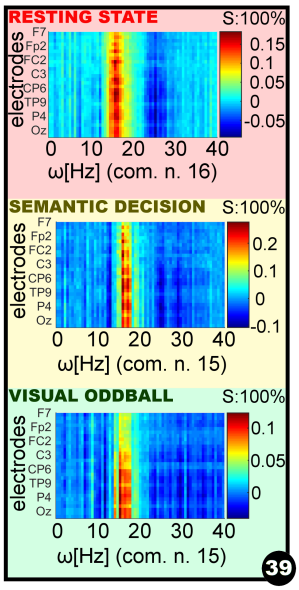

Fig. 4.11: Cluster 39 as an example of the k-means clustering output: The spatiospectral patterns were averaged for each experimental paradigm and cluster. The *number on the upper right* (e.g. "S:") indicates the percentage of subjects who belong to the cluster. The spatial distribution of electrodes in each plot is: F7, F3, Fp1, Fz, Fp2, F4, F8, FC6, FC2, FC1, FC5, T7, C3, Cz, C4, T8, CP6, CP2, CP1, CP5, TP9, P7, P3, Pz, P4, P8, TP10, O2, Oz, O1 [120].

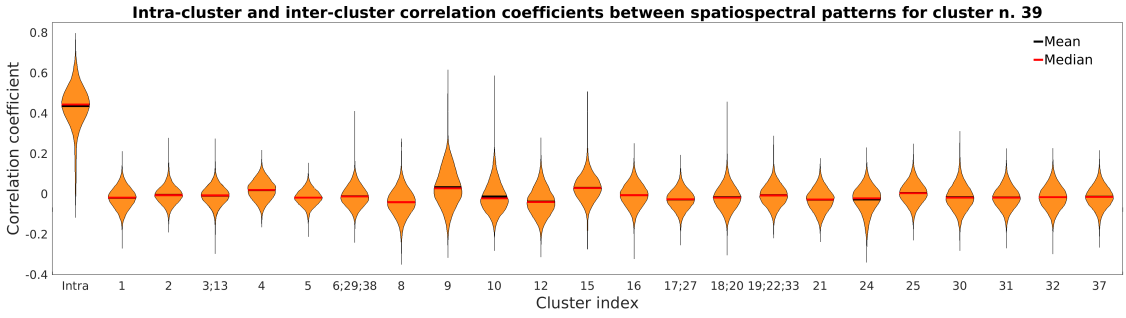

Fig. 4.12: K-means intra-cluster and inter-cluster correlation coefficients for cluster n. 39.: The violin plots indicate the distribution of intra-cluster correlations (leftmost plot) and the 22 distributions of inter-cluster correlations (i.e. the distribution of correlations between the patterns of cluster 39 patterns and the patterns within the other post-processed clusters, as indicated on the x-axis). [120].

from cluster 17 likely due to different EEG preprocessing steps (i.e. eye-blink artifact correction applied to VOT but not RST-eye-closed or SDT data). Clusters number 1 and 12 (4.14) consist of components with maximal narrow-band power slightly

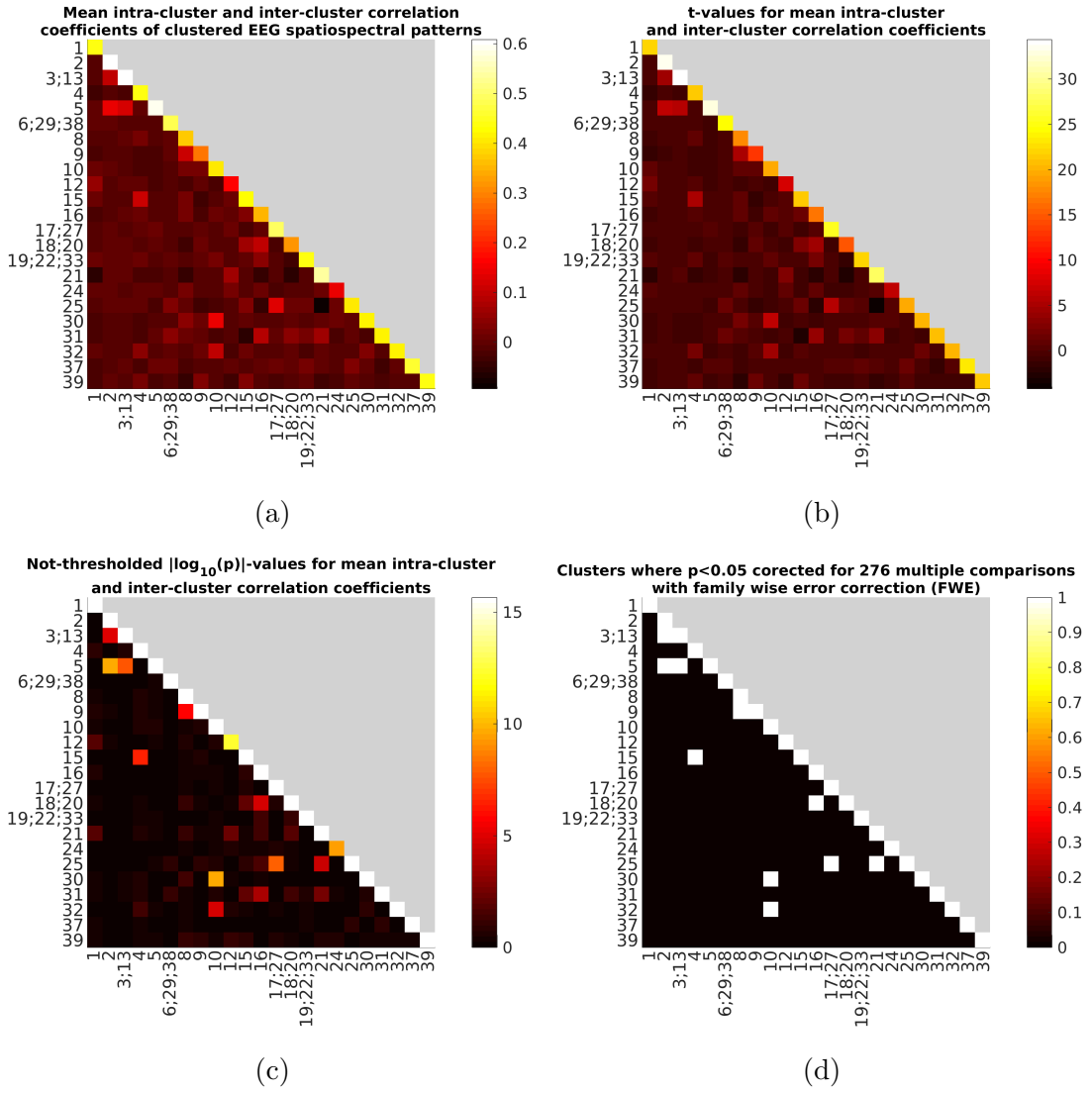

Fig. 4.13: Mean intra-cluster (*main diagonal*) and inter-cluster (*below the main diagonal*) correlation coefficients (**a**) over the final k-means clusters, the probabilities [the p values (**c**), derived from correlations coefficients through t-values (**b**)] indicating the likelihood that the observed correlations differed from zero by chance and the supra-thresholded p FWE <0.05 (**d**). The labels indicate the final cluster indexes (see Fig. 4.10) [120].

above 30 Hz, and cluster 24 appears to comprise a collection of residual (i.e. unique) spatiospectral patterns [120].

Two spatiospectral patterns which are observable in all datasets were divided at six disjunctive clusters where each cluster belongs to one specific dataset. On both the standard dendrogram (Fig. 4.10) and the radial dendrogram projection (Figs. 4.14 and 4.15), these clusters form 2 different but neighbouring groups and each

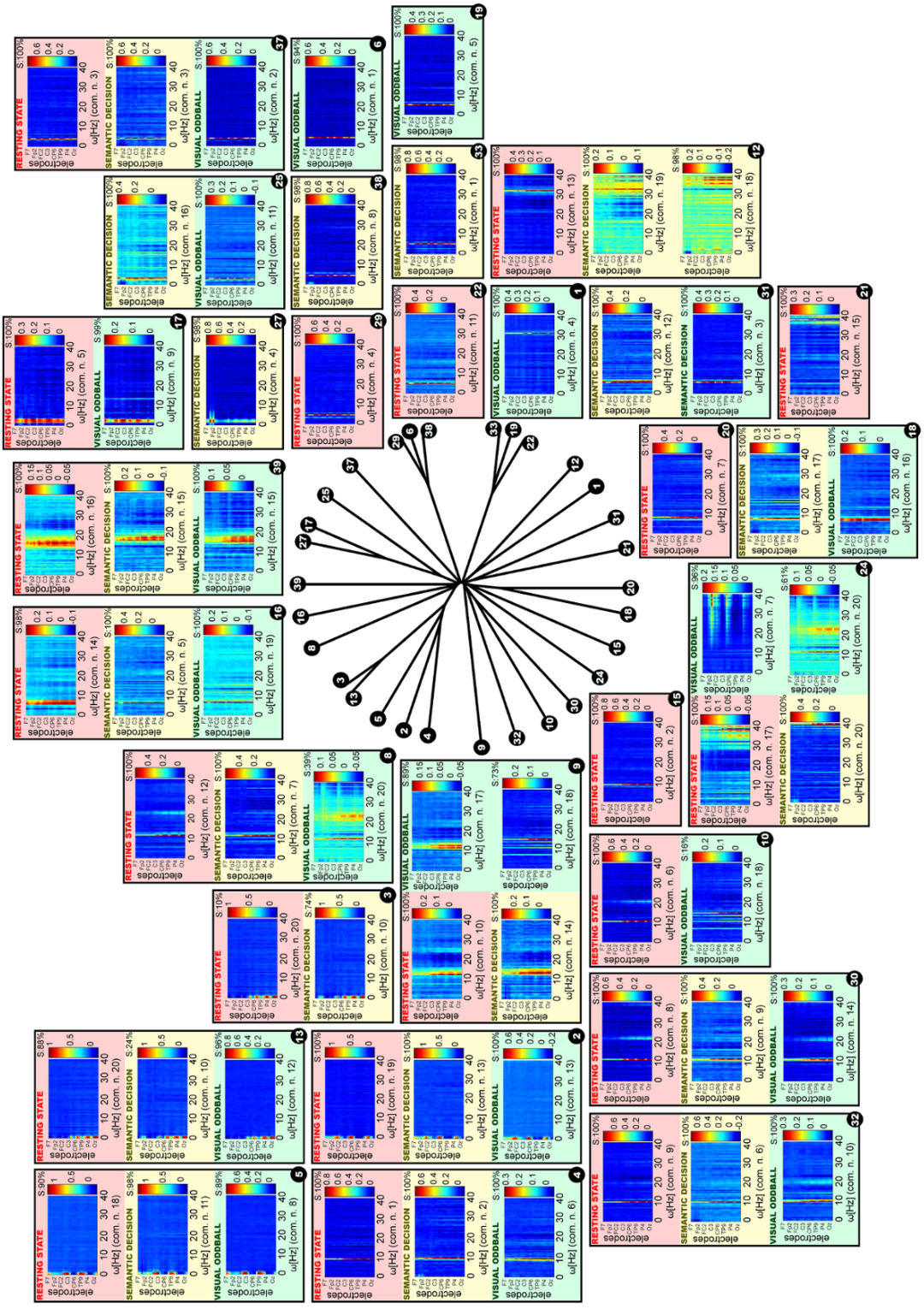

Fig. 4.14: Full absolute EEG power k-means clustering result visualization over all tested paradigms: The radial dendrogram projection is visualized in the center. The legend for the descriptive cluster informations are the same as in Fig. 4.11 [120].

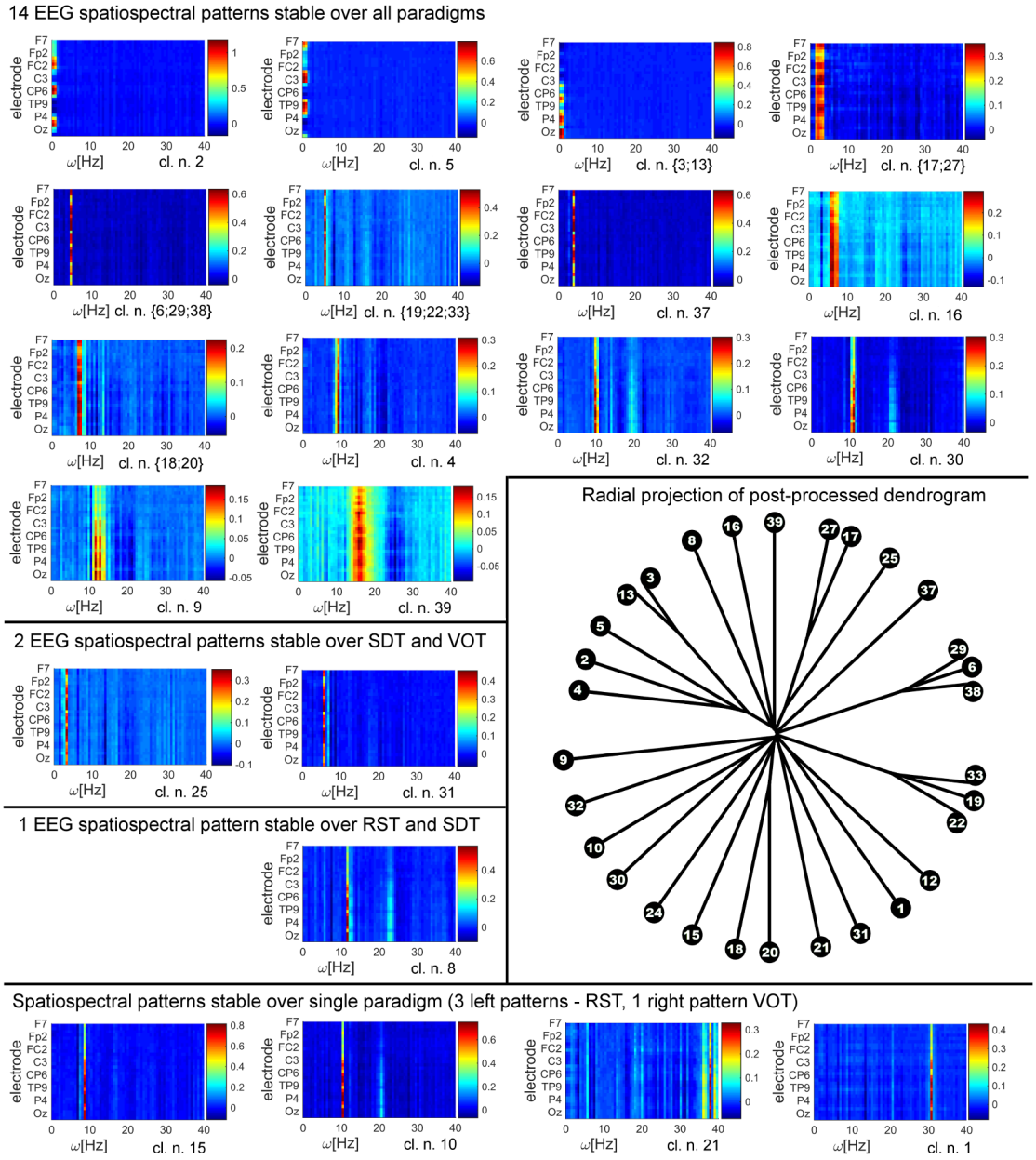

Fig. 4.15: Simplified absolute EEG power k-means clustering result visualization over all tested paradigms: The legend for the descriptive cluster informations are the same as in Fig. 4.11 [120].

group corresponds to an unique spatiospectral pattern (cl. numbers $\{6; 29; 38\}$ and $\{19; 22; 33\}$) [120].

As demonstrated in Figs. 4.14 and 4.15, 21 of 30 clusters characterize 14 different spatiospectral patterns which are observable and relatively stable in all three datasets. For exceptions, we note that clusters 25 and 31 contain some spatiospec-

tral patterns which are present only during task, while the patterns of clusters 10 and 15 were present only during "rest" [120].

For the relative EEG power, we have got following k-means clustering results. Twenty-one of the 40 output clusters were organized into 16 final K-means clusters (Fig. 4.16) whose spatiospectral patterns appear to be of physiological origin. Thirteen clusters were not included since their patterns consisted of single-frequency peak which appeared artefactual, and which was not present over the 3 paradigms. The remaining 6 excluded clusters contained less than 5% of single-subject patterns of at least one paradigm and are thus considered noise. Twelve of the sixteen patterns derived from relative EEG power were stable over all three paradigms (Fig. 4.16a,b). Of these twelve stable sources, ten appeared visually similar to patterns that were observed for absolute EEG power (Fig. 4.16a). Two stable γ-band patterns (Fig. 4.16b) were present with relative power but not with absolute power. One cluster representing β-band activity ($\sim$20Hz) was present for SDT and VOT data but not RST (Fig. 4.16c). For the cl. n. 29, the spatial distribution of the pattern looks identical over paradigms, but the frequency peak within relative power maps appears to differ across paradigms (Fig. 4.17). Three clusters contained maps (one θ-band and two γ-band patterns) which were present during RST but not SDT or VOT (Fig. 4.16d) [119].

4.3.3 Relationships between spatiospectral pattern time-courses and stimulus vectors

The t-values of relationships between EEG spatiospectral pattern time-courses $\boldsymbol{A}$ and stimulus vectors are listed in Table 4.1. Distributions of |t|-values over different power types are shown in Fig. 4.18. The critical t-values rejecting the null hypothesis, that there is no evidence between compared signals, is 2.1 for $p<0.05$ uncorrected, 3.0 for $p<0.05$ corrected (FWE correction) and 3.22 for $p<0.001$ uncorrected for multiple comparisons. Although significant relationships with stimulus vectors were found for both power types, there appears to be no statistically significant difference in the distribution of |t|-values computed between the two (Fig. 4.18). The difference between absolute or relative power relationships with the stimuli (Fig. 4.18) is $p < 0.162$ based on two-sample t-test between distributions or $p < 0.150$ based on a 10 000 sample bootstrap test. |t|-values are not normally distributed, since the p-values of one-sample Kolmogorov-Smirnov tests are $p < 6.1 \cdot 10^{-14}$ for the absolute power and $p < 1.8 \cdot 10^{-12}$ for the relative power [119].

The most of the tests did not reach statistical significance using conservative corrections for multiple comparisons. And probably, it is more true for the absolute EEG power than for the relative EEG power (Fig. 4.18). Thus, it is likely that

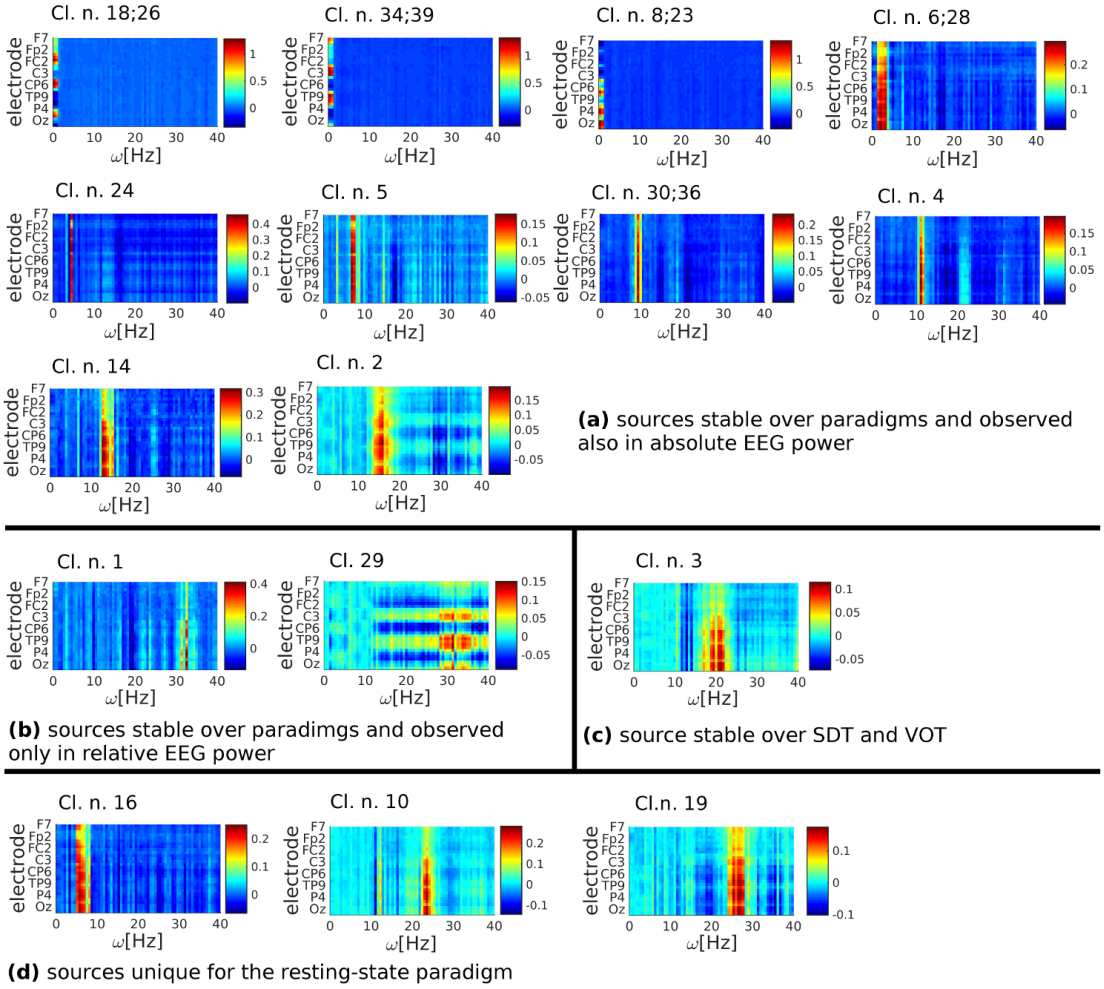

Fig. 4.16: Relative EEG power k-means clustering result visualization: The legend for the descriptive cluster informations are the same as in Fig. 4.11 [119].

the dynamics of EEG's spatiospectral patterns are a mixture of the task-evoked neuronal activity and neuronal activity of task unrelated process (e.g. default mode activity).

For the absolute power, the majority of uncorrected statistical effects appear for the VOT (higher t-values for 7 patterns from 14 different stable clusters, Table 4.1) than for the SDT (any higher t-values, Table 4.1). The SDT t-value for the cluster $\{17; 27\}$ were not taken into account, since the estimated spatiospectral pattern contains modulated eye-blink artifact (Fig. 4.14). For the relative power, more corrected supra-thresholded t-values are observed and togehted with uncorrected significant effects we have got for VOT 7 higher t-values from 13 stable clusters and for SDT 1 higher t-value.

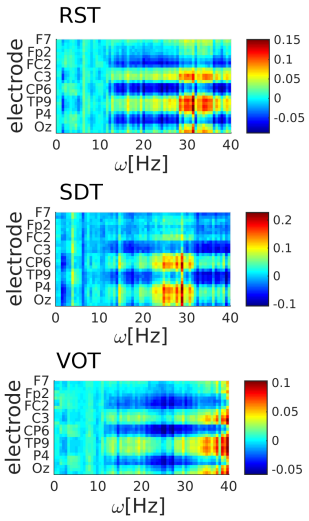

Fig. 4.17: Similar spatial pattern and variable peaks in aggregated relative power of the cl. n. 29 over paradigms [119].

Tab. 4.1: Relationships between timecourses $\boldsymbol{A}$ and stimulus vectors: The black bold highlighted values are t-values with p<0.05 uncorrected for multiple comparisons. The green bold highlighted values are t-values with p<0.05 corrected for multiple comparisons (FWE correction).

Absolute power					Relative power				
Cl. n.	frequent	target	distractor	sentences	Cl. n.	frequent	target	distractor	sentences
2	-1.13	0.43	-0.52	0.93	1	-0.58	-1.86	0.21	0.08
5	-0.81	1.77	0.31	-0.63	2	**-3.74**	-1.40	-1.31	-0.05
3;13	-1.45	**2.43**	0.21	-0.09	4	0.12	0.21	0.40	**-2.88**
17;27	-2.09	0.24	**-2.24**	-	5	-0.13	1.14	-1.50	0.76
19;38;6	-0.34	**2.37**	-0.25	-1.63	14	**-3.28**	-1.44	-0.97	0.26
22;33;19	-0.27	-0.23	-0.97	-0.25	24	-2.03	**2.17**	0.01	0.24
37	-1.13	-0.40	0.56	-0.73	29	-0.08	0.57	0.47	0.33
16	**-2.47**	1.20	-0.83	-0.72	8;23	-1.45	**2.46**	-0.35	0.01
18;20	0.39	0.39	-1.00	-1.45	34;39	-0.92	**2.63**	1.30	-0.86
4	1.72	**2.62**	0.56	-0.86	18;26	-1.01	1.45	-0.43	1.00
32	1.67	0.73	0.12	-1.10	6;28	**-4.32**	1.04	-1.46	-0.29
30	**2.48**	0.58	-0.34	-1.87	30;36	**2.59**	1.82	1.65	-1.67
9	**-3.23**	-0.52	-0.61	0.21	3	2.06	-0.86	-1.86	0.27
39	-0.17	-0.06	-0.61	0.21					

4.3.4 Absolute EEG power topologies and spectral densities

The topographies and spectral densities of the 14 stable spatiospectral patterns (Fig. 4.19a) appear biologically plausible, with spectral peaks that appear within characteristic EEG frequency bands. In addition, the spatiospectral patterns gen-

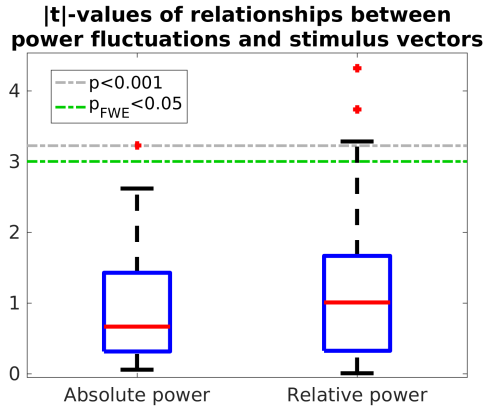

Fig. 4.18: Relationships between timecourses of stable spatiospectral sources and stimulus vectors: using absolute and relative EEG power as input to group-ICA [119].

erally demonstrate similar topographies across the RST and VOT datasets. The SDT dataset appears corrupted by the eye-blink artifacts as described later. Twelve out of 14 topographies appear similar between the RST and VOT datasets, while 5 topographies appear similar across all 3 datasets (cl. n. 2, 5, $\{13;3\}$, $\{29;38;6\}$, $\{22;33;19\}$ and 39).

The independent spatiospectral maps potentially differ due to differences in topography or spectral peak. For example, three independent low δ-band (0-1.5Hz) patterns (clusters number 2, 5 and $\{13;3\}$) show peak topographic responses over right temporal regions (cluster 2), left temporal regions (cluster 5), and occipital/parietal regions (cluster $\{13;3\}$). The high δ-band (1.5Hz-4Hz) and θ-band (4-8Hz) patterns (cl. n. $\{17;27\}$, $\{29;38;6\}$, $\{22;33;19\}$, 37 and 16) are spatially similar with bilateral peaks located over frontal and fronto-temporal areas, with a peak decrease around the midline. Cl. n. $\{18;20\}$ demonstrates the highest power within the upper θ-band, but differs in scalp topography across datasets. Three independent α-band (8-12Hz) patterns (cl. n. 4, 30 and 32) were present with spatially different topographies (i.e. central-parietal areas for cl. n. 4, bilateral occipital areas for cl. n. 30 and right occipital areas for cl. n. 32). The low β-band (10-15Hz) pattern (cl. n. 9) differs spatially across tasks and the high β-band (12-20Hz) pattern (cl. n. 39) shows peak power around right frontal and fronto-central areas. In general, the different topographies suggest that the different components (i.e. different patterns) have spatially different generators.

It is interesting to note that the average power spectral densities overlap for all three datasets, (see Fig. 4.19a). However, wider confidence intervals were observed for the SDT tasks compared to the RST and VOT tasks (e.g. cl. $\{17;27\}$ or 9).

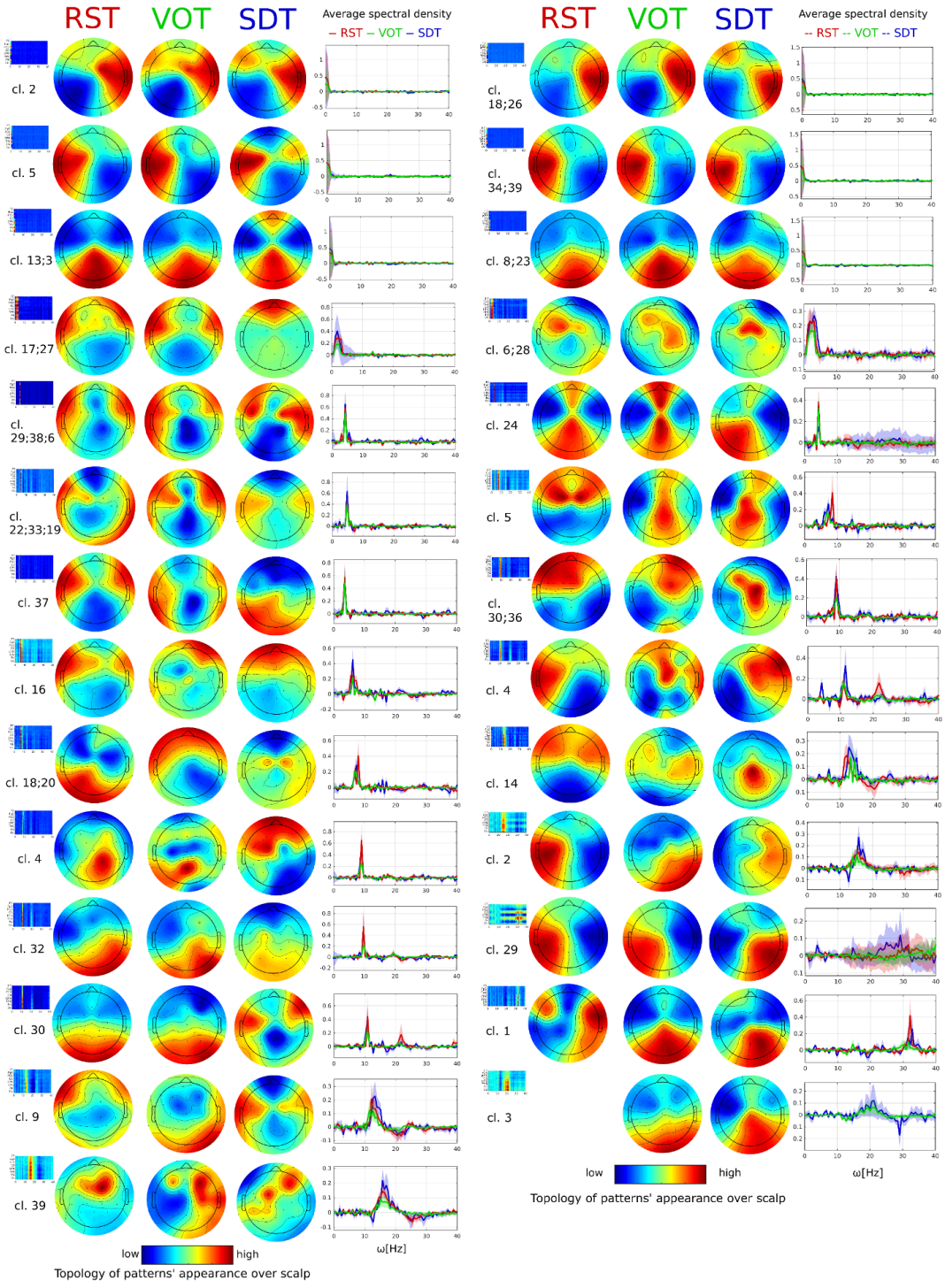

(a) absolute power

(b) relative power

Fig. 4.19: Scalp topologies of EEG spatiospectral patterns and their average spectral densities: The shaded regions within the spectral density plots indicate the 95% confidence interval of the mean for RST (red), VOT (green), and SDT (blue).

4.3.5 Relative EEG power topologies and spectral densities

The spectral densities of relative power spatiospectral patterns appear to have peaks with characteristic EEG frequency bands (Fig. 4.19b) similarly as for the absolute power. Similarities of topologies over all three paradigms is observed for lots of the stable patterns (Fig. 4.19b). For the most of the patterns, the similarity is observed at minimum over two paradigms. The δ-band topologies (cl. n. $\{18; 26\}$, $\{34; 39\}$, $\{8; 23\}$) demonstrate to be identical to absolute power topologies (Fig. 4.19). The eye-blinking artifact observed over SDT absolute power topologies seems to be suppressed in stable relative power topologies. The wide range θ-band pattern (cl. n. $\{6; 28\}$) appears to have the source in middle frontal areas (Fig. 4.19b). Narrow band low and high θ-band pattern sources (cl. n. 24 and 5) are around the midline more than for the absolute power (Fig. 4.19). The α-band (cl. n. $\{30; 36\}$ and 4) and β-band (cl. n. 4 and 14) sources are quite heterogeneous across the paradigms (Fig. 4.19b). One stable γ-band pattern (cl. n. 29) has similar topologies over all datasets, only the SDT topology has switched polarity (Fig. 4.19b). The second stable γ-band pattern has stable source only across VOT and SDT datasets (Fig. 4.19b). The high β-band pattern (cl. n. 3) stable only across VOT and SDT datasets seems to have same source in occipital areas (Fig. 4.19b).

4.3.6 Absolute power EEG-fMRI F-maps and IRFs

FMRI F-maps were generated with the individual EEG spatiospectral time-courses as regressors (Fig. 4.20 and Appendix A). While 12 of 14 F-maps demonstrate supra-threshold voxels for the VOT task, 9 of 14 were supra-threshold for RST, and only 4 of 14 were supra-threshold for SDT. In terms of absolute F-values, the strongest values were observed for VOT data. The values are lower for the RST and SDT datasets except for the SDT EEG-fMRI map corresponding to cl. n. $\{17; 27\}$. This pattern appears to reflect eye-blinking artifacts, however, as suggested by Figs. 4.14 and 4.19a. The robust supra-threshold activations in visual cortices (Fig. 4.20) support the hypothesis that this result is due to shared physiological noise between the two signals, and not due to relationships between the EEG and fMRI signals directly. The other 3 SDT supra-threshold maps show similarity with RST and VOT maps for the corresponding EEG patterns (Fig. 4.20 and Appendix A).

Significant EEG-fMRI activations were observed for the VOT task within sensory-motor and basal ganglia networks for 5 θ-band patterns (similar locations were present with lower F-values and lower cluster size within the RST and SDT datasets) (Figs 4.20, Figure 4.21a and Appendix A). EEG-fMRI networks partially overlapped for 2 δ-band (cl. 2 and 5) and low β-band (cl. 9) patterns (Fig. 4.22 and Appendix A). The δ-band F-statistic patterns overlapped with the basal ganglia, while the

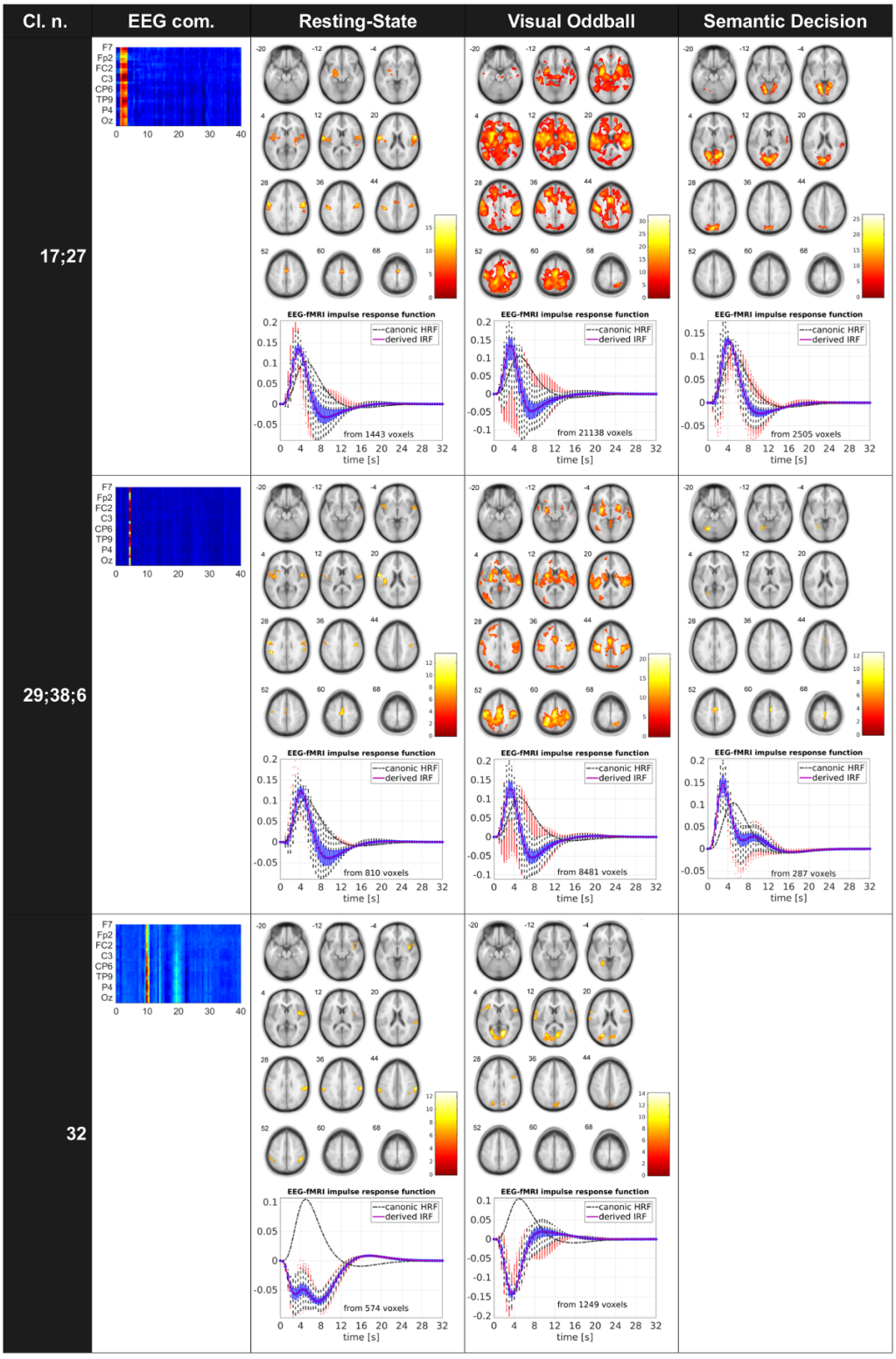

Fig. 4.20: Example of supra-threshold group-averaged EEG-fMRI results: for three different absolute power EEG spatiospectral patterns and RST, VOT and SDT datasets ($p<0.001$ uncorrected).

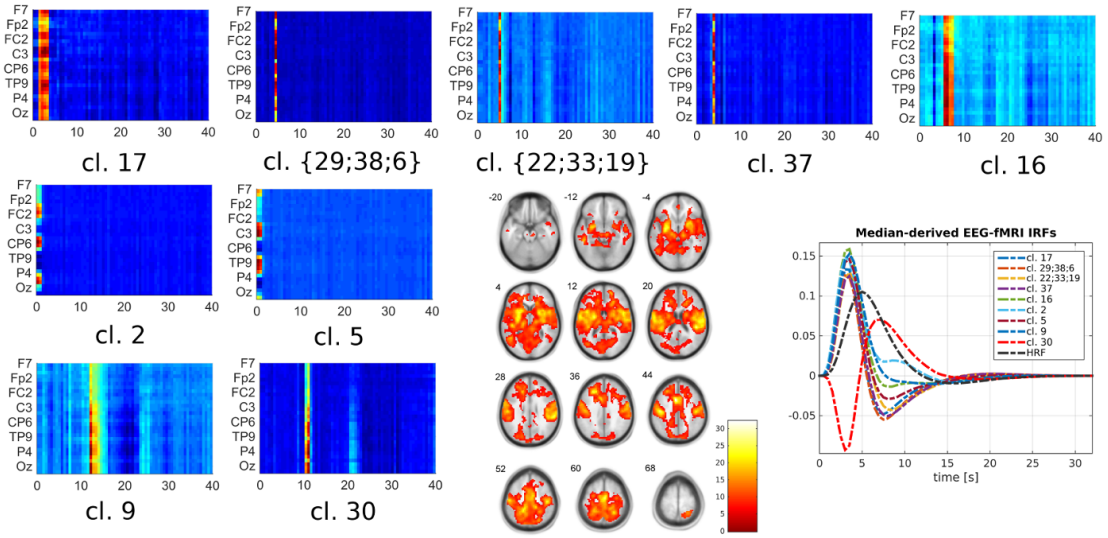

(a) Sensory-motor and basal ganglia networks

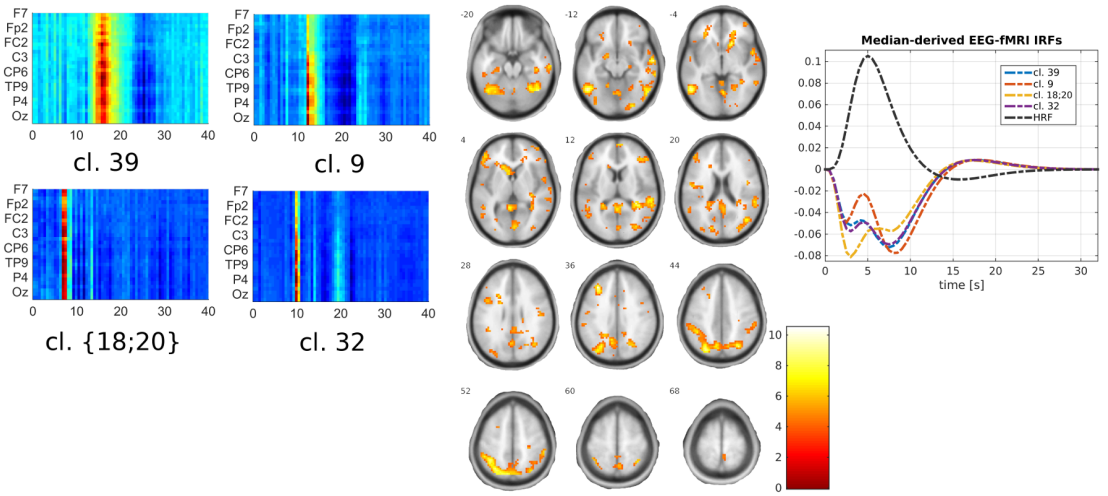

(b) Attention network

Fig. 4.21: Sensory motor and basal ganglia EEG-fMRI networks observed during VOT and attention EEG-fMRI networks observed during RST (p<0.001 uncorrected).

low β-band pattern overlapped with the left lateralized sensory-motor areas (i.e. consistent with the relationship between its time-course and the frequent stimulus vector, demonstrated in Table 4.1). The 3^{rd} δ-band pattern $\{13; 3\}$ demonstrates supra-threshold F-values within the basal ganglia for the RST data.

The independent α-band patterns (with differing topographies; Fig. 4.19a) correspond with fMRI activity within non-overlapping voxels within the VOT task (Fig. 4.23). The α-band pattern of cluster 32 is unrelated to the stimulus timings (Table 1), despite its association with deactivations in primary visual cortical

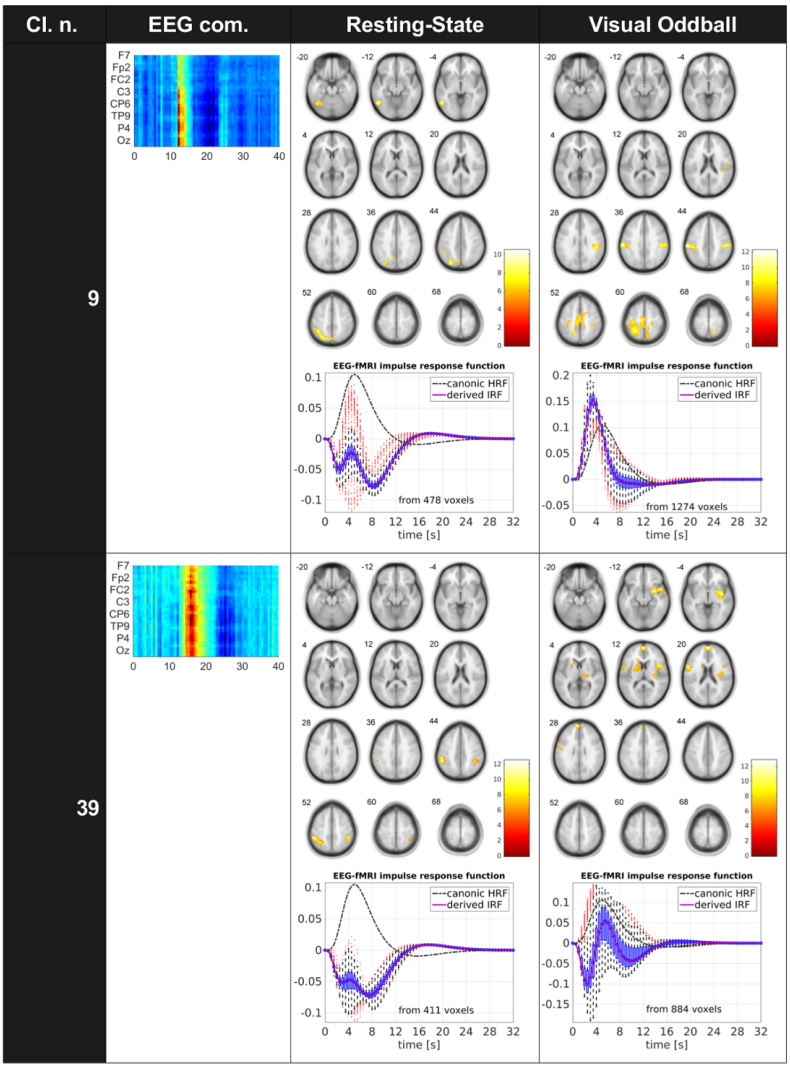

Fig. 4.22: EEG-fMRI group-averaged F-maps for EEG low and high β-bands: for RST and VOT tasks, and HRFs derived from supra-threshold voxels ($p<0.001$ uncorrected).

fMRI responses (Figs. 4.20 and 4.23a, and Appendix A). The α-band pattern of cluster 4 was associated with deactivations within secondary visual cortical fMRI regions, which are associated with target stimulus timings (Fig. 4.23b, Table 4.1 and Appendix A). This finding indicates that the α-band pattern which covaries with secondary visual cortical fMRI fluctuations may be related to cognitive processes that are related to processing target stimuli. The α-band pattern within cluster 30 corresponds with deactivations in sensory-motor cortices, secondary visual cortices and left superior frontal gyrus, with activations in the default mode network, left paracentral lobule and right insula (Fig. 4.23c and Appendix A). Results in Table 4.1 indicate that it is related to frequent stimulus timings.

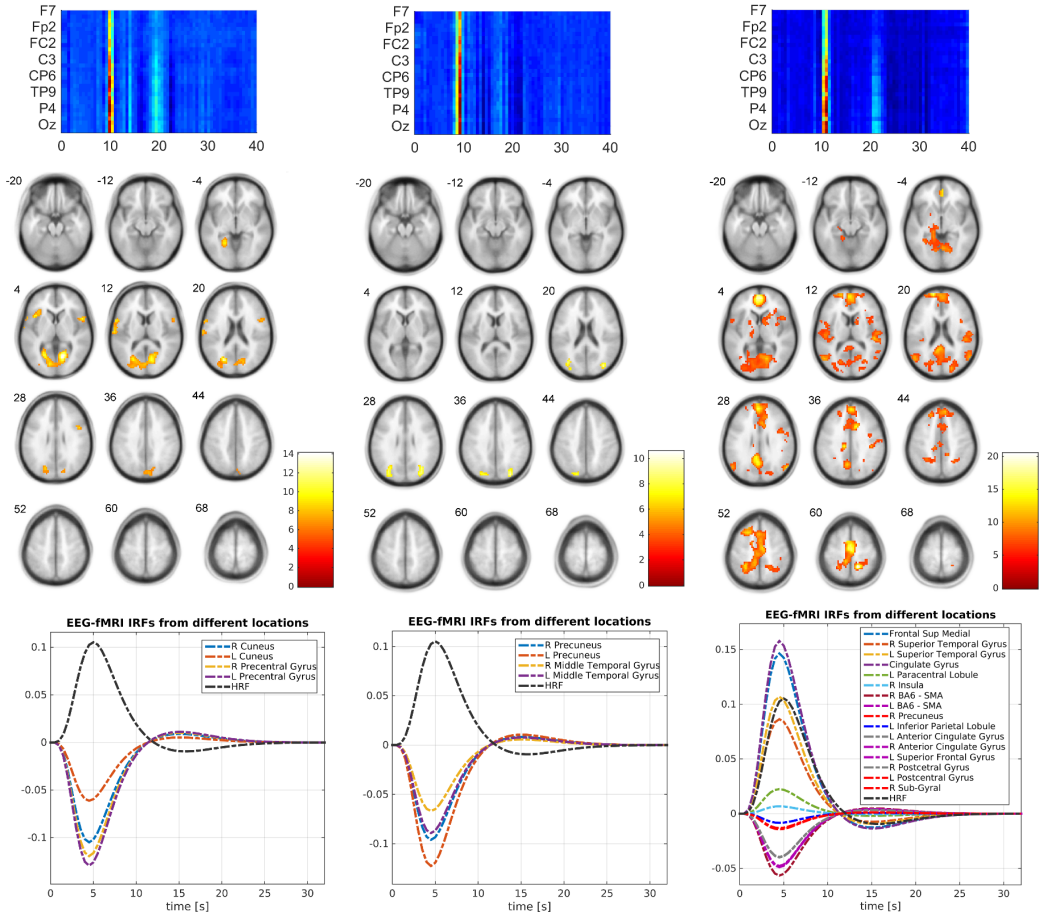

(a) cluster 32 (b) cluster 4 (c) cluster 30

Fig. 4.23: EEG-fMRI absolute α-band results: Three different EEG-fMRI networks from the VOT task generated from three independent EEG spatiospectral α-band patterns and their local HRFs estimated with eq. 4.9 from local maximums of the supra-threshold clusters ($p<0.001$ uncorrected).

The high β-band pattern (cl. 39), with consistent topographies across paradigms (Fig. 4.19a), is associated with supra-threshold F-map activations within the salience network during VOT. However, results in Table 4.1 indicate that it is unrelated to stimulus timings (Fig. 4.22). For RST and SDT datasets, we generally observed less significant, but similar, F-statistic overlays for θ-band patterns compared to VOT. In addition, within RST we observe F-statistic map activations within the attention network for the low and high β-band patterns, the θ-band pattern of cluster $\{18; 20\}$ and the α-band pattern of cluster 32 (see in Figs. 4.23b and 4.22, and Appendix A).

Fig. 4.20, Fig. 4.22 and the Appendix A demonstrate the distribution of estimated HRFs across supra-threshold voxels. From those distributions, Fig. 4.21

demonstrates the median-derived HRFs over different spatiospectral patterns for several brain networks. Fig. 4.23 demonstrates local HRFs for 3 independent α-band patterns from the EEG-fMRI supra-threshold clusters within the VOT dataset.

The VOT HRFs generated from the α-band patterns primarily demonstrate negative peaks with similar timings as the canonical HRF (Fig. 4.23). The positive HRF peaks derived from cluster n. 30 also demonstrate similar timings as the canonical HRF (Fig. 4.23c).

While VOT mean-derived HRFs with the EEG δ-band components (cl. 2 and 5) demonstrate positive HRF peaks, the RST mean-derived HRFs with the EEG δ-band occipital/parietal components demonstrate negative HRF peaks. Each show supra-threshold and significant F-statistics within the basal ganglia (Appendix A).

It is interesting to note the discrepancy between the canonical HRF and the HRF derived from attention network activity during RST (cl. $\{18; 20\}$, 9, 32 and 39) (Fig. 4.21b, Fig. 4.22 and Appendix A). These results suggest that the canonical HRF (i.e. the HRF without its temporal derivatives) is inadequate for capturing the relationship between those EEG patterns and BOLD-RST data within the attention network.

4.3.7 Relative power EEG-fMRI F-maps and IRFs

Although we have not investigated the relative power results in such details as absolute power results yet, we have made some observations suggesting that relative power overcomes the absolute power again. Since the table of relationships between EEG spatiospectral pattern timecourses and stimulus vectors demonstrate higher relationships for the relative power (Table 4.1) and since several spatiospectral patterns appear to be stable for both power types (Figs. 4.15 and 4.16), we have compared EEG-fMRI results for the pattern appearing for both power types with the highest evidence to the stimulus vectors (Fig. 4.24). On the first view, it could seems that both powers visualize the same large scale brain network involving sensory-motor cortices and basal ganglia working together. But relative power results are statistically stronger over almost all observations. The F-values are higher, the supra-threshold areas are larger (or the amount of supra-threshold voxels is higher), the evidence to the frequent stimulus is higher and supra-threshold after correction for multiple comparisons. The estimated impulse response functions between EEG and fMRI signals appear to be almost the same.

There are two other stable patterns (cl. n. 2 and 14) whose timecourses are significant to the frequent stimulus after family wise error correction ($p_{FWE} < 0.05$) and one cluster (cl. n. $\{30; 36\}$) supra-threshold without the correction ($p<0.05$;

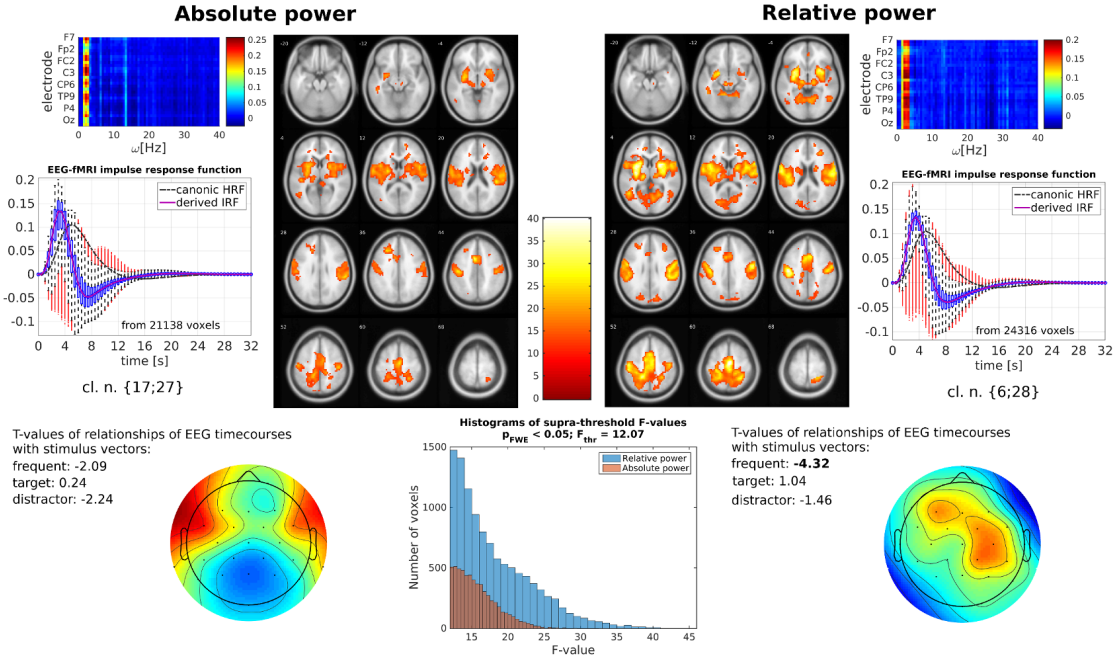

Fig. 4.24: Absolute versus relative EEG-fMRI results for the low θ-band spatiospectral pattern with the highest evidence to the task: VOT task, both EEG-fMRI maps threshold at $p_{FWE} < 0.05$, the colorbar between F-maps is the same for both F-maps.

Table 4.1). Their EEG-fMRI associations demonstrate much lower statistical significance than previous result and after the family wise error correction almost anything is supra-threshold.

Other three clusters (cl. n. $\{34; 39\}$, $\{8; 23\}$ and 24; Fig. 4.16) dispose with significant relationship to the target stimulus with p<0.05 uncorrected for multiple comparison errors (Table 4.1). Clusters n. $\{34; 39\}$ and $\{8; 23\}$ did not show any significant EEG-fMRI correlates at significance level $p_{FWE} < 0.05$. Oppositely, the cluster n. 24 demonstrate significant EEG-fMRI associations at significance level $p_{FWE} < 0.05$ in left-side lateralized sensory-motor networks (i.e. contralateral to right handed pushed button) and in left Putamen (Fig. 4.25).

Timecourses of the spatiospectral pattern of cluster n. 4 are significantly related to the sentence stimulus during the semantic decision task (Table 4.1 and Fig. 4.16). Although we have reported that our SDT EEG data are distorted with eye-blinking artifact and that it possibly decreases the strength of EEG-fMRI couplings, we are observing deactivations in Wenricke's areas (part of the speech cortex reliable for the speech understanding) after the α-band pattern (cl. n. 4) increase (Fig. 4.26). As you can see on the scalp topology, the decrease in α-band corresponds with Wenricke's area location.

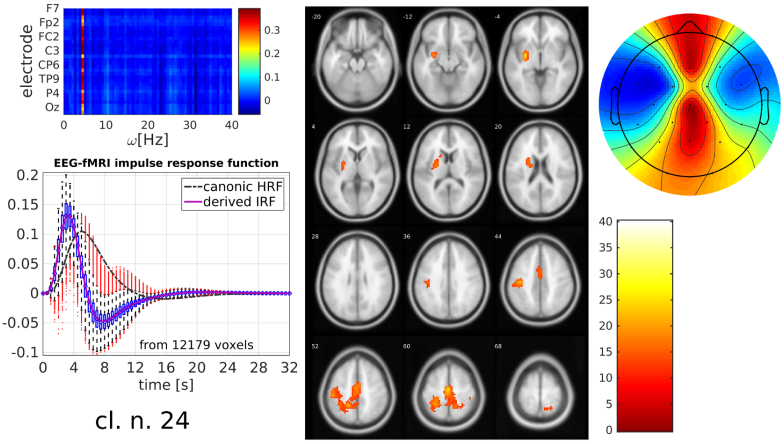

Fig. 4.25: EEG-fMRI results for the θ-band spatiospectral pattern related to the target stimulus: VOT task, EEG-fMRI F-map threshold at $p_{FWE} < 0.05$.

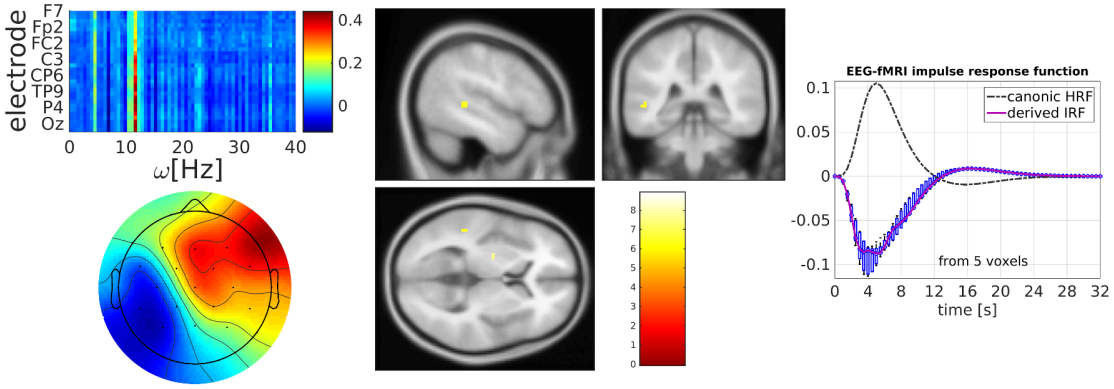

Fig. 4.26: EEG-fMRI results for the α-band spatiospectral pattern related to the semantic blocked sentence stimulus: SDT task, EEG-fMRI F-map threshold at $p < 0.001$ uncorrected for multiple comparison errors.

The rest of the relative power based EEG-fMRI results has not examined and investigated yet (i.e. results for other VOT and SDT stable components, and for all RST stable components). It is definitely a limit of the submitted thesis, but still we hope and believe that lots of novelties were presented within all shown results.

4.4 Discussion

4.4.1 Stable absolute EEG power spatiospectral patterns, their rhythms and topologies

EEG oscillations are often subdivided into distinct frequency bands which appear to represent distinct cognitive states (δ:0–4Hz, θ:4–8Hz, α:8–12Hz, β:12–20Hz and $\gamma > 20$ Hz) [26, 157]. Our results suggest that those bands can be further subdivided by frequency and electrode with data-driven group decomposition of independent spatiospectral patterns, and that these patterns are stable across experimental paradigms [120].

Using the current approach, (i.e. with a high model order), we demonstrate a more detailed parcellation of EEG sub-bands. The δ-band appears to have four independent spatiospectral components (clusters 2, 5, $\{3; 13\}$ and $\{17; 27\}$). The θ-band was divided into four stable independent mostly narrow-band clusters ($\{29; 38; 6\}$, $\{22; 33; 6\}$, 16; 37). The maximal α-band power was observed for three independent spatiospectral patterns (cl. 4, 30 and 32). The stable β-band components converged into two clusters (9 and 39), and broad-band components within the γ-band were only observed within cluster $\{1; 12\}$. The narrow-band components within the γ-band are likely non-neural in origin, potentially reflecting residual artifacts from the fMRI environment, as in Mareček et al. (2016) [120, 144].

The number components observed within each frequency band may depend on the model order (i.e. number of components) in ICA decomposition. For example, a given component may split into multiple components with a higher model order. The number of reliable components provides a useful metric for the appropriate choice of model order, since additional components are less reliably estimated when the model order is too high [136]. The model orders used within the present study appear appropriate, since cluster quality values are generally above 0.9, and were never below 0.7 (Fig. 4.3b, Fig. 4.4b and Fig. 4.5b) [120].

Although the subjects' groups partially overlapped for the SDT and RST datasets, the results in indicate that the spatiospectral patterns should be stable also over subjects. This conclusion is supported by three facts. First, the percentile of subjects belonging to the stable cluster is over 90% on average for all paradigms. Second, the VOT data involved totally disjunctive group of subjects from both other datasets. Third, the back-reconstruction of single-subject spatiospectral patterns brings inter-subject variability into the k-means clustering analysis, which reorganizes the variability back into relevant, convergent and compact clusters [120].

The δ-band oscillations appear to arise and be modulated by deep brain structures, and are associated with slow-wave sleep, and some pathologies [113]. We

identified two bilateral temporal sources in the present study with responses within these δ-band (Fig. 4.19a, cl. 2 and 5), suggesting they may be related to, or modulated by, activity within the allocortex structures.

Four θ-band spatiospectral patterns demonstrated prominent activity within bilateral frontal or fronto-temporal regions, with activity reduced around the midline (Fig. 4.19a, cl. $\{17; 27\}$, $\{29; 38; 6\}$, $\{22; 33; 19\}$ and 37). Previous experiments indicate that frontal θ-band oscillations modulate cognitive control [36], especially during working memory [69, 70, 76, 95, 102, 165, 181, 217]. These components likely contribute to these functions, although they demonstrate bilateral frontal topographic peaks, instead of the mid-central frontal peak typically observed.

Three independent spatiospectral patterns represent occipital and parieto-occipital responses within the α-band (Fig. 4.19a, cl. 4, 30 and 32). For two of the patterns (cl. 30 and 32), we found that decreases correspond to increases in frontal fMRI areas, supporting the association with α-band oscillations and active cognitive processes [110, 111].

The low β-band topologies appear inconsistent across datasets, despite the similarity in their peak frequency (Fig. 4.19a), while the high β-band topologies appear to have similar generators (i.e. are consistent across datasets) in right frontal areas (Fig. 4.19a). This finding indicates that β-band responses are present for each paradigm, but the spatial topography of low β-band components differs more across paradigms than the high β-band components.

4.4.2 Absolute power EEG-fMRI associations

Previous fMRI studies reported that different brain's areas organize into functionally distinct Large Scale Brain Networks (LSBNs) during the "resting-state" [1, 44, 204] and during tasks [32, 142, 192]. Comparison of fMRI LSBNs' dynamics (derived primarily using spatial group-ICA) with simultaneously acquired EEG shows that some networks (i.e. ventral attention, core and visual networks) correspond to event related potential (ERP) amplitudes [140, 142]. In addition, a subset of LSBNs correspond a subset of EEG power fluctuations [23, 81, 141, 143]. Although the voxel-wise analysis does not take into account information about LSBN structure, the supra-threshold maps often organize into these structures for a subset of spectral responses (e.g. the dorsal attention network associated with broad band EEG power [123, 127, 128], the default mode network [123, 128, 183], the speech network [144], the sensory-motor network [121, 123] and the visual network [123, 177]).

In the current study, the voxel-wise GLM between EEG spatiospectral patterns and BOLD signals revealed supra-threshold F-maps that overlap spatially with several LSBNs (e.g. sensory-motor, basal ganglia, visual, default mode, salience and

attention networks; Fig. 4.20, Fig. 4.21, Fig. 4.23, 4.22 and Appendix A). Although some similarities were observed over paradigms for some patterns, the most robust relationships between EEG and fMRI were observed during VOT. This finding may result due to the greater sample size within this dataset (21 subjects · 4 sessions · 256 scans) compared to the RST data (50 subjects · 300 scans) or SDT data (42 subjects · 230 scans). Alternatively, these findings are consisted with the robustness of VOT responses that have been observed within the fMRI and EEG literature, where responses to rare stimuli engage a series of brain networks specialized for detecting environmental irregularities.

Impulse response functions between EEG and fMRI-BOLD signals appear mostly to have similar shape as the canonical HRF with faster peak response than the canonical HRF (Fig. 4.20, Fig. 4.21, Fig. 4.23, 4.22 and Appendix A). EEG α-band responses often demonstrate negative relationships with fMRI, since increase in the α-band reflect neural disengagement (e.g. inhibition-timings hypothesis [111]) and a reduced metabolic state.

4.4.3 Stable relative EEG power spatiospectral patterns, their rhythms, topologies and relation to tasks

Although the stability of spatiospectral group-ICA estimates was lower than for the absolute power estimates (Figs. 4.3b-4.8b), the k-means clustering algorithm showed that relative EEG power also consists of linear combination of stable spatiospectral patterns. Same as for the absolute power patterns, the rhythms of the relative power patterns are sub-divided at frequency bands (Fig. 4.19b) consistent with previous observations [26]. The topologies are often similar over datasets and it seems that SDT patterns are not distorted by eye-blinking artifact in so big volume as happened for the absolute power patterns (Fig. 4.19).

The δ-band topologies are identical to absolute power δ-band topologies (Fig. 4.19). The midline θ-band topology [36, 165] is more observable in relative power topologies than in absolute power topologies. The topologies for other higher frequency bands start to be more divergent but still looking physiologically plausible.

As it was expected based on the literature review of previous studies [108, 110, 177, 187], we have confirmed for the novel relative EEG power spatiospectral patterns their higher evidence to the stimulus vectors than for the absolute power (Table 4.1, Fig. 4.18). Since the significance of the relationship to the external stimulation is higher for the relative power, it confirms the tested hypothesis that transformation between absolute and relative power is not a linear operation over time. And, it motivates the relative power as better predictor for blind visualizations of the task-

related brain networks from simultaneous EEG-fMRI data. This issue is described in more details in following sub-chapter.

4.4.4 Generalized EEG-fMRI spatiospectral heuristic model

We have decomposed relative power periodogram $\boldsymbol{D}(n_T, n_c * n_\omega)$ at m independent spatiospectral patterns $\boldsymbol{S}_m(n_c, n_w)$ and their time-courses $\boldsymbol{A}_m(n_T)$ (eq. 1.50) with Bridwell's et al. (2013) spatiospectral group-ICA [23]. As we have proposed on preliminary results [121], the matrices $\boldsymbol{S}_m$ can be considered as independent spatiospectral filters which solve our designed spatiospectral heuristic model (eq. 1.57). It can be solved with group-ICA because it then applies for independent functions g that $g(c, \omega) = \boldsymbol{S}_m$, and their time-courses $\boldsymbol{A}_m$ are then proportional to BOLD signal fluctuations.

Although we have not investigated all EEG-fMRI associations over all stable spatiospectral patterns, we are presenting on obtained results the indisputable proofs that the spatiospectral heuristic model visualize task-related networks better and with higher statistical significance than fluctuations of absolute power spatiospectral patterns (Fig. 4.24 and Fig. 4.25). Over the previous literature review [14, 45, 73, 75, 123, 121, 127, 128, 141, 144, 148, 153, 168, 177, 181, 183, 184, 187], we have noticed very limited count of studies presenting EEG-fMRI results with statistical significance after family wise error correction. From that point of view, we are presenting results on the current research border limit, since the whole self-organize large scale brain networks are significant and task-related (Fig. 4.24, Fig. 4.25 and Table 4.1).

Visual oddball data demonstrates large and significant BOLD activations after low wide-range θ-band pattern relative power increase in sensory-motor cortices and basal ganglia structures (containing both side putamen and brain stem areas) (Fig. 4.24). The functional connectivity between those two LSBNs is possibly frequent stimulus related (Table 4.1). After target appearance, the midline narrow θ-band pattern increase possibly change the connectivity in left putamen and left-lateralized sensory-motor network and BOLD signals are increasing only in this areas (Fig. 4.25 and Table 4.1). The lateralization corresponds with right hand held and pushed button after target stimulus. Based on neurologist expertise, the visualized networks are related and relevant to the visual oddball experiment.

Only one α-band pattern (cl. n. 4) was significantly related to the block-designed sentence stimulus during semantic decision task (Fig. 4.19b and Table 4.1). We have found BOLD activations in Wenricke's areas (with $p < 0.001$ uncorected) after the α-band pattern decrease observable on the scalp topology and on IRF timings (Fig 4.26). Functional role of Wenricke's area is understanding of the speech, other

words it is one of the primary centres which should be activated during the semantic task. The antagonistic behavior of the α-band pattern corresponds to the inhibition timing hypothesis [111] and to the other previous EEG-fMRI observations [46, 23]. Although the significance and the amount of surpa-threshold voxels are quite low, the generalized spatiospectral heuristic model is the only one approach which was able to find activations in speech areas in SDT data. Possibly, it is the most insensitive at the present eye-blinking artifact in EEG data.

In comparison with generalized spectral heuristic model results (*sub-chapter 3.3 "Results"*), we are obtaining higher significance of the results for the task-related networks. Here it can be double effect. The first effect is that we have better utilized the channel information within the EEG-fMRI data fusion. And, the second effect is that we have modelled spatial and time variable hemodynamic response functions.

In summary, our designed spatiospectral heuristic model appears to be relevant and reliable for task-related network visualizations from EEG-fMRI data and its following future research will be still necessary.

4.4.5 Novelty in spastiospectral decomposition of EEG signal and following EEG-fMRI fusion

To the best of our knowledge and knowledge of other scientists [89], the present doctoral thesis and publications related to the thesis are the first to demonstrate the stability of EEG independent spatiospectral patterns over different datasets. These findings further validate the approach for future studies, and motivate investigation of the functional role of the distinct spatiospectral patterns. Subdividing spectral responses in a data driven manner will be useful for future studies that decompose separate signals with potentially distinct functional roles (i.e. generating more robust results) and separating signals from artifact (i.e. enhancing signal over noise) [120].

This is the first study examining EEG-fMRI correlates after group-derived EEG spatiospectral decomposition over different experimental datasets. The voxel-wise EEG-fMRI approach revealed F-statistic fMRI overlays whose supra-threshold voxels organized into functional large scale brain networks (LSBNs) consistent with previous literature. In addition, we have modeled spatially variable group-averaged HRFs often with shorter latency peaks than the canonical HRF (Fig. 4.20, Fig. 4.21, Fig. 4.23, 4.22 and Appendix A).

We have designed the generalized EEG-fMRI spatiospectral heuristic model and proposed how to solve the model with the spatiospectral group-ICA method [121]. Since the model demonstrates the most significant task-related EEG-fMRI associations over the range of tested approaches (i.e. absolute power fluctuations, gen-

eralized spectral heuristic model, fluctuations of absolute power spatiospectral patterns), its application can be expected in future research of blind visualizations of task-related networks directly from simultaneous EEG-fMRI data. Obtained statistical significance of EEG-fMRI results for the VOT task-related networks is one of the highest which can be observed over literature nowadays.

4.4.6 Limits and possible future research

The stability of spatiospectral patterns may be useful for brain computer interface (BCI) research [212], since EEG spatiospectral filters are often applied as an approach to denoise the data [6, 48, 132, 147, 160, 202, 216]. The approach may also be useful in clinical research and applications focused on spectral differences between populations within distinct frequency bands, e.g. as demonstrated for Alzheimer's [103, 176] or Parkinson's [109, 191] diseases. Since the relative EEG power demonstrates the stable patterns too, the spatiospectral Group-ICA may also be useful for examining the relative power differences prominent in autism [120, 210].

Future research could compare the consistency of group results derived using other approaches that generate EEG spatiospectral patterns, such as group-clustering after single-subject ICA [91, 93], approximate joint diagonalization of lagged-covariance [200] or cospectral matrices [42, 43, 120].

The inability to detect stable γ-band patterns from absolute EEG power limits the current study, fortunately the patterns are observable in relative EEG power.

Only amplitudes of frequency powers were taken into account, the incorporation of the signal phases into the spatiospectral decomposition [94, 215] could potentially brings benefits.

Although eye-blinking artifacts in absolute EEG power were previously observed only for cl. n. 17;27 of the SDT dataset (Fig. 4.14), it seems that the artifact may be minimal, but present, within 11 of the 14 absolute power components, since topology maps demonstrate peak responses over frontal regions (Fig. 4.19a). This suggests that eye-blinking artifacts may not separate into a single component within spatiospectral group-ICA of absolute EEG power implemented in GIFT. This may result due to the variability of eye blink artifacts across subjects, motivating individual subject eye-blink artifact removal (e.g. with temporal ICA prior to spatiospectral Group-ICA).

The different sample sizes within the different tasks potentially limit the present study. Lower sample sizes within the RST and SDT tasks could have contributed to greater variability in the statistical estimates, potentially explaining the more robust EEG-fMRI associations observed within the VOT paradigm.

Not fully explored space of EEG-fMRI results for spatiospectral heuristic model limits the actual study. Although we have presented that the generalized spatiospectral heuristic model provides the strongest EEG-fMRI task-related correlates, we have not tested inter-subject variability in EEG-fMRI results over any used and tested approach. Still, it is very interesting, actual and opened question in EEG-fMRI data fusion research [75, 81, 143, 148] and should be investigated furthermore.

4.5 Conclusion

As the first in the world, we have shown and published that spatiospectral group-ICA of EEG spectra estimates stable independent spatiospectral patterns over datasets and possibly also over subjects. That applies for both power types (i.e. absolute and relative powers). Obtained higher statistical significance for EEG-fMRI results with EEG spatiospectral F-maps proves that better incorporation of the channels together with modelled spatially and timely variable hemodynamic response improved the method of the data fusion. Our designed generalized spatiospectral heuristic model dispose with the highest evidence in task-related network visualizations and it could possibly become to be used in future simultaneous EEG-fMRI data fusion research. The inter-subject variability of significant obtained results were not investigated within the current thesis and it should be done within the near future research.

5 PH.D. THESIS OUTCOMES AND CONCLUSIONS

We have set seven partial goals necessary for the successful defense of the current doctoral thesis. For remembering, they are repeated in following paragraph:

1. Select the EEG signal processing strategy which is usable for the blind search analysis.
2. Design the models for the data fusion which could work better than current state of the art.
3. Design the evaluation and evaluate the correspondence of obtained results with experimental external stimulation.
4. On available real simultaneous EEG-fMRI data, estimate the fusion with designed models, with previously implemented methods and compare the results over the different approaches.
5. Evaluate the designed models and their new contributions to the current knowledge.
6. Present the obtained results in neuroscience or biomedical engineering journals with impact factor as two original research papers (at minimum).
7. Share the implemented software libraries as the doctoral thesis attachment.

Ad. 1.: Because the goal was to visualize task-related brain networks without information about the stimulus timings inside the EEG-fMRI fusion, we have selected the EEG processing via power spectral changes instead of the event related potentials, where timings of the trial beginnings are necessary.

Ad. 2.: The literature review uncovered that the most of EEG-fMRI data fusion processes use absolute EEG power fluctuations which are compared with delayed fMRI-BOLD signals. The usage of the relative EEG power fluctuations in distinct frequency bands were not commonly used, although Klimesch 1999 and Kilner et al. (2005) [108, 110] claim it corresponds more with evoked neuronal activity. Kilner et al. (2005) proposed and Rosa et al. (2010) simplified the classic heuristic approach (eq. 1.54 or 5.1) [108, 177] which expects same global changes over whole relative power frequency range after evoked neural activity, although e.g. inhibition hypothesis was tested and confirmed for the α-band pattern [111] (i.e. it behaves antagonistic to the other frequency bands). To overcome this limit, we have designed generalized spectral heuristic model (eq. 1.56 or 5.2), which we are testing within the current doctoral thesis. The generalized spectral heuristic model has still limit in utilizing unique informations from different EEG leads, as evaluated in 3^{rd}

chapter of the current thesis. To overcome this issue, we have proposed generalized spatiospectral heuristic model (eq. 1.57 or 5.3) and designed how to solve it with spatiospectral group-ICA. Since the group-ICA belongs to the family of blind source separation algorithms and stability of its estimates over different runs/datasets/etc. is still speculative, we have used existing k-means clustering algorithm and as estimated the stability of the EEG spatiospectral sources over different datasets and subjects. Following EEG-fMRI associations were then evaluated and tested only for the stable spatiospectral patterns. For the EEG-fMRI data fusion, general linear model was used for both proposed and tested models. The BOLD signal delay in EEG power fluctuations was modelled as fixed canonical hemodynamic response function for the generalized spectral heuristic model, and as spatially and temporally variable hemodynamic response function for the generalized spatiospectral heuristic model.

$$\tilde{b} \propto \sqrt{\int \omega^2 \tilde{p}(\omega) d\omega} \tag{5.1}$$

$$\tilde{b} \propto \sqrt{\int g(\omega) \tilde{p}(\omega) d\omega} \tag{5.2}$$

$$\tilde{b} \propto \sqrt{\int \int g(c,\omega) \tilde{p}(c,\omega) dc d\omega} \tag{5.3}$$

Ad. 3.: To evaluate the correspondence with external stimulation, general linear model between EEG power fluctuations and stimulus vectors was implemented with following group one-sample t-tests. The stimulus vectors were regressors and EEG power fluctuations were the measured data.

Ad. 4.: We have implemented the EEG-fMRI fusion for the original absolute power fluctuations, classic heuristic model, generalized spectral heuristic model, time-courses of stable absolute power spatiospectral patterns and stable patterns of generalized spatiospectral heuristic model. Simultaneous EEG-fMRI data were acquired for visual oddball, semantic decision and resting-state experiments, and were more or less used for the evaluation of differences over different fusion approaches.

Ad. 5.: It was shown that both proposed models (i.e. generalized spectral and spatiospectral heuristic models) visualize task-related networks from EEG-fMRI data better than previous available approaches. The spectral model did not ignore the α-band inhibition properties of the EEG signal. And the spatiospectral model utilized better the information about different sources over different leads. The spatiospectral heuristic model disposed with highest statistical significance of the task-related results for visual oddball data. For semantic decision data, it was the only one approach which was able to show supra-threshold activated voxels in

speech areas, although the semantic decision EEG data were distorted with eye-blinking artifact. Beyond the original objectives, we have found that EEG absolute and relative power spatiospectral patterns are stable over different paradigms and subjects, and that the stability is much higher than other concurrent actually used ICA decompositions of EEG signal.

Ad. 6.: First, we have presented in *Journal of Neuroscience Methods* that relative EEG power in distinct frequency bands (i.e. the generalized spectral heuristic model) is better for visualizations of task-related brain networks than originally commonly used absolute power [123]. Then we have proposed generalized spectral and spatiospectral heuristic models with a preliminary results on 13^{th} *International Symposium on Biomedical Imaging: From Nano to Macro* [121]. During the testing of the spatiospectral group-ICA as the method for EEG signal processing into the form comparable with BOLD signals, we have noticed that the estimates are stable and similar over different paradigms for both power types (i.e. absolute and relative). For the absolute power, we have reported this acquired knowledge in *Brain Topography* journal within the special issue *Multisubject Decomposition of EEG — Methods and Applications* [120]. For the relative power, we have submitted the obtained results as conference proceedings on *World Congress on Medical Physics & Biomedical Engineering* [119]. The proceedings is under review now. The EEG-fMRI results for the stable absolute power spatiospectral sources are summarized within prepared manuscript *"EEG spatiospectral patterns and their link to fMRI BOLD signal via variable hemodynamic response functions"* which will be submitted into a journal in several following weeks. Since we have got the most significant EEG-fMRI task-related networks for the generalized spatiospectral heuristic model, we are expecting that this result could be written as an other manuscript and submitted to a journal. Except these published or prepared or planned papers related to the current doctoral thesis, I was helpful during testing the stability of EEG-fMRI fusion after EEG signal PARAFAC decomposition (parallel factor analysis). The PARAFAC results were presented in *Neural Computation* journal [143].

Ad. 7.: The list of attached functions is given within appendices *B*.

BIBLIOGRAPHY

[1] Elena A Allen, Erik B Erhardt, Eswar Damaraju, William Gruner, Judith M Segall, Rogers F Silva, Martin Havlicek, Srinivas Rachakonda, Jill Fries, Ravi Kalyanam, Andrew M Michael, Arvind Caprihan, Jessica a Turner, Tom Eichele, Steven Adelsheim, Angela D Bryan, Juan Bustillo, Vincent P Clark, Sarah W Feldstein Ewing, Francesca Filbey, Corey C Ford, Kent Hutchison, Rex E Jung, Kent A Kiehl, Piyadasa Kodituwakku, Yuko M Komesu, Andrew R Mayer, Godfrey D Pearlson, John P Phillips, Joseph R Sadek, Michael Stevens, Ursina Teuscher, Robert J Thoma, and Vince D Calhoun. *A baseline for the multivariate comparison of resting-state networks.* Frontiers in systems neuroscience, 5(February):2, 2011.

[2] Elena A Allen, Erik B Erhardt, Yonghua Wei, Tom Eichele, and Vince D Calhoun. *Capturing inter-subject variability with group independent component analysis of fMRI data: a simulation study.* NeuroImage, 59(4):4141–4159, 2012.

[3] P J Allen, O Josephs, and R Turner. *A method for removing imaging artifact from continuous EEG recorded during functional MRI.* NeuroImage, 12(2):230–9, aug 2000.

[4] P J Allen, G Polizzi, K Krakow, D R Fish, and L Lemieux. *Identification of EEG events in the MR scanner: the problem of pulse artifact and a method for its subtraction.* NeuroImage, 8(3):229–239, 1998.

[5] Jörn Anemüller, Terrence J. Sejnowski, and Scott Makeig. *Complex independent component analysis of frequency-domain electroencephalographic data.* Neural Networks, 16(9):1311–1323, 2003.

[6] Kai Keng Ang, Zheng Yang Chin, Haihong Zhang, and Cuntai Guan. *Filter Bank Common Spatial Pattern (FBCSP) in Brain-Computer Interface.* International Joint Conference on Neural Networks (IJCNN), (July 2016):2390–2397, 2008. Available from: `http://ieeexplore.ieee.org/xpls/abs{_}all.jsp?arnumber=4634130{%}5Cnhttp://ieeexplore.ieee.org/lpdocs/epic03/wrapper.htm?arnumber=4634130`.

[7] S. Baron-Cohen, S. Baron-Cohen, H. A Ring, H. A Ring, S Wheelright, S Wheelright, E. T Bullmore, E. T Bullmore, M. J Brammer, M. J Brammer, Andrea M Simmons, Andrea M Simmons, S C Williams,

and S C Williams. *Social intelligence in the normal and autisitic brain: an fMRI study.* *European Journal of Neuroscience*, 11(6):1891–1898, 1999.

[8] P J Basser, J Mattiello, and D LeBihan. *MR diffusion tensor spectroscopy and imaging.* *Biophysical journal*, 66(1):259–67, jan 1994.

[9] Beckmann, Mackay, Filippini, and Smith. *Group comparison of resting-state FMRI data using multi-subject ICA and dual regression.* *NeuroImage*, 47(Suppl 1):S148, 2009.

[10] C F Beckmann and S M Smith. *Tensorial extensions of independent component analysis for multisubject FMRI analysis.* *NeuroImage*, 25(1):294–311, 2005.

[11] Christian F Beckmann and Stephen M Smith. *Probabilistic independent component analysis for functional magnetic resonance imaging.* *IEEE transactions on medical imaging*, 23(2):137–152, 2004.

[12] A J Bell and T J Sejnowski. *An information-maximization approach to blind separation and blind deconvolution.* *Neural computation*, 7(6):1129–1159, nov 1995.

[13] A. Belouchrani, K. Abed-Meraim, J.F. Cardoso, and E. Moulines. *A blind source separation technique using second-order statistics.* *IEEE Transactions on Signal Processing*, 45(2):434–444, 1997.

[14] Christian-G Bénar, Daniele Schön, Stephan Grimault, Bruno Nazarian, Boris Burle, Muriel Roth, Jean-Michel Badier, Patrick Marquis, Catherine Liegeois-Chauvel, and Jean-Luc Anton. *Single-trial analysis of oddball event-related potentials in simultaneous EEG-fMRI.* *Human brain mapping*, 28(7):602–613, 2007.

[15] Edward M. Bernat, William J. Williams, and William J. Gehring. *Decomposing ERP time-frequency energy using PCA.* *Clinical Neurophysiology*, 116(6):1314–1334, 2005.

[16] Ella Bingham and Aapo Hyvärinen. *a Fast Fixed-Point Algorithm for Independent Component Analysis of Complex Valued Signals.* *International Journal of Neural Systems*, 10(01):1–8, 2000.

[17] F Bloch. *Nuclear induction.* *Physical Review*, 70(7-8):460–474, 1946.

[18] Roland N Boubela, Klaudius Kalcher, Wolfgang Huf, Claudia Kronnerwetter, Peter Filzmoser, and Ewald Moser. *Beyond Noise: Using*

Temporal ICA to Extract Meaningful Information from High-Frequency fMRI Signal Fluctuations during Rest. Frontiers in human neuroscience, 7:168, 2013.

[19] Milan Brázdil, Michal Mikl, Radek Mareček, Petr Krupa, and Ivan Rektor. *Effective connectivity in target stimulus processing: a dynamic causal modeling study of visual oddball task.* NeuroImage, 35(2):827–835, 2007.

[20] David A. Bridwell and Vince Calhoun. *Fusing Concurrent EEG and fMRI intrinsic networks.* In Magnetoencephalography, pages 213–235. Springer, Berlin Heidelberg, 2014.

[21] David A. Bridwell, Srinivas Rachakonda, Rogers F. Silva, Godfrey D. Pearlson, and Vince D. Calhoun. *Spatiospectral Decomposition of Multi-subject EEG: Evaluating Blind Source Separation Algorithms on Real and Realistic Simulated Data.* Brain Topography, 31(1):47–61, 2018.

[22] David A. Bridwell, Vaughn R. Steele, J. Michael Maurer, Kent A. Kiehl, and Vince D. Calhoun. *The relationship between somatic and cognitive-affective depression symptoms and error-related ERPs.* Journal of Affective Disorders, 172:89–95, 2015.

[23] David A Bridwell, Lei Wu, Tom Eichele, and Vince D Calhoun. *The spatiospectral characterization of brain networks: fusing concurrent EEG spectra and fMRI maps.* NeuroImage, 69:101–11, apr 2013.

[24] Rasmus Bro. *Multi-way analysis in the food industry: models, algorithms, and applications.* PhD thesis, Univerity of Amsterdam, 1998.

[25] R B Buxton, E C Wong, and L R Frank. *Dynamics of blood flow and oxygenation changes during brain activation: the balloon model.* Magnetic Resonance in Medicine, 39(6):855–64, jun 1998.

[26] Gregory Buzsaki. *Rhythms of the Brain.* Oxford University Press, 2006.

[27] V. Calhoun, G. Pearlson, and T. Adali. *Independent Component Analysis Applied to fMRI Data: A Generative Model for Validating Results.* The Journal of VLSI Signal Processing, 37(2):281–291, 2004.

[28] V D Calhoun, T Adali, V B McGinty, J J Pekar, T D Watson, and G D Pearlson. *fMRI activation in a visual-perception task: network of areas detected using the general linear model and independent components analysis.* NeuroImage, 14(5):1080–1088, 2001.

[29] V D Calhoun, T Adali, G D Pearlson, and J J Pekar. *A Method for Making Group Inferences from Functional MRI Data Using Independent Component Analysis.* Human brain mapping, 14:140–151, 2001.

[30] V D Calhoun, T Adali, G D Pearlson, and J J Pekar. *Spatial and temporal independent component analysis of functional MRI data containing a pair of task-related waveforms.* Human brain mapping, 13(1):43–53, may 2001.

[31] Vince D Calhoun and Tülay Adali. *Multisubject independent component analysis of fMRI: a decade of intrinsic networks, default mode, and neurodiagnostic discovery.* IEEE reviews in biomedical engineering, 5:60–73, 2012.

[32] Vince D Calhoun, Kent A Kiehl, and Godfrey D Pearlson. *Modulation of temporally coherent brain networks estimated using ICA at rest and during cognitive tasks.* Human brain mapping, 29(7):828–838, 2008.

[33] Vince D Calhoun, Jingyu Liu, and Tülay Adali. *A review of group ICA for fMRI data and ICA for joint inference of imaging, genetic, and ERP data.* NeuroImage, 45(1 Suppl):S163—-72, 2009.

[34] Vince D Calhoun, James J Pekar, and Godfrey D Pearlson. *Alcohol intoxication effects on simulated driving: exploring alcohol-dose effects on brain activation using functional MRI.* Neuropsychopharmacology, 29(11):2097–2107, 2004.

[35] Jean-francois Cardoso and Antoine Souloumiac. *Blind beamforming for non gaussian signals.* In IEE Proceedings F (Radar and Signal Processing), volume 140, pages 362–370, 1993.

[36] James F Cavanagh and Michael J Frank. *Frontal theta as a mechanism for cognitive control.* Trends in Cognitive Sciences, 18(8):414–421, 2014.

[37] Joseph E Cavanaugh. *A large-sample model selection criterion based on Kullback's symmetric divergence.* Statistics & Probability Letters, 42(4):333–343, 1999.

[38] Leon Cohen. *Time-Frequency Distributions — A Review.* Proceedings of the IEEE, 77(7):941–981, 1989.

[39] Leon Cohen. *Time-frequency analysis.* NJ:: Prentice Hall PTR, Englewood Cliffs, 1995.

[40] Pierre Comon. *Independent component analysis, A new concept?* Signal Processing, 36(3):287–314, apr 1994.

[41] Fengyu Cong, Zhaoshui He, Jarmo Hämäläinen, Paavo H T Leppänen, Heikki Lyytinen, Andrzej Cichocki, and Tapani Ristaniemi. *Validating rationale of group-level component analysis based on estimating number of sources in EEG through model order selection.* Journal of Neuroscience Methods, 212(1):165–172, 2013.

[42] Marco Congedo, Cédric Gouy-Pailler, and Christian Jutten. *On the blind source separation of human electroencephalogram by approximate joint diagonalization of second order statistics.* Clinical Neurophysiology, 119(12):2677–2686, 2008.

[43] Marco Congedo, Roy E. John, Dirk De Ridder, and Leslie Prichep. *Group independent component analysis of resting state EEG in large normative samples.* International Journal of Psychophysiology, 78(2):89–99, 2010.

[44] J S Damoiseaux, S A R B Rombouts, F Barkhof, P Scheltens, C J Stam, S M Smith, and C F Beckmann. *Consistent resting-state networks across healthy subjects.* Proceedings of the National Academy of Sciences of the United States of America, 103(37):13848–53, 2006.

[45] J C de Munck, S I Gonçalves, R Mammoliti, R M Heethaar, and F H Lopes da Silva. *Interactions between different EEG frequency bands and their effect on alpha-fMRI correlations.* NeuroImage, 47(1):69–76, aug 2009.

[46] J.C. C de Munck, S.I. I Gonçalves, L. Huijboom, J.P.A. P A Kuijer, P.J.W. J W Pouwels, R.M. M Heethaar, and F.H. H Lopes da Silva. *The hemodynamic response of the alpha rhythm: An EEG/fMRI study.* NeuroImage, 35(3):1142–1151, 2007.

[47] Arnaud Delorme, Terrence Sejnowski, and Scott Makeig. *Enhanced detection of artifacts in EEG data using higher-order statistics and independent component analysis.* NeuroImage, 34(4):1443–1449, 2007.

[48] Guido Dornhege, Benjamin Blankertz, Matthias Krauledat, Florian Losch, Gabriel Curio, and Klaus Robert Müller. *Combined optimization of spatial and temporal filters for improving brain-computer interfacing.* IEEE Transactions on Biomedical Engineering, 53(11):2274–2281, 2006.

[49] Norman Richard Draper, Harry Smith, and Elizabeth Pownell. *Applied regression analysis.* Wiley, New York, 3rd edition, 1966.

[50] Tom Eichele, Vince D Calhoun, and Stefan Debener. *Mining EEG-fMRI using independent component analysis.* International journal of psychophysiology, 73(1):53–61, 2009.

[51] Tom Eichele, Vince D Calhoun, Matthias Moosmann, Karsten Specht, Marijtje L a Jongsma, Rodrigo Quian Quiroga, Helge Nordby, and Kenneth Hugdahl. *Unmixing concurrent EEG-fMRI with parallel independent component analysis.* International journal of psychophysiology, 67(3):222–234, 2008.

[52] Tom Eichele, Srinivas Rachakonda, Brage Brakedal, Rune Eikeland, and Vince D. Calhoun. *EEGIFT: Group independent component analysis for event-related EEG data.* Computational Intelligence and Neuroscience, 2011, 2011.

[53] James William Emsley, James Feeney, and Leslie Howard Sutcliffe. *High resolution nuclear magnetic resonance spectroscopy.* Elsevier, 2013.

[54] Stephen A. Engel, David E. Rumelhart, Brian A. Wandell, Adrian T. Lee, Gary H. Glover, Eduardo-Jose Chichilnisky, and Michael N. Shadlen. *fMRI of human visual cortex.* Nature, 369:525, 1994.

[55] Erik Barry Erhardt, Srinivas Rachakonda, Edward J Bedrick, Elena a Allen, Tülay Adali, and Vince D Calhoun. *Comparison of multi-subject ICA methods for analysis of fMRI data.* Human brain mapping, 32(12):2075–2095, 2011.

[56] Fabrizio Esposito, Tommaso Scarabino, Aapo Hyvarinen, Johan Himberg, Elia Formisano, Silvia Comani, Gioacchino Tedeschi, Rainer Goebel, Erich Seifritz, and Francesco Di Salle. *Independent component analysis of fMRI group studies by self-organizing clustering.* NeuroImage, 25(1):193–205, 2005.

[57] Zainab Fatima, Maher A. Quraan, Natasa Kovacevic, and Anthony Randal McIntosh. *ICA-based artifact correction improves spatial localization of adaptive spatial filters in MEG.* NeuroImage, 78:284–294, 2013.

[58] D Flannigan, G Bradley, John R Bentson, B Luf, and Grant B Hieshima. *Magnetic Resonance Imaging Brainstem: Normal Structure Basic Functional Anatomy.* Neuroradiology, 154(2):375–383, 1985.

[59] K J Friston. *Bayesian estimation of dynamical systems: an application to fMRI.* NeuroImage, 16(2):513–30, jun 2002.

[60] K J Friston, J Ashburner, C D Frith, J Poline, J D Heather, and R S J Frackowiak. *Spatial Registration and Normalization of Images.* *Human brain mapping*, 3(3):165–189, 1995.

[61] K J Friston, P Fletcher, O Josephs, A Holmes, M D Rugg, and R Turner. *Event-related fMRI: characterizing differential responses.* *NeuroImage*, 7(1):30–40, 1998.

[62] K. J. Friston, A. P. Holmes, K. J. Worsley, J.-P. Poline, C. D. Frith, and R. S. J. Frackowiak. *Statistical Parametric Maps in Functional Imaging: A General Linear Approach.* *Human brain mapping*, 2(4):189–210, 1994.

[63] K J Friston, P Jezzard, and R Turner. *Analysis of Functional MRI Time-Series.* *Human Brain Mapping*, 171:153–171, 1994.

[64] K J Friston, A Mechelli, R Turner, and C J Price. *Nonlinear responses in fMRI: the Balloon model, Volterra kernels, and other hemodynamics.* *NeuroImage*, 12(4):466–77, oct 2000.

[65] K J Friston, W Penny, C Phillips, S Kiebel, G Hinton, and J Ashburner. *Classical and Bayesian inference in neuroimaging: theory.* *NeuroImage*, 16(2):465–83, jun 2002.

[66] Karl J Friston, Joshua Kahan, Bharat Biswal, and Adeel Razi. *A DCM for resting state fMRI.* *NeuroImage*, dec 2013.

[67] K.J. Karl J Friston, Lee Harrison, and Will Penny. *Dynamic causal modelling.* *NeuroImage*, 19(4):1273–1302, aug 2003.

[68] A. Gartus, T. Foki, A. Geissler, and Roland Beisteiner. *Improvement of clinical language localization with an overt semantic and syntactic language functional MR imaging paradigm.* *American Journal of Neuroradiology*, 30(10):1977–1985, 2009.

[69] A.S. Gevins, G.M. Zeitlin, J.C. Doyle, R.E. Schaffer, and E. Callaway. *EEG Patterns during 'cognitive' taks. II. Analysis of controlled taks.* *Electroencephalography and Clinical Neurophysiology*, 47:704–710, 1979.

[70] A.S. Gevins, G.M. Zeitlin, C.D. Yingling, J.C. Doyle, M.F. Dedon, R.E. Schaffer, J.T. Roumasset, and C.L. Yeager. *EEG Patterns during 'cognitive' taks. I. Methodology and analysis of complex behaviours.* *Electroencephalography and Clinical Neurophysiology*, 47:693–703, 1979.

[71] Rainer Goebel, Alard Roebroeck, Dae Shik Kim, and Elia Formisano. *Investigating directed cortical interactions in time-resolved fMRI data using vector autoregressive modeling and Granger causality mapping.* Magnetic Resonance Imaging, 21(10):1251–1261, 2003.

[72] Robin I. Goldman, John M. Stern, Jerome Engel, and Mark S. Cohen. *Acquiring simultaneous EEG and functional MRI.* Clinical Neurophysiology, 111(11):1974–1980, 2000.

[73] Robin I Goldman, John M. Stern, Jerome Jr Engel, and Mark S. Cohen. *Simultaneous EEG and fMRI of alpha rhythm.* Neuroreport, 13(18):2487–2492, 2002.

[74] Gene H Golub, Per Christian Hansen, and Dianne P O'Leary. *Tikhonov Regularization and Total Least Squares.* SIAM Journal on Matrix Analysis and Applications, 21(1):185–194, 1999.

[75] S I Gonçalves, J C de Munck, P J W Pouwels, R Schoonhoven, J P a Kuijer, N M Maurits, J M Hoogduin, E J W Van Someren, R M Heethaar, and F H Lopes da Silva. *Correlating the alpha rhythm to BOLD using simultaneous EEG/fMRI: inter-subject variability.* NeuroImage, 30(1):203–213, 2006.

[76] Alexander Gundel and Glenn F Wilson. *Topographical Changes in the Ongoing EEG Related to the Difficulty of Mental Tasks.* Brain topography, 5(1):17–25, 1992.

[77] Martin Havlicek, Jiri Jan, Milan Brazdil, and Vince D Calhoun. *Dynamic Granger causality based on Kalman filter for evaluation of functional network connectivity in fMRI data.* NeuroImage, 53(1):65–77, 2010.

[78] Martin Havlíček and Jiří Jan. *Exploring brain network connectivity through hemodynamic modeling.* PhD thesis, Brno University of Technology, 2011.

[79] Johan Himberg and Aapo Hyvärinen. *Icasso: software for investigating the reliability of ICA estimates by clustering and visualization.* In 13th Workshop on Neural Networks for Signal Processing, pages 259–268. IEEE, 2003.

[80] Johan Himberg, Aapo Hyvärinen, and Fabrizio Esposito. *Validating the independent components of neuroimaging time series via clustering and visualization.* NeuroImage, 22(3):1214–1222, 2004.

[81] Jaroslav Hlinka, Charilaos Alexakis, Ana Diukova, Peter F. Liddle, and Dorothee P. Auer. *Slow EEG pattern predicts reduced intrinsic functional connectivity in the default mode network: An inter-subject analysis.* NeuroImage, 53(1):239–246, 2010.

[82] A Hoffmann, L Jäger, K J Werhahn, M Jaschke, S Noachtar, and M Reiser. *Electroencephalography during functional echo-planar imaging: detection of epileptic spikes using post-processing methods.* Magnetic Resonance in Medicine, 44(5):791–8, 2000.

[83] L. Hu, A. Mouraux, Y. Hu, and G. D. Iannetti. *A novel approach for enhancing the signal-to-noise ratio and detecting automatically event-related potentials (ERPs) in single trials.* NeuroImage, 50(1):99–111, 2010.

[84] L. Hu, Z. G. Zhang, A. Mouraux, and G. D. Iannetti. *Multiple linear regression to estimate time-frequency electrophysiological responses in single trials.* NeuroImage, 111:442–453, 2015.

[85] Frank R. Huang-Hellinger, Hans C. Breiter, Glen McCormack, Mark S. Cohen, Ken K. Kwong, Jeffrey P. Sutton, Robert L. Savoy, Robert M. Weisskoff, Timothly L. Davis, John R. Baker, John W. Belliveau, and Bruce R. Rosen. *Simultaneous functional magnetic resonance imaging and electrophysiological recording.* Human Brain Mapping, 3(1):13–23, 1995.

[86] Scott A Huettel, Allen W Song, and Gregory McCarthy. *Functional Magnetic Resonance Imaging.* Sinauer Associates, Inc, Sunderland, 2nd edition, 2009.

[87] Rene J Huster, Sergey M Plis, and Vince D Calhoun. *Group-level component analyses of EEG: validation and evaluation.* Frontiers in neuroscience, 9(July):254, 2015.

[88] René J. Huster and Liisa Raud. *A Tutorial Review on Multi-subject Decomposition of EEG.* Brain Topography, 31(1):3–16, 2018.

[89] R.J. Huster and V.D. Calhoun. *Progress in EEG: Multi-subject Decomposition and Other Advanced Signal Processing Approaches.* Brain Topography, 31(1):1–2, 2018.

[90] A. Hyvärinen. *The Fixed-Point Algorithm and Maximum Likelihood Estimation for Independent Component Analysis.* Neural Processing Letters, 10(1):1–5, 1999.

[91] Aapo Hyvärinen. *Testing the ICA mixing matrix based on inter-subject or inter-session consistency.* NeuroImage, 58(1):122–136, 2011.

[92] Aapo Hyvärinen, Juha Karhunen, and Erkki Oja. *Independent component analysis.* John Wiley & Sons, New York, 2001.

[93] Aapo Hyvärinen and Pavan Ramkumar. *Testing independent component patterns by inter-subject or inter-session consistency.* Frontiers in human neuroscience, 7(March 2013):94, 2013.

[94] Aapo Hyvärinen, Pavan Ramkumar, Lauri Parkkonen, and Riitta Hari. *Independent component analysis of short-time Fourier transforms for spontaneous EEG/MEG analysis.* NeuroImage, 49(1):257–271, 2010.

[95] T. Ishihara and N. Yoshii. *Multivariate analytic study of EEG and mental activity in juvenile delinquents.* Electroencephalography and Clinical Neurophysiology, 33:71–80, 1972.

[96] J. R. Ives, S. Warach, F. Schmitt, R. R. Edelman, and D. L. Schomer. *Monitoring the patient's EEG during echo planar MRI.* Electroencephalography and Clinical Neurophysiology, 87(6):417–420, 1993.

[97] Julia Jacobs, Pierre LeVan, Friederike Moeller, Rainer Boor, Ulrich Stephani, Jean Gotman, and Michael Siniatchkin. *Hemodynamic changes preceding the interictal EEG spike in patients with focal epilepsy investigated using simultaneous EEG-fMRI.* NeuroImage, 45(4):1220–1231, 2009.

[98] Jiří Jan. *Digital Signal Filtering, Analysis and Restoration.* The Institution of Electrical Engineers, London, 1st edition, 2000.

[99] Jiří Jan. *Medical Image Processing, Reconstruction and Restoration: concepts and methods.* Taylor & Francis Group, Boca Raton, 2006.

[100] David Janeček. *Sdružená EEG-fMRI analýza na základě heuristického modelu.* In Master Thesis, pages 1–88. Brno University of Technology, Supervised by René Labounek, 2015.

[101] David Janeček and René Labounek. *Heuristic model in joint EEG-fMRI analysis.* In Proceedings of the 21st Conference STUDENT EEICT 2015, pages 209–211, Brno, 2015.

[102] Ole Jensen and Claudia D Tesche. *Frontal theta activity in humans increases with memory load in a working memory task.* European Journal of Neuroscience, 15(8):1395–1399, 2002.

[103] Jeong-Won Jeong, Tae-Seong Kim, Sung-Heon Kim, and Manbir Singh. *Application of independent component analysis with mixture density model to localize brain alpha activity in fMRI and EEG.* International Journal of Imaging Systems and Technology, 14(4):170–180, 2004.

[104] Ian Jolliffe. *Principal component analysis.* John Wiley & Sons, Ltd, 2002.

[105] Carrie A. Joyce, Irina F. Gorodnitsky, and Marta Kutas. *Automatic removal of eye movement and blink artifacts from EEG data using blind component separation.* Psychophysiology, 41(2):313–325, 2004.

[106] Tzyy-ping Jung, Scott Makeig, Colin Humphries, Te-Won Lee, Martin J. McKeown, Vicente Iragui, and Terrence J. Sejnowski. *Removing electroencephalographic artifacts by blind source separation.* Psychophysiology, 37(2):S0048577200980259, 2000.

[107] Jukka Pekka Kauppi, Lauri Parkkonen, Riitta Hari, and Aapo Hyvärinen. *Decoding magnetoencephalographic rhythmic activity using spectrospatial information.* NeuroImage, 83:921–936, 2013.

[108] J.M. M Kilner, J. Mattout, R. Henson, and K.J. J Friston. *Hemodynamic correlates of EEG: a heuristic.* NeuroImage, 28(1):280–286, oct 2005.

[109] B. T. Klassen, J. G. Hentz, H. A. Shill, E. Driver-Dunckley, V. G H Evidente, M. N. Sabbagh, C. H. Adler, and J. N. Caviness. *Quantitative EEG as a predictive biomarker for Parkinson disease dementia.* Neurology, 77(2):118–124, 2011.

[110] W Klimesch. *EEG alpha and theta oscillations reflect cognitive and memory performance: a review and analysis.* Brain research reviews, 29(2-3):169–95, apr 1999.

[111] Wolfgang Klimesch, Paul Sauseng, and Simon Hanslmayr. *EEG alpha oscillations: the inhibition-timing hypothesis.* Brain research reviews, 53(1):63–88, jan 2007.

[112] B Knutson, A Westdorp, E Kaiser, and D Hommer. *FMRI visualization of brain activity during a monetary incentive delay task.* NeuroImage, 12(1):20–7, 2000.

[113] Gennady G. Knyazev. *EEG delta oscillations as a correlate of basic homeostatic and motivational processes.* Neuroscience and Biobehavioral Reviews, 36(1):677–695, 2012.

[114] Zbyněk Koldovský, Petr Tichavský, and Erkki Oja. *Efficient variant of algorithm FastICA for independent component analysis attaining the Cramér-Rao lower bound.* IEEE Transactions on Neural Networks, 17(5):1265–1277, 2006.

[115] J Kornelsen and P W Stroman. *fMRI of the lumbar spinal cord during a lower limb motor task.* Magn Reson Med, 52(2):411–414, 2004.

[116] Natasa Kovacevic and Anthony Randal McIntosh. *Groupwise independent component decomposition of EEG data and partial least square analysis.* NeuroImage, 35(3):1103–1112, 2007.

[117] K Krakow, F G Woermann, M R Symms, P J Allen, L Lemieux, G J Barker, J S Duncan, and D R Fish. *EEG-triggered functional MRI of interictal epileptiform activity in patients with partial seizures.* Brain, 122(9):1679–1688, 1999.

[118] René Labounek. *Analýza souvislostí mezi simultánně měřenými EEG a fMRI daty.* In Master Thesis, pages 1–62. Brno University of Technology, Supervised by Martin Lamoš, 2012.

[119] René Labounek, David A. Bridwell, Radek Mareček, Martin Lamoš, Michal Mikl, Milan Brázdil, Jiří Jan, and Petr Hluštík. *Stable EEG spatiospectral sources using relative power as group-ICA input.* In World Congress on Medical Physics & Biomedical engineering [Under Review], 2018.

[120] René Labounek, David A Bridwell, Radek Mareček, Martin Lamoš, Michal Mikl, Tomáš Slavíček, Petr Bednařík, Jaromír Baštinec, Petr Hluštík, Milan Brázdil, and Jiří Jan. *Stable scalp EEG spatiospectral patterns across paradigms estimated by group ICA.* Brain Topography, 31(1):76–89, 2018.

[121] René Labounek, David Janeček, Radek Mareček, Martin Lamoš, Tomáš Slavíček, Michal Mikl, Jaromír Baštinec, Petr Bednařík, David Bridwell, Milan Brázdil, and Jiří Jan. *Generalized EEG-fMRI spectral and spatiospectral heuristic models.* In 13th International Symposium on Biomedical Imaging: From Nano to Macro, pages 767–770, Prague, 2016. IEEE.

[122] René Labounek, David Janeček, Dominika Sanetrníková, Martin Lamoš, Radek Mareček, and Jiří Jan. *EEG Regressor Builder 2.0*, 2012. Brno. Available from: `http://www.ubmi.feec.vutbr.cz/sites/default/files/products/26150.zip`.

[123] René Labounek, Martin Lamoš, Radek Mareček, Milan Brázdil, and Jiří Jan. *Exploring task-related variability in fMRI data using fluctuations in power spectrum of simultaneously acquired EEG.* *Journal of Neuroscience Methods*, 245:125–136, 2015.

[124] René Labounek, Martin Lamoš, Radek Mareček, and Jiří Jan. *Analysis of connections between simultaneous EEG and fMRI data.* In *19th International Conference on Systems, Signals and Image Processing*, number April, pages 576–579, Vienna, Austria, 2012.

[125] Dave R M Langers. *Unbiased group-level statistical assessment of independent component maps by means of automated retrospective matching.* *Human Brain Mapping*, 31(5):727–742, 2010.

[126] H Laufs, John L Holt, Robert Elfont, Michael Krams, Joseph S Paul, K Krakow, and A Kleinschmidt. *Where the BOLD signal goes when alpha EEG leaves.* *NeuroImage*, 31(4):1408–18, jul 2006.

[127] H Laufs, A Kleinschmidt, A Beyerle, E Eger, A Salek-Haddadi, C Preibisch, and K Krakow. *EEG-correlated fMRI of human alpha activity.* *NeuroImage*, 19(4):1463–1476, aug 2003.

[128] H. Laufs, K. Krakow, P. Sterzer, E. Eger, A. Beyerle, A. Salek-Haddadi, and A. Kleinschmidt. *Electroencephalographic signatures of attentional and cognitive default modes in spontaneous brain activity fluctuations at rest.* *Proceedings of the National Academy of Sciences*, 100(19):11053–11058, 2003.

[129] P. C. Lauterbur. *Image Formation by Induced Local Interactions: Examples Employing Nuclear Magnetic Resonance.* *Nature*, 242:190–191, 1973.

[130] L Lemieux, A Salek-Haddadi, O Josephs, P Allen, N Toms, C Scott, K Krakow, R Turner, and D R Fish. *Event-related fMRI with simultaneous and continuous EEG: description of the method and initial case report.* *NeuroImage*, 14(3):780–7, sep 2001.

[131] Louis Lemieux, Helmut Laufs, David Carmichael, Joseph Suresh Paul, Matthew C. Walker, and John S. Duncan. *Noncanonical spike-related BOLD responses in focal epilepsy.* *Human Brain Mapping*, 29(3):329–345, 2008.

[132] Steven Lemm, Benjamin Blankertz, Gabriel Curio, and Klaus Robert Müller. *Spatio-spectral filters for improving the classification of single trial EEG.* *IEEE Transactions on Biomedical Engineering*, 52(9):1541–1548, 2005.

[133] K L Li, X P Zhu, J Waterton, and A Jackson. *Improved 3D quantitative mapping of blood volume and endothelial permeability in brain tumors.* *Journal of magnetic resonance imaging*, 12(2):347–357, 2000.

[134] Shijun Li, Yi Wang, Guangyu Bin, Xiaoshan Huang, Dan Zhang, Gang Liu, Yanwei Lv, Xiaorong Gao, and Shangkai Gao. *Space distribution of EEG responses to hanoi-moving visual and auditory stimulation with Fourier Independent Component Analysis.* *Frontiers in Human Neuroscience*, 9:1–13, 2015.

[135] Xi Lin Li and Tlay Adali. *Independent component analysis by entropy bound minimization.* *IEEE Transactions on Signal Processing*, 58(10):5151–5164, 2010.

[136] Yi-Ou Li, Tülay Adali, and Vince D Calhoun. *Estimating the number of independent components for functional magnetic resonance imaging data.* *Human brain mapping*, 28(11):1251–1266, 2007.

[137] Guillaume Lio and Philippe Boulinguez. *Greater robustness of second order statistics than higher order statistics algorithms to distortions of the mixing matrix in blind source separation of human EEG: Implications for single-subject and group analyses.* *NeuroImage*, 67:137–152, 2013.

[138] S Makeig, T P Jung, A J Bell, D Ghahremani, and T J Sejnowski. *Blind separation of auditory event-related brain responses into independent components.* *Proceedings of the National Academy of Sciences of the United States of America*, 94(20):10979–84, 1997.

[139] Dov Malonek and Amiram Grinvald. *Interactions between electrical activity and cortical microcirculation revealed by imaging spectroscopy: Implications for functional brain mapping.* *Science*, 272:551, 1996.

[140] D Mantini, L Marzetti, M Corbetta, G L Romani, and C Del Gratta. *Multimodal integration of fMRI and EEG data for high spatial and temporal resolution analysis of brain networks.* *Brain topography*, 23(2):150–8, 2010.

[141] D Mantini, M G Perrucci, C Del Gratta, G L Romani, and M Corbetta. *Electrophysiological signatures of resting state networks in the human brain.* *Proceedings of the National Academy of Sciences of the United States of America*, 104(32):13170–5, aug 2007.

[142] Dante Mantini, Maurizio Corbetta, Mauro Gianni Perrucci, Gian Luca Romani, and Cosimo Del Gratta. *Large-scale brain networks account*

for sustained and transient activity during target detection. NeuroImage, 44(1):265–274, jan 2009.

[143] Radek Mareček, Martin Lamoš, René Labounek, Marek Bartoň, Tomáš Slavíček, Michal Mikl, Ivan Rektor, and Milan Brázdil. *Multiway array decomposition of EEG spectrum: Implications of its stability for the exploration of large-scale brain networks.* Neural computation, 29(4), 2017.

[144] Radek Mareček, Martin Lamoš, Michal Mikl, Marek Bartoň, J Fajkus, Ivan Rektor, and Milan Brázdil. *What can be found in scalp EEG spectrum beyond common frequency bands. EEG–fMRI study.* Journal of Neural Engineering, 13(4):1–13, 2016.

[145] Eduardo Martínez-Montes, Pedro a Valdés-Sosa, Fumikazu Miwakeichi, Robin I Goldman, and Mark S Cohen. *Concurrent EEG/fMRI analysis by multiway Partial Least Squares.* NeuroImage, 22(3):1023–34, jul 2004.

[146] M J McKeown, S Makeig, G G Brown, T P Jung, S S Kindermann, a J Bell, and T J Sejnowski. *Analysis of fMRI data by blind separation into independent spatial components.* Human brain mapping, 6(3):160–188, 1998.

[147] Jianjun Meng, Gan Huang, Dingguo Zhang, and Xiangyang Zhu. *Optimizing spatial spectral patterns jointly with channel configuration for brain-computer interface.* Neurocomputing, 104(October 2016):115–126, 2013.

[148] Matthias C Meyer, Erik S B van Oort, and Markus Barth. *Electrophysiological correlation patterns of resting state networks in single subjects: a combined EEG-fMRI study.* Brain topography, 26(1):98–109, 2013.

[149] Kai J Miller. *Broadband spectral change: evidence for a macroscale correlate of population firing rate?* The Journal of Neuroscience, 30(19):6477–9, may 2010.

[150] Fumikazu Miwakeichi, Eduardo Martínez-Montes, Pedro A. Valdés-Sosa, Nobuaki Nishiyama, Hiroaki Mizuhara, and Yoko Yamaguchi. *Decomposing EEG data into space-time-frequency components using Parallel Factor Analysis.* NeuroImage, 22(3):1035–1045, 2004.

[151] T.K. Moon. *The expectation-maximization algorithm.* IEEE Signal Processing Magazine, 13(6):47–60, 1996.

[152] Matthias Moosmann, Tom Eichele, Helge Nordby, Kenneth Hugdahl, and Vince D Calhoun. *Joint independent component analysis for simultaneous EEG-fMRI: principle and simulation.* *International journal of psychophysiology : official journal of the International Organization of Psychophysiology*, 67(3):212–21, mar 2008.

[153] Matthias Moosmann, Petra Ritter, Ina Krastel, Andrea Brink, Sebastian Thees, Felix Blankenburg, Birol Taskin, Hellmuth Obrig, and Arno Villringer. *Correlates of alpha rhythm in functional magnetic resonance imaging and near infrared spectroscopy.* *NeuroImage*, 20(1):145–158, sep 2003.

[154] Susumu Mori. *Introduction to Diffusion Tensor Imaging.* Elsevier, Amsterdam, 2 edition, 2007.

[155] M E Moseley, Y Cohen, J Kucharczyk, J Mintorovitch, H S Asgari, M F Wendland, J Tsuruda, and D Norman. *Diffusion-weighted MR imaging of anisotropic water diffusion in cat central nervous system.* *Radiology*, 176(2):439–445, 1990.

[156] Christoph Mulert, Lorenz Jäger, Robert Schmitt, Patrick Bussfeld, Oliver Pogarell, Hans-Jürgen Möller, Georg Juckel, and Ulrich Hegerl. *Integration of fMRI and simultaneous EEG: towards a comprehensive understanding of localization and time-course of brain activity in target detection.* *NeuroImage*, 22(1):83–94, may 2004.

[157] Ernst Niedermeyer and FH Lopes da Silva. *Electroencephalography: basic principles, clinical applications, and related fields.* Lippincott Williams & Wilkins, 6th edition, 2011.

[158] Vadim V. Nikulin, Guido Nolte, and Gabriel Curio. *A novel method for reliable and fast extraction of neuronal EEG/MEG oscillations on the basis of spatio-spectral decomposition.* *NeuroImage*, 55(4):1528–1535, 2011.

[159] Michael Novey and Tülay Adali. *Complex ICA by negentropy maximization.* *IEEE Transactions on Neural Networks*, 19(4):596–609, 2008.

[160] Quadrianto Novi, Cuntai Guan, Tran Huy Dat, and Ping Xue. *Sub-band common spatial pattern (SBCSP) for brain-computer interface.* *Proceedings of the 3rd International IEEE EMBS Conference on Neural Engineering*, pages 204–207, 2007.

[161] S Ogawa, T M Lee, a R Kay, and D W Tank. *Brain magnetic resonance imaging with contrast dependent on blood oxygenation.* In *Proceedings of the*

National Academy of Sciences of the United States of America, volume 87, pages 9868–72, dec 1990.

[162] S Ogawa, R S Menon, D W Tank, S G Kim, H Merkle, J M Ellermann, and K Ugurbil. *Functional brain mapping by blood oxygenation level-dependent contrast magnetic resonance imaging. A comparison of signal characteristics with a biophysical model.* *Biophysical journal*, 64(3):803–12, mar 1993.

[163] S Ogawa, D W Tank, R Menon, J M Ellermann, S G Kim, H Merkle, and K Ugurbil. *Intrinsic signal changes accompanying sensory stimulation: functional brain mapping with magnetic resonance imaging.* In *Proceedings of the National Academy of Sciences of the United States of America*, volume 89, pages 5951–5955, 1992.

[164] Kei Omata, Takashi Hanakawa, Masako Morimoto, and Manabu Honda. *Spontaneous Slow Fluctuation of EEG Alpha Rhythm Reflects Activity in Deep-Brain Structures: A Simultaneous EEG-fMRI Study.* *PloS one*, 8(6):1–12, jan 2013.

[165] Julie Onton, Arnaud Delorme, and Scott Makeig. *Frontal midline EEG dynamics during working memory.* *NeuroImage*, 27(2):341–356, 2005.

[166] R.D. Pascual-Marqui, C.M. Michel, and D. Lehmann. *Low resolution electromagnetic tomography: a new method for localizing electrical activity in the brain.* *International Journal of Psychophysiology*, 18(1):49–65, 1994.

[167] B a Pearlmutter and L C Parra. *Maximum likelihood blind source separation: a context-sensitive generalization of ICA.* *Advances in Neural Information Processing Systems*, 9:613–619, 1997.

[168] Galina Portnova, Vladislav Balaev, Alina Tetereva, Mikhail Atanov, Alexey Ivanitsky, Ludmila Skiteva, Vladimir Ushakov, and Olga Martynova. *Correlation of BOLD Signal with Linear and Nonlinear Patterns of EEG in Resting State EEG-informed fMRI.* *Frontiers in Human Neuroscience*, 11(January):654, 2018.

[169] E M Purcell. *Spontaneous Emission Probabilities at Radio Frequencies.* In *Proceedings of the American Physical Society*, volume 69, page 681, 1946.

[170] I. I. Rabi. *Space Quantization in a Gyrating Magnetic Field.* *Physical Review*, 51(1):652–654, 1937.

[171] Pavan Ramkumar, Bruce C. Hansen, Sebastian Pannasch, and Lester C. Loschky. *Visual information representation and rapid-scene categorization are simultaneous across cortex: An MEG study.* NeuroImage, 134(March):295–304, 2016.

[172] Pavan Ramkumar, Lauri Parkkonen, Riitta Hari, and Aapo Hyvärinen. *Characterization of neuromagnetic brain rhythms over time scales of minutes using spatial independent component analysis.* Human Brain Mapping, 33(7):1648–1662, 2012.

[173] Pavan Ramkumar, Lauri Parkkonen, and Aapo Hyvärinen. *Group-level spatial independent component analysis of Fourier envelopes of resting-state MEG data.* NeuroImage, 86:480–491, 2014.

[174] Murray A. Reicher, Wolfgang Rauschning, Richard H. Gold, Lawrence W. Bassett, Robert B. Lufkin, and William Jr. Glen. *High-Resolution Magnetic Resonance Imaging of the Knee Joint: Normal Anatomy.* American journal of roentgenology, 145(5):895–902, 1985.

[175] J Rissanen. *Modelling by the shortest data description.* Automatica, 14:465–471, 1978.

[176] Guido Rodriguez, Francesco Copello, Paolo Vitali, Germana Perego, and Flavio Nobili. *EEG spectral profile to stage Alzheimer's disease.* Clinical Neurophysiology, 110:1831–1837, 1999.

[177] M J Rosa, J Kilner, F Blankenburg, O Josephs, and W Penny. *Estimating the transfer function from neuronal activity to BOLD using simultaneous EEG-fMRI.* NeuroImage, 49(2):1496–509, jan 2010.

[178] Afraim Salek-Haddadi, Beate Diehl, Khalid Hamandi, Martin Merschhemke, Adam Liston, Karl Friston, John S Duncan, David R Fish, and Louis Lemieux. *Hemodynamic correlates of epileptiform discharges: an EEG-fMRI study of 63 patients with focal epilepsy.* Brain research, 1088(1):148–166, 2006.

[179] V J Samar, K P Swartz, and M R Raghuveer. *Multiresolution analysis of event-related potentials by wavelet decomposition.* Brain and Cognition, 27(3):398–438, 1995.

[180] Vincent J Samar, Ajit Bopardikar, Raghuveer Rao, and Kenneth Swartz. *Wavelet Analysis of Neuroelectric Waveforms: A Conceptual Tutorial.* Brain and Language, 66(1):7–60, 1999.

[181] Gebhard Sammer, Carlo Blecker, Helge Gebhardt, Matthias Bischoff, Rudolf Stark, Katrin Morgen, and Dieter Vaitl. *Relationship between regional hemodynamic activity and simultaneously recorded EEG-theta associated with mental arithmetic-induced workload.* Human brain mapping, 28(8):793–803, aug 2007.

[182] Dominika Sanetrníková. *Převrácené hodnoty výkonu EEG signálu ve sdružené EEG-fMRI analýze.* In Bachelor Thesis, pages 1–54. Brno University of Technology, Supervised by René Labounek, 2014.

[183] René Scheeringa, M. C M Bastiaansen, Karl Magnus Petersson, Robert Oostenveld, David G. Norris, and Peter Hagoort. *Frontal theta EEG activity correlates negatively with the default mode network in resting state.* International Journal of Psychophysiology, 67(3):242–251, 2008.

[184] René Scheeringa, Karl Magnus Petersson, Andreas Kleinschmidt, Ole Jensen, and Marcel C M Bastiaansen. *EEG α power modulation of fMRI resting-state connectivity.* Brain connectivity, 2(5):254–64, jan 2012.

[185] Vincent J. Schmithorst and Scott K. Holland. *Comparison of Three Methods for Generating Group Statistical Inferences from Independent Component Analysis of Functional Magnetic Resonance Imaging Data.* Journal of Magnetic Resonance Imaging, 19(3):365–368, 2004.

[186] Gideon Schwarz. *Estimating the dimensions of the model.* Annals of Statistics, 6(2):461–464, 1978.

[187] Roberta Sclocco, Maria G Tana, Elisa Visani, Isabella Gilioli, Ferruccio Panzica, Silvana Franceschetti, Sergio Cerutti, and Anna M Bianchi. *EEG-informed fMRI analysis during a hand grip task: estimating the relationship between EEG rhythms and the BOLD signal.* Frontiers in Human Neuroscience, 8:186, 2014.

[188] Guofa Shou, Lei Ding, and Deepika Dasari. *Probing neural activations from continuous EEG in a real-world task: Time-frequency independent component analysis.* Journal of Neuroscience Methods, 209(1):22–34, 2012.

[189] N.D. Sidiropoulos, G.B. Giannakis, and R. Bro. *Blind PARAFAC receivers for DS-CDMA systems.* IEEE Transactions on Signal Processing, 48(3):810–823, 2000.

[190] A F M Smith and A E Gelfand. *Bayesian Statistics without Tears: A Sampling–Resampling Perspective.* The American Statistician, 46(2):84–88, 1992.

[191] R Soikkeli, J Partanen, H Soininen, A Pääkkönen, and P Riekkinen. *Slowing of EEG in Parkinson's disease.* Electroencephalography and clinical neurophysiology, 79(3):159–165, 1991.

[192] Sara Spadone, Stefania Della Penna, Carlo Sestieri, Viviana Betti, Annalisa Tosoni, Mauro Gianni Perrucci, Gian Luca Romani, and Maurizio Corbetta. *Dynamic reorganization of human resting-state networks during visuospatial attention.* Proceedings of the National Academy of Sciences of the United States of America, 112(26):8112–7, 2015.

[193] G. Srivastava, S. Crottaz-Herbette, K. M. Lau, G. H. Glover, and V. Menon. *ICA-based procedures for removing ballistocardiogram artifacts from EEG data acquired in the MRI scanner.* NeuroImage, 24(1):50–60, 2005.

[194] James V. Stone. *Independent component analysis: A Tutorial Introduction.* MIT press, Cambridge, MA, 2004.

[195] P Stroman. *Mapping of Neuronal Function in the Healthy and Injured Human Spinal Cord with Spinal fMRI.* NeuroImage, 17(4):1854–1860, 2002.

[196] P. W. Stroman, C. Wheeler-Kingshott, M. Bacon, J. M. Schwab, R. Bosma, J. Brooks, D. Cadotte, T. Carlstedt, O. Ciccarelli, J. Cohen-Adad, A. Curt, N. Evangelou, M. G. Fehlings, M. Filippi, B. J. Kelley, S. Kollias, A. Mackay, C. A. Porro, S. Smith, S. M. Strittmatter, P. Summers, and I. Tracey. *The current state-of-the-art of spinal cord imaging: Methods.* NeuroImage, 84:1070–1081, jan 2014.

[197] Patrick W. Stroman. *Magnetic Resonance Imaging of Neuronal Function in the Spinal Cord: Spinal fMRI.* Clinical Medicine and Research, 3(3):146–156, 2005.

[198] Markus Svensén, Frithjof Kruggel, and Habib Benali. *ICA of fMRI Group Study Data.* NeuroImage, 16(3):551–563, 2002.

[199] Yusuke Takeda, Nobuo Hiroe, Okito Yamashita, and Masa aki Sato. *Estimating repetitive spatiotemporal patterns from resting-state brain activity data.* NeuroImage, 133:251–265, 2016.

[200] Akaysha C. Tang, Matthew T. Sutherland, and Christopher J. McKinney. *Validation of SOBI components from high-density EEG.* NeuroImage, 25(2):539–553, 2005.

[201] Lixia Tian, Yazhuo Kong, Juejing Ren, Gaël Varoquaux, Yufeng Zang, and Stephen M. Smith. *Spatial vs. Temporal Features in ICA of Resting-State fMRI - A Quantitative and Qualitative Investigation in the Context of Response Inhibition.* *PLoS ONE*, 8(6), 2013.

[202] Ryota Tomioka, Guido Dornhege, Guido Nolte, Benjamin Blankertz, Kazuyuki Aihara, and Klaus-Robert Muller. *Spectrally weighted Common Spatial Pattern algorithm for single trial EEG classification.* *Dept Math Eng Univ Tokyo Tokyo Japan Tech Rep*, 40:1–23, 2006.

[203] Ivan Toni, Michael Krams, Robert Turner, and Richard E. Passingham. *The Time Course of Changes during Motor Sequence Learning: A Whole-Brain fMRI Study.* *NeuroImage*, 8(1):50–61, 1998.

[204] Martijn P. Van Den Heuvel, Ren?? C W Mandl, Ren?? S. Kahn, and Hilleke E. Hulshoff Pol. *Functionally linked resting-state networks reflect the underlying structural connectivity architecture of the human brain.* *Human Brain Mapping*, 30(10):3127–3141, 2009.

[205] M a van der Jagt, W M Brink, M J Versluis, S C a Steens, J J Briaire, a G Webb, J H M Frijns, and B M Verbist. *Visualization of Human Inner Ear Anatomy with High-Resolution MR Imaging at 7T: Initial Clinical Assessment.* *American journal of neuroradiology*, 36(2):378–383, 2015.

[206] Roemer van der Meij, Joshua Jacobs, and Eric Maris. *Uncovering phase-coupled oscillatory networks in electrophysiological data.* *Human Brain Mapping*, 36(7):2655–2680, 2015.

[207] Roemer Van Der Meij, Freek Van Ede, and Eric Maris. *Rhythmic components in extracranial brain signals reveal multifaceted task modulation of overlapping neuronal activity.* *PLoS ONE*, 11(6):1–28, 2016.

[208] R Vigário, J Särelä, V Jousmäki, M Hämäläinen, and E Oja. *Independent component approach to the analysis of EEG and MEG recordings.* *IEEE transactions on bio-medical engineering*, 47(5):589–593, 2000.

[209] S Vulliemoz, R Rodionov, D W Carmichael, R Thornton, M Guye, S D Lhatoo, C M Michel, J S Duncan, and L Lemieux. *Continuous EEG source imaging enhances analysis of EEG-fMRI in focal epilepsy.* *NeuroImage*, 49(4):3219–29, feb 2010.

[210] Yao Wang, Estate M Sokhadze, Ayman S El-Baz, Xiaoli Li, Lonnie Sears, Manuel F Casanova, and Allan Tasman. *Relative Power of Specific*

EEG Bands and Their Ratios during Neurofeedback Training in Children with Autism Spectrum Disorder. Frontiers in human neuroscience, 9(January):723, 2015.

[211] S Warach, J R Ives, G Schlaug, M R Patel, D G Darby, V Thangaraj, C M Michel, J S Duncan, and D L Schomer. *EEG-triggered echo-planar functional MRI in epilepsy.* Neurology, 47(1):89–93, 1996.

[212] Jonathan R. Wolpaw, Niels Birbaumer, William J. Heetderks, Dennis J. McFarland, P. Hunter Peckham, Gerwin Schalk, Emanuel Donchin, Louis A. Quatrano, Charles J. Robinson, and Theresa M. Vaughan. *Brain-computer interface technology: A review of the first international meeting.* IEEE Transactions on Rehabilitation Engineering, 8(2):164–173, 2000.

[213] K. J. Worsley and K.J. Friston. *Analysis of fMRI Time-Series Revisited—Again.* NeuroImage, 2(3):173–181, 1995.

[214] K. J. Worsley, K.J. J. Friston, A. P. Holmes, J-B. Poline, P. J. Grasby, S. C. R. Williams, R. S. J. Frackowiak, and R. Turner. *Analysis of fMRI Time-Series Revisited.* NeuroImage, 2(1):45–43, 1995.

[215] Lei Wu, Tom Eichele, and Vince D. Calhoun. *Reactivity of hemodynamic responses and functional connectivity to different states of alpha synchrony: A concurrent EEG-fMRI study.* NeuroImage, 52(4):1252–1260, 2010.

[216] Wei Wu, Xiaorong Gao, Bo Hong, and Shangkai Gao. *Classifying single-trial EEG during motor imagery by iterative spatio-spectral patterns learning (ISSPL).* IEEE Transactions on Biomedical Engineering, 55(6):1733–1743, 2008.

[217] Sakae Yamamoto and Shigeaki Matsuoka. *Topographic EEG Study of Visual Display Terminal (VDT) Performance with Special Reference to Frontal Midline Theta Waves.* Brain topography, 2(4):257–267, 1990.

[218] Arie Yeredor. *Blind separation of Gaussian sources via second-order statistics with asymptotically optimal weighting.* IEEE Signal Processing Letters, 7(7):197–200, 2000.

[219] Arie Yeredor. *Blind source separation via the second characteristic function.* Signal Processing, 80(5):897–902, 2000.

[220] Arie Yeredor. *Blind separation of Gaussian sources with general covariance structures: Bounds and optimal estimation.* IEEE Transactions on Signal Processing, 58(10):5057–5068, 2010.

[221] Q. Yu, L. Wu, David A. Bridwell, E. B. Erhardt, Y. Du, H. He, and Vince D. Calhoun. *Building an EEG-fMRI multi-modal brain graph: a concurrent EEG-fMRI study.* Frontiers in Human Neuroscience, 2016.

[222] Han Yuan, Tao Liu, Rebecca Szarkowski, Cristina Rios, James Ashe, and Bin He. *Negative covariation between task-related responses in alpha/beta-band activity and BOLD in human sensorimotor cortex: an EEG and fMRI study of motor imagery and movements.* NeuroImage, 49(3):2596–606, feb 2010.

LIST OF SYMBOLS, PHYSICAL CONSTANTS AND ABBREVIATIONS

Symbols

a, A	scalar value a, respectively A
$\boldsymbol{a}, \boldsymbol{A}$	matrix or vector $\boldsymbol{a}$, respectively $\boldsymbol{A}$
$\boldsymbol{A}^-$	$\boldsymbol{A}^- = \boldsymbol{A}^{-1}$; short prescription for $\boldsymbol{A}^{-1}$ of matrix $\boldsymbol{A}$
$\boldsymbol{A}^*$	prescription for matrix $\boldsymbol{A}$ with reduced dimensionality (e.g. with PCA)
$\breve{\boldsymbol{A}}$	best linear predictor of matrix $\boldsymbol{A}$
$\hat{\boldsymbol{A}}$	generative latent variable of matrix $\boldsymbol{A}$

Physical constants

c	channel of the EEG leads
t, T	time
α	8-12Hz frequency band of the EEG Signal
β	12-20Hz frequency band of the EEG Signal
γ	over 20Hz or 20-40Hz (in the current thesis) frequency band of the EEG Signal
δ	0-4Hz frequency band of the EEG Signal
θ	4-8Hz frequency band of the EEG Signal
ω	frequency

Abbreviations

AIC	Akaike's information criterion
AJDC	approximate joint diagonalization of Fourier cospectral matrices
ARF	α response function

BIC	Bayesian information criterion
BLP	best linear predictor
BOLD	blood oxygen level dependence
BSS	blind source separation
dHb	deoxy-hemoglobin
dMRI	diffusion weighted magnetic resonance imaging
EEG	electroencephalography
EM	expectation maximization
EP	evoked potential
ERP	event-related potential
fMRI	functional magnetic resonance imaging
FWE	family wise error
gICA	group Independent Component Analysis
GLM	general linear model
HOS	higher order statistics
HRF	hemodynamic response function
IC	indepdendent component
ICA	independent component analysis
INFOMAX	information maximization approach
IRF	impulse response function
ITC	information theoretic criteria
JADE	joint approximation diagonalization of eigenmatrices
KIC	Kullback-Leibler information criterion
LDA	linear discriminant analysis
LMS	least mean square

LORETA	low resolution brain electromagnetic tomography
LSBN	large scale brain network
MDL	maximum description length
MEG	magnetoencephalography
MIC	mutual information coefficient
ML	maximum likelihood
MR	magnetic resonance
MRI	magnetic resonance imaging
MSE	mean squared error
OLS	ordinary least square
PARAFAC	parallel factor analysis
PCA	principal component analysis
PLS	penalized least square
PPO	perpendicular projection operator
RSN	resting state network
SM	source matrix
SOBI	second order blind identification
SPM	statistical parametric map OR Statistical Parametric Mapping (software's name)
STP	spatio-temporal regression
SVD	singular value decomposition
TC	time course
WASOBI	weights-adjusted second order blind identification
WLS	weighted least square
WPLS	weighted penalized least square

LIST OF APPENDICES

A EEG-FMRI RESULTS FOR ABSOLUTE POWER SPATIOSPECTRAL PATTERNS

The legend for figures: In the plot below each fMRI map, the black dashed-dotted line represents the canonical HRF, and the purple line represents our median-derived IRF from the white boxplots, where blue oblongs are quartiles and red dots are outliers. The spatiospectral patterns are indicated on the column on the left, and F-statistic results are overlayed on the fMRI maps if there are 100 contiguous voxels with $p < 0.001$. The colorbar indicates the F values in the corresponding map. The values in the table under each pattern are group-averaged t-values of the statistical significance between the spatiospectral pattern dynamics and the stimulus vectors (S – sentence block in SDT, F – frequent, T – target, D – distractor in VOT).

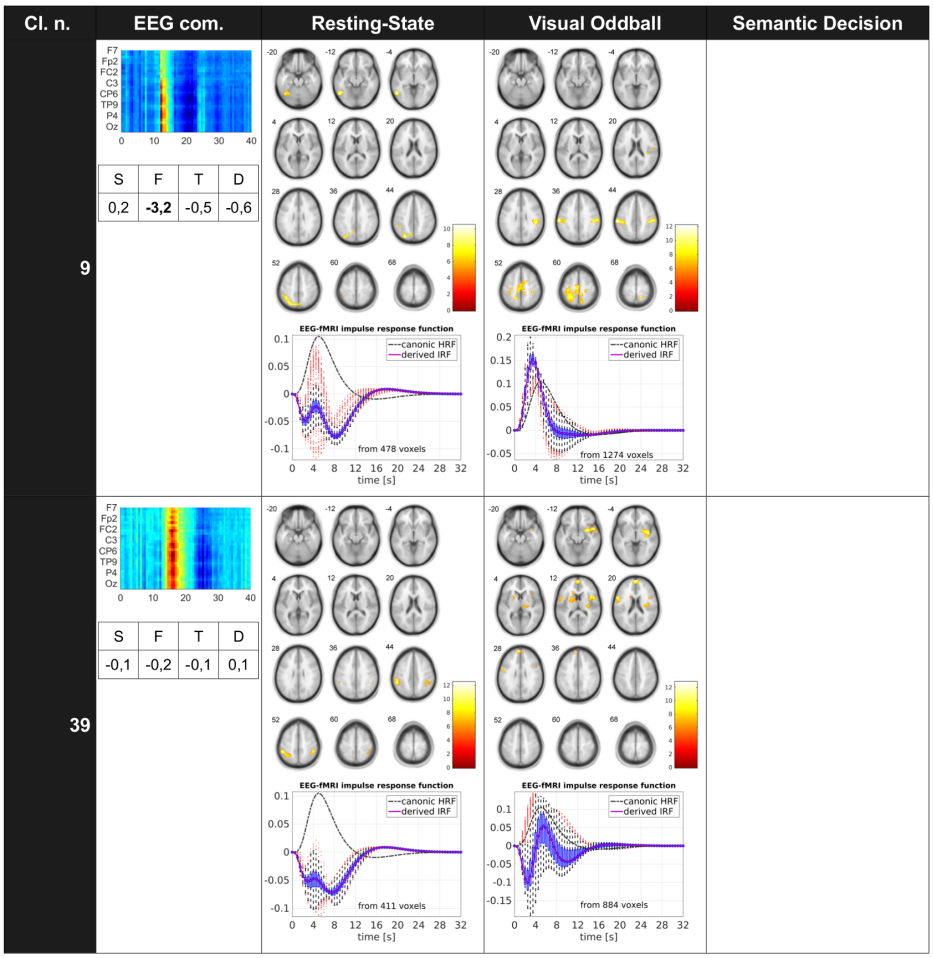

Fig. A.1: EEG-fMRI results for absolute β-band spatiospectral patterns: EEG-fMRI F-map threshold at $p < 0.001$ uncorrected for multiple comparison errors.

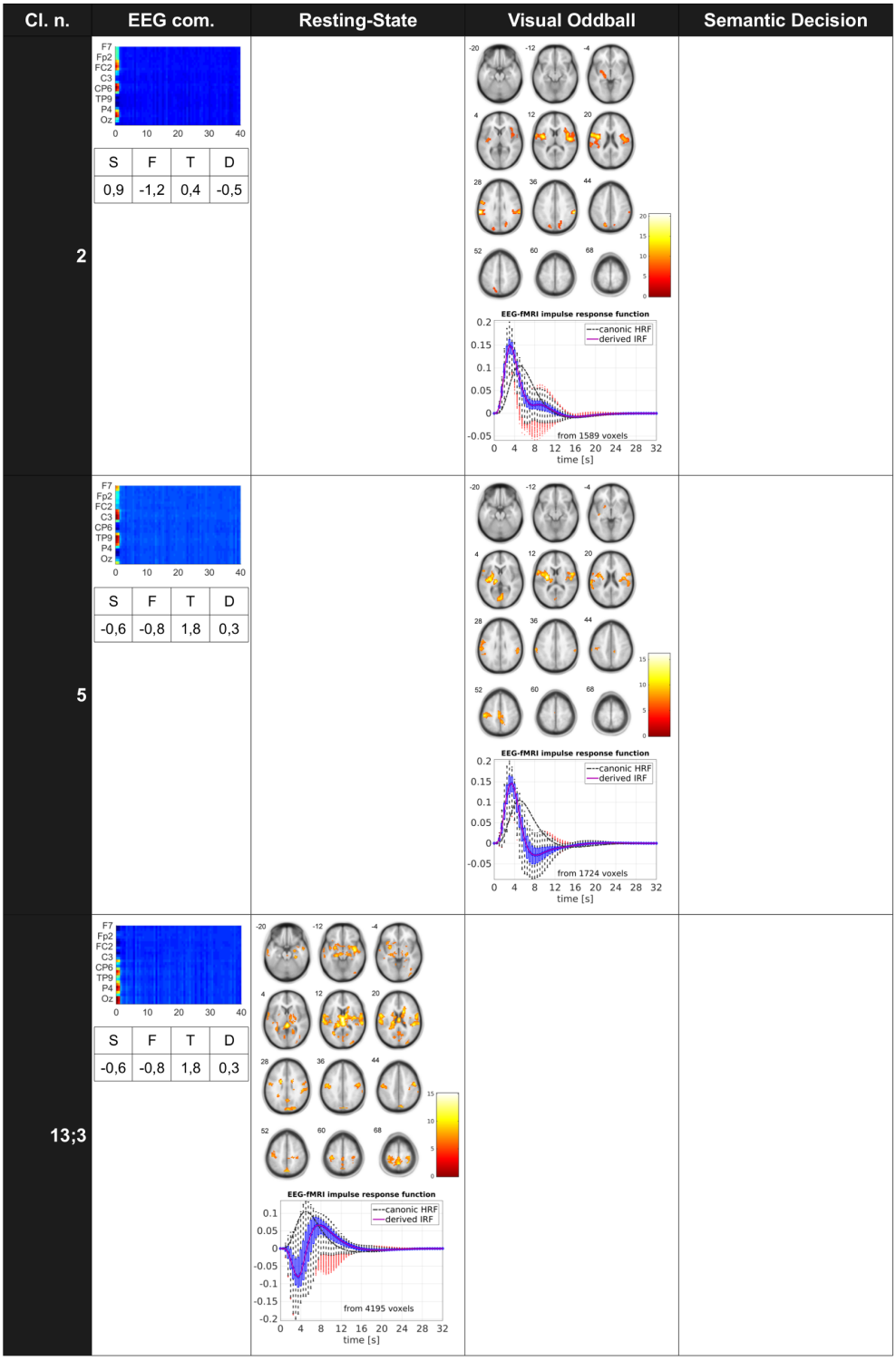

Fig. A.2: EEG-fMRI results for absolute δ-band spatiospectral patterns: EEG-fMRI F-map threshold at $p < 0.001$ uncorrected for multiple comparison errors.

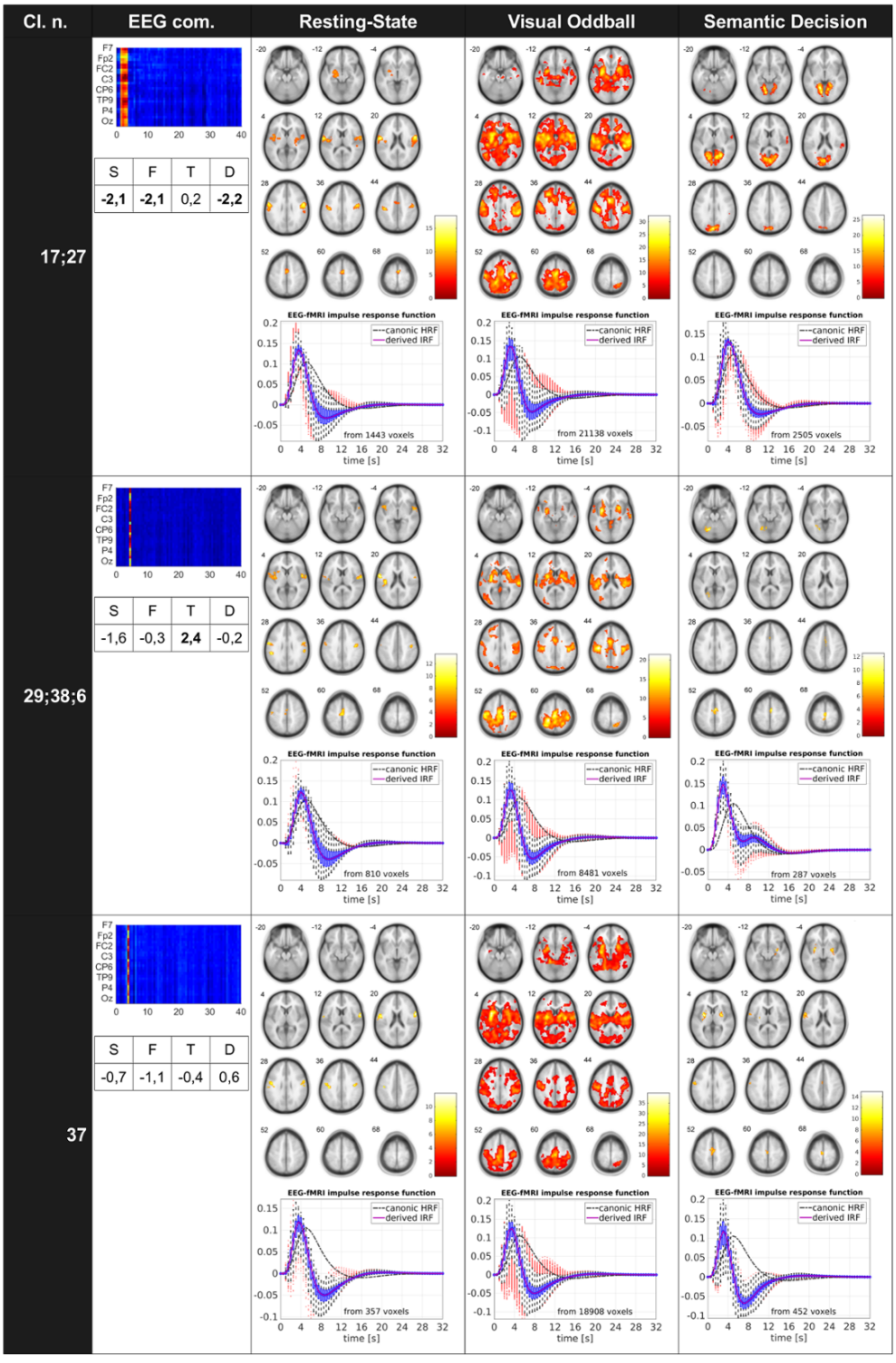

Fig. A.3: EEG-fMRI results for absolute θ-band spatiospectral patterns: EEG-fMRI F-map threshold at $p < 0.001$ uncorrected for multiple comparison errors.

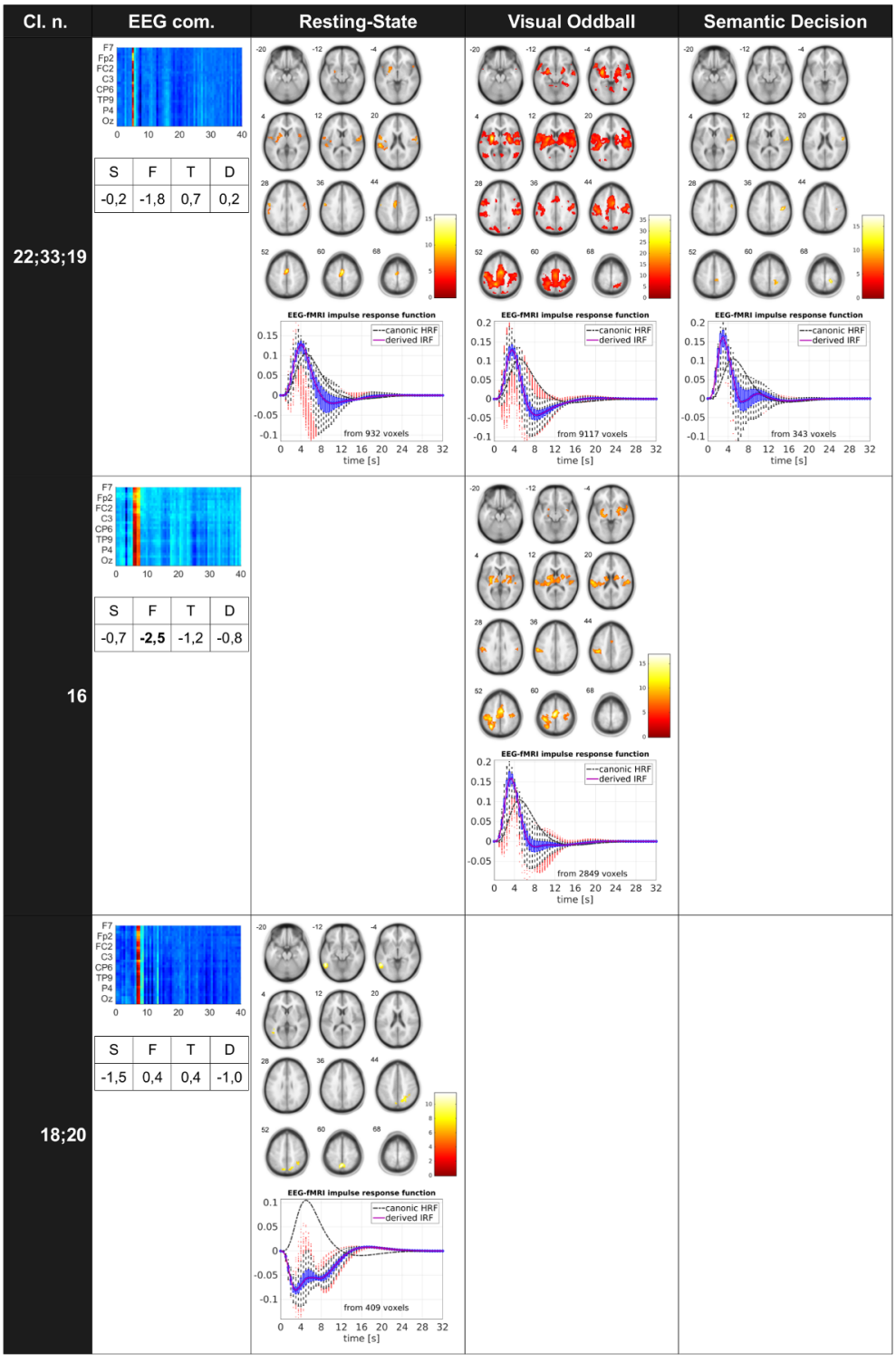

Fig. A.4: EEG-fMRI results for absolute high θ-band spatiospectral patterns: EEG-fMRI F-map threshold at $p < 0.001$ uncorrected for multiple comparison errors.

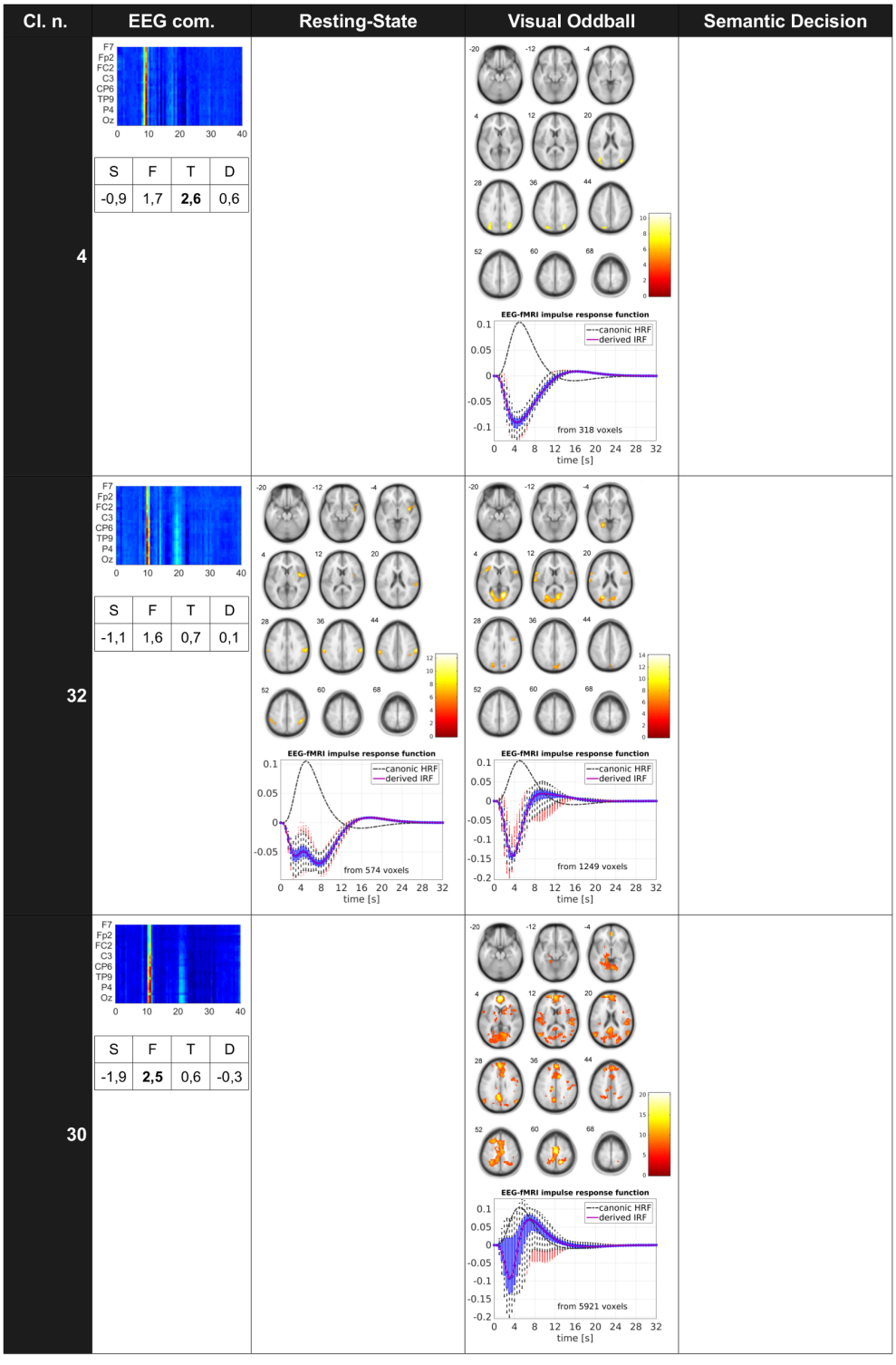

Fig. A.5: EEG-fMRI results for absolute α-band spatiospectral patterns: EEG-fMRI F-map threshold at $p < 0.001$ uncorrected for multiple comparison errors.

B ATTACHED IMPLEMENTED MATLAB FUNCTIONS

B.1 Batch scripts

B.1.1 batch_matrix_E.m

The batch script is calculating matrix $\boldsymbol{E}(n_T, n_c \cdot n_\omega)$ from preprocessed EEG data for all subjects.

B.1.2 batch_spatiospectral_gICA.m

The batch script is estimating the spatiospectral group-ICA with GIFT software libraries.

B.1.3 batch_glm_eeg_fmri_hrf_derivates.m

The batch script is estimating general linear model between time-courses of EEG spatiospectral patterns and fMRI-BOLD signals with variable hemodynamic response functions. The SPM12 libraries are necessary and used for estimations.

B.1.4 batch_anova_eeg_fmri.m

The batch script is preforming the group one-way ANOVA test with multiple measurements on single subjects EEG-fMRI results previously estimated with batch_glm_eeg_fmri_hrf_derivates.m script.

B.1.5 batch_k-means_clustering.m

The batch script is preforming k-means clustering over different numbers of set output clusters and evaluate the clusters' stability.

B.2 Scripts and functions

B.2.1 spectral_ICA_process.m and norm_power.m

The functions which are calculating and forming matrices $\boldsymbol{E}(n_T, n_c \cdot n_\omega)$. They are called in batch_matrix_E.m script.

B.2.2 ICA_EEG_for_clustering.m

The script which transforms the GIFT result outputs $\boldsymbol{S}$ (sources) into the input form for the k-means clustering. The following k-means clustering is run with batch_k-means_clustering.m script.

B.2.3 matrix2nifti.m

The function is transforming 3D matrix $\boldsymbol{E}(n_T, n_c \cdot n_\omega)$ into 3D NIFTI files, which are importable by GIFT software library.

B.2.4 create_mask.m

The script which is creating mask of the same dimensions as 3D matrices created within matrix2nifti.m function.

B.2.5 getClusters.m

The function is performing the k-means clustering with Pascual-Marqui et al. (1995) algorithm [166]. The function was implemented by my colleague Radek Mareček from Central European Institute of Technology, Brno, Czech Republic.

B.2.6 k-means_classification.m

The script which is classifying the output k-means clusters and quantifying basic statistical clusters' parameters.

B.2.7 ICA_component_processing.m

The script which transforms the GIFT result outputs $\boldsymbol{A}$ (time-courses) into the input form for general linear model with stimulus vectors.

B.2.8 glm_eeg_regresrors.m

The script is estimating general linear model between time-sources of EEG spatiospectral patterns (data $\boldsymbol{Y}$) and stimulus vectors (in model matrix $\boldsymbol{X}$).

B.3 Scripts for result visualizations

B.3.1 topology_visualize.m

The script is visualizing the topologies of EEG spatiospectral patterns.

B.3.2 frequency_visualize.m

The script is visualizing the spectral densities of EEG spatiospectral patterns with their confidence intervals.

B.3.3 dendrogram_visualization.m

The script is visualizing the dendrogram of estimated clusters.

B.3.4 cluster_cross_correlation.m

The script is visualizing intra- and inter-cluster correlations for one cluster of interest.

B.3.5 cluster_mean_cross_correlation.m

The script is visualizing mean intra- and inter-cluster correlations over all estimated stable EEG spatiospectral patterns.

B.3.6 hrf_var.m

The script is visualizing the estimated hemodynamic response functions from supra-threshold voxels of group-averaged EEG-fMRI F-maps ($p<0.001$ uncorrected for multiple testing errors).

B.4 EEG Regressor Builder ver. 2.0

All EEG-fMRI results for generalized spectral heuristic model were estimated with our proposed software EEG Regressor Builder ver. 2.0 [122], which I and my students have changed and improved [100, 101, 182] during my Ph.D. studies, since its initial version proposed originally as my Master Thesis [118].